SPECTRAL AND STATISTICAL ANALYSES OF EXPERIMENTAL RADAR CLUTTER DATA

A THESIS SUBMITTED TO
THE GRADUATE SCHOOL OF NATURAL AND APPLIED SCIENCES
OF
MIDDLE EAST TECHNICAL UNIVERSITY

BY

NAZLI DENİZ KAHYAOĞLU

IN PARTIAL FULFILLMENT OF THE REQUIREMENTS
FOR
THE DEGREE OF MASTER OF SCIENCE
IN
ELECTRICAL AND ELECTRONICS ENGINEERING

DECEMBER 2010

Approval of the thesis:

SPECTRAL AND STATISTICAL ANALYSES OF EXPERIMENTAL RADAR CLUTTER DATA

submitted by **NAZLI DENİZ KAHYAOĞLU** in partial fulfillment of the requirements for the degree of **Master of Science in Electrical and Electronics Engineering Department, Middle East Technical University** by,

Prof. Dr. Canan ÖZGEN
Dean, Graduate School of **Natural and Applied Sciences**

Prof. Dr. İsmet ERKMEN
Head of Department, **Electrical and Electronics Engineering**

Assoc. Prof. Dr. Ali Özgür YILMAZ
Supervisor, **Electrical and Electronics Engineering Dept., METU**

Examining Committee Members:

Prof. Dr. Yalçın TANIK
Electrical and Electronics Engineering Dept., METU

Assoc. Prof. Dr. Ali Özgür YILMAZ
Electrical and Electronics Engineering Dept., METU

Prof. Dr. Sencer KOÇ
Electrical and Electronics Engineering Dept., METU

Assoc. Prof. Dr. Çağatay CANDAN
Electrical and Electronics Engineering Dept., METU

Dr. Ülkü ÇİLEK DOYURAN
Design Leader, ASELSAN

Date:

I hereby declare that all information in this document has been obtained and presented in accordance with academic rules and ethical conduct. I also declare that, as required by these rules and conduct, I have fully cited and referenced all material and results that are not original to this work.

Name, Last Name: NAZLI DENİZ KAHYAOĞLU

Signature :

ABSTRACT

SPECTRAL AND STATISTICAL ANALYSES OF EXPERIMENTAL RADAR CLUTTER DATA

KAHYAOĞLU, Nazlı Deniz
M.Sc., Department of Electrical and Electronics Engineering
Supervisor : Assoc. Prof. Dr. Ali Özgür YILMAZ

December 2010, 139 pages

The performance of radar detection and imaging systems strongly depends on the characteristics of radar clutter. In order to improve the radar signal processing algorithms, successful analysis and modeling of radar clutter are required. For a successful model of radar clutter, both the spectral and statistical characteristics of the clutter should be revealed. Within the scope of this study, an experimental radar data acquisition system is established to analyze radar clutter. The hardware and the data processing system are first verified using generic signals and then a set of measurements is taken in the open terrain. In this thesis, the limitations and problems encountered during the establishment of the system are explained in detail. The spectral and statistical analyses performed on the recorded data are examined. The temporal and spatial behavior of the measured clutter data are explored. The hypothetical models proposed so far in the literature are tested on the experimental data and the fitting of models to the experimental data is confirmed using various goodness-of-fit tests. Finally, the results of the analyses are interpreted in the light of the radar system parameters and the characteristics of the illuminated terrain.

Keywords: Radar clutter, range-Doppler processing, statistical analysis, spectral estimation, experimental data

ÖZ

DENEYSEL RADAR KARGAŞA VERİSİNİN İSTATİKSEL VE SPEKTRAL ANALİZİ

KAHYAOĞLU, Nazlı Deniz
Yüksek Lisans, Elektrik ve Elektronik Mühendisliği Bölümü
Tez Yöneticisi : Doç. Dr. Ali Özgür YILMAZ

Aralık 2010, 139 sayfa

Radar tespit ve görüntüleme sistemlerinin başarımı radar kargaşasının karakteristiğine bağlıdır. Radar sinyal işleme algoritmalarını geliştirmek için, radar kargaşasının analiz edilmesi ve modellenmesi gerekmektedir. Başarılı bir radar kargaşa modeli için, kargaşanın hem spektral hem de istatiksel karakteristiği ortaya çıkarılmalıdır. Bu çalışma kapsamında, radar kargaşasını analiz etmek için, deneysel radar verisi toplama sistemi kurulmuştur. Donanım ve veri işleme sistemi önce jenerik sinyaller kullanılarak doğrulanmış ve ardından açık alanda ölçümler alınmıştır. Bu tezde, sistemin kurulumu sırasında karşılaşılan sınırlamalar ve problemler detaylı bir şekilde anlatılmıştır. Kaydedilmiş veri üzerinde spektral ve istatiksel analizler gerçekleştirilmiştir. Ölçülen kargaşa verisinin zamansal ve uzaysal davranışı araştırılmıştır. Literatürde şimdiye kadar önerilen kuramsal modeller deneysel veri üzerinde test edilmiş ve modellerin deneysel veriye uyumu çeşitli uyum-iyiliği testleri kullanılarak doğrulanmıştır. Son olarak, analiz sonuçları radar sistem parametreleri ve incelenen alanın karakteristiği ışığında yorumlanmıştır.

Anahtar Kelimeler: Radar kargaşası, menzil-Doppler işleme, istatiksel analiz, spektral kestirim, deneysel veri

To my family

and

To Engin

ACKNOWLEDGMENTS

I would like to express my deepest gratitude to my supervisor Assoc. Prof. Dr. Ali Özgür YILMAZ for his precious guidance, advice, criticism, encouragement and insight throughout the development of this work. I would also like to thank Prof. Dr. Sencer KOÇ for his valuable suggestions, comments and support. The technical discussions with them are gratefully appreciated.

I owe my most sincere gratitude to my friend Nezaket KILIÇOĞLU, with whom I spent the last two years with all the hard times and nice memories. The sincere friendship we started to share is maybe the best part of this work.

I also wish to thank TÜBİTAK-UZAY for the environment provided to me throughout the research. All my colleagues and friends at TÜBİTAK-UZAY are appreciated for their support and encouragement. I would like to express my special thanks to Hacer SUNAY and Celal DUDAK since this work would hardly be possible without their great patience and understanding.

Special appreciation and gratitude are also to my family for their endless love, constant support, great patience and extensive encouragement throughout my whole life.

Finally, the words are not enough to express my appreciation to my dearest, Engin, who always makes me count myself lucky that he is in my life.

TABLE OF CONTENTS

CHAPTERS

LIST OF TABLES

TABLES

LIST OF FIGURES

FIGURES

LIST OF ABBREVIATIONS

ACF	Autocorrelation Function
AD	Anderson-Darling
ADC	Analog-to-Digital Converter
ALC	Automatic Level Control
BW	Bandwidth
CDF	Cumulative Distribution Function
CFAR	Constant False Alarm Rate
CG	Compound Gaussian
CLT	Central Limit Theorem
CNR	Clutter-to-Noise Ratio
COTS	Commercial Off-The-Shelf
CS	Chi-Square
CUT	Cell Under Test
CW	Continuous Wave
EXA	X-Series Signal Analyzer
F	Noise Factor
FFT	Fast Fourier Transform
GC	Generalized Compound
GK	Generalized K
GO-CFAR	Greatest of CFAR
GoF	Goodness-of-Fit
GUI	Graphical User Interface
I	In-phase Component
IF	Intermediate Frequency
KS	Kolmogorov-Smirnov
LAN	Local Area Network
LFM	Linear Frequency Modulation
LNA	Low Noise Amplifier
METU	Middle East Technical University
MIT-LL	Massachusetts Institute of Technology - Lincoln Laboratory
MKS	Modified Kolmogorov-Smirnov
MLE	Maximum Likelihood Estimation
MoM	Method of Moments
MTI	Moving Target Indicator
NF	Noise Figure
NRCS	Normalized Radar Cross Section
PCR	Pulse Compression Ratio
pdf	Probability Density Function
PRI	Pulse Repetition Interval
PSA	Performance Spectrum Analysis
PSD	Power Spectral Density
PW	Pulse Width
Q	Quadrature Component
RBW	Resolution Bandwidth
RCS	Radar Cross Section
RF	Radio Frequency
RH-CFAR	Range Heterogeneous CFAR
SAR	Synthetic Aperture Radar
SCPI	Standard Commands for Programmable Instruments
SNR	Signal-to-Noise Ratio
VSA	Vector Signal Analyzer
VSG	Vector Signal Generator

CHAPTER 1

INTRODUCTION

RADAR (RAdio Detection And Ranging) is an electromagnetic remote sensing instrument, used for detecting, ranging and tracking targets. Basically, an electromagnetic wave is transmitted and the echo reflected by the target is used to determine its direction, distance or speed. The return signal is composed of the direct path return from the target, multipath returns, echoes from other objects, thermal noise, and jammer if present. Anything except the target, jammer and noise can be considered as clutter.

First, the clutter differs from noise in two ways: 1) They have different correlation properties. The clutter is a correlated interference, i.e., it has a non-white power spectrum. 2) Unlike noise, clutter is a type of echo, hence its power is affected by the radar parameters [25].

On the other hand, the difference between clutter and jammer is that the clutter is a passive interference, where the jammer is an active one.

Lastly, the definition of target differs according to the function of the radar. For instance, the clouds can be considered as clutter for air traffic radars, while as target for weather radars. Similarly, the surface of earth is the target for synthetic aperture radars, and the clutter for surveillance radars.

The radar clutter may be homogeneous or not. The homogeneity of clutter depends on the cell-to-cell amplitude variations. On the other hand, the clutter can be classified as fluctuating or non-fluctuating according to the temporal behavior. The behavior of clutter in both space and time is of great importance to radar detection mechanisms and imaging technologies. Besides, for a successful characterization of clutter, the spectral and statistical properties of clutter should be considered.

In order to find an appropriate model, the radar clutter, especially the ground and sea clutter, has been widely studied in the literature and various spectral and statistical models have been proposed [15], [16], [22], [24], [27], [28]. Once appropriate clutter models are obtained, they are utilized to develop various detection algorithms and to evaluate their performance as in [3], [6], [23], [29], [34], [36].

The basic motivating factor behind this work is to examine spatial and temporal spectral and statistical characteristics of experimental radar clutter. In order to perform analyses on the experimental radar clutter data, an experimental data acquisition and data processing system is established within the scope of this study.

In the chapters that follow, analysis of radar clutter is presented as follows:

In Chapter 2, various methods of radar clutter analysis are examined. First, the concept of data storage structure is discussed. Then, the spatial and temporal correlation and the Doppler-spreading effect of clutter are studied. Chapter 2 also covers the spatial and temporal statistical analyses of clutter, which complement the spectral analysis and yield a complete understanding of clutter. This chapter ends with explanation of the concept of clutter reflectivity.

In Chapter 3, the experimental data acquisition set-up used in this study is described. First, the general block diagram of the system is given. After the transmitter and the receiver blocks are presented in detail, the signal processing of the received signal is explained. Finally, the whole system is verified using generic signals.

Chapter 4 covers the analyses of the experimental data. The results of the statistical and spectral analyses performed on the received signal, and the calculation of the clutter reflectivity are given for each measurement together with the characteristics of the studied terrain.

Finally, in Chapter 5, the results are concluded and the possible future works are stated.

CHAPTER 2

RADAR CLUTTER ANALYSIS

2.1 Data Matrix Construction

In radar signal processing, there is a well-accepted approach of using a data storage structure in order to illustrate various digital processing concepts. The data structure is constructed in such a way that spectral and statistical processing operations can be performed on its dimensions. Hence, in order to construct such a structure, first the dimensions should be determined. Each of pulse number, delay of the radar echo, receiver channel number, azimuth and elevation angles of the antenna can be considered as a potential dimension of the data storage structure [25, chap 3.1]. Among them, the ones which are of interest are determined according to the data acquisition scenario. For instance, for a phased-array antenna system, in which a group of antennas is used, one dimension can be assigned to the receiver channel number. On the other hand, if the angular position of the antenna does not change in the data acquisition system, there is no need to define any dimension representing the azimuth or elevation angle. Once the dimensions are determined, the complex baseband samples of the received radar signal are aligned according to them. The samples are in $I + jQ$ form, where I and Q represent the voltage of in-phase and quadrature components of the received signal, respectively.

In this study, only two dimensions of the return signal, which represent the pulse number and the delay, are of interest. Hence, throughout this thesis, the data storage structure will be mentioned as the *data matrix*. In order to illustrate how the data matrix is constructed, consider the transmitted train of M pulses given in Figure 2.1. The antenna beam is fixed, so the same region is illuminated in each pulse repetition interval (PRI). For the return signal, each

PRI is divided into N successive *range cells* (*range bins* or *delay bins*), each corresponding to a fixed delay. The return signal is then sampled and stored in an MxN matrix (Figure 2.2), so that each row represents the samples of a fixed PRI and each column is composed of the samples taken from successive pulses after a fixed delay. Successive columns of a given row is referred to as the *fast time* domain, while the opposite is called the *slow time* domain.

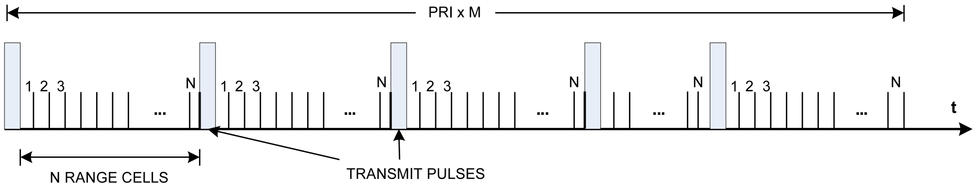

Figure 2.1: Pulse train as the transmitting signal

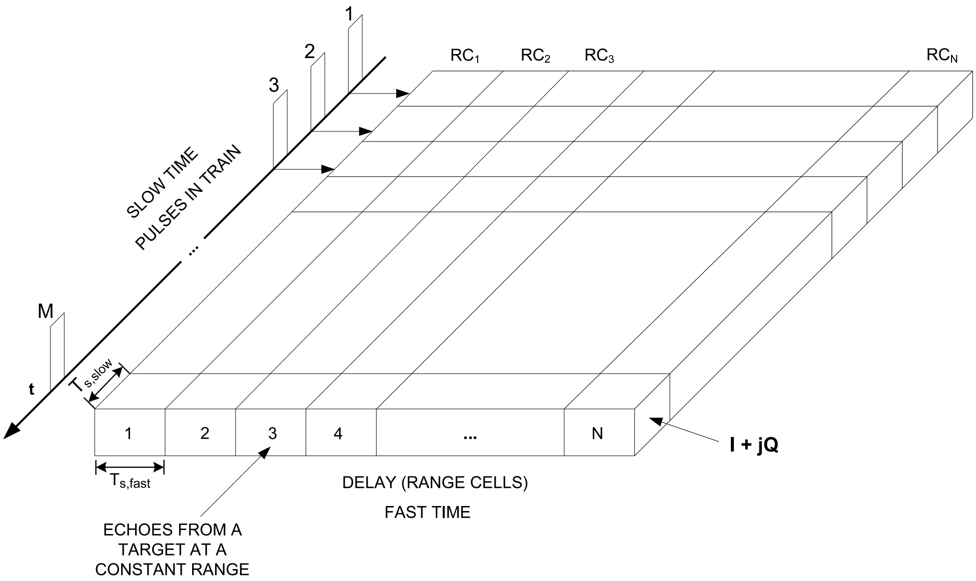

Figure 2.2: Data matrix

In order to place the samples in the data matrix, the knowledge of sampling rates in both dimensions is required. To begin with the fast time, let $T_{s,\,fast}$ denote the time interval between two successive range samples from a single received pulse. According to the Nyquist criterion, the minimum sampling rate required for unique recovery of the received signal is twice its bandwidth. In a radar system, the received signal gives information about the reflection of the transmitted signal from different range cells. Hence, it will be appropriate to model the radar return signal $r(t)$ as the convolution of the transmitting signal $x(t)$ and the range reflectivity function of the illuminated area $p(t)$ [25, chap 3.1]. Then, the spectrum of the return signal is the product of the spectra of $x(t)$ and $p(t)$. That is,

$$r(t) = x(t) * p(t) \tag{2.1a}$$

$$R(f) = X(f) \cdot P(f). \tag{2.1b}$$

Since the spectrum of $p(t)$ is assumed to occupy a larger bandwidth than that of $x(t)$ [25, chap 2.8], the spectrum of the return signal is determined by the latter. Hence, only the bandwidth of the transmitting signal can be taken into account in determining the Nyquist sampling rate. Thus, the minimum frequency of sampling in range, $F_{s,\,fast}$, can be chosen as twice the bandwidth of the transmitting signal, B_{TX}, i.e.,

$$F_{s,\,fast} \geq 2 \cdot B_{TX} \tag{2.2}$$

according to the Nyquist sampling theorem. In order to find the unknown B_{TX} in the above relation, consider a rectangular pulse of duration PW as the transmitting signal. Although it is not bandlimited, its bandwidth can be approximated by the Rayleigh bandwidth as

$$B_{TX} \cong \frac{1}{PW}. \tag{2.3}$$

The pulse width PW of the transmitting signal in relation (2.3) also determines the range resolution of the system as follows

$$R_{res} = \frac{c \cdot PW}{2}. \tag{2.4}$$

Combining the relations in (2.2), (2.3), and (2.4),

$$F_{s,\,fast} \geq \frac{c}{R_{res}} \tag{2.5a}$$

$$T_{s,\,fast} \leq \frac{R_{res}}{c} \tag{2.5b}$$

Then, the fast time sampling interval, or equivalently the range cell spacing, should be chosen considering the range resolution. It is important to state here the importance of range cell spacing for discrete time target detection mechanism. A target peak in a resolution cell may be missed if an appropriate sampling is not provided in the range and there is no sample *near* the target. Hence, the range cell spacing should be fine enough to catch as much details as possible from the terrain. As a result, the Nyquist sampling rate in fast time domain, i.e., $F_{s,\,fast}$, is determined according to the transmitting signal, which is constructed in such a way that it satisfies the range resolution requirement of the system.

Having found the fast time sampling criterion, the next step is to determine the slow time sampling interval related to the data matrix, i.e., sampling along one column. The slow time data represent the samples taken from the same range cell in each pulse. For a given range cell, both the intrinsic motion of the illuminated area and the radar platform may yield pulse-to-pulse phase variation, which corresponds to a Doppler shift. This results in a spread in the spectrum of the slow time signal, hence a nonzero Doppler bandwidth [25, chap 2.8]. According to the Nyquist sampling theorem, the frequency of sampling in slow time, $F_{s,\,slow}$, can be expressed as

$$F_{s,\,slow} \geq 2 \cdot B_D \tag{2.6}$$

where B_D represents the bandwidth of the slow time signal.

On the other hand, it is obvious that the slow time sampling interval, $T_{s,\,slow}$ is equal to the PRI of the pulse train. Then, the frequency of sampling in slow time, $F_{s,\,slow}$ is

$$F_{s,\,slow} = \frac{1}{T_{s,\,slow}} = \frac{1}{PRI} \tag{2.7}$$

From (2.6) and (2.7),

$$F_{s,\,slow} = \frac{1}{PRI} \geq 2 \cdot B_D \tag{2.8}$$

The selection of $F_{s,\,slow}$ or PRI is important from two points of view:

1. The unambiguous Doppler spectrum width is given by

$$\beta_D = \frac{1}{PRI}. \tag{2.9}$$

An unambiguous Doppler spectrum width β_D, which is small with respect to clutter and target Doppler frequencies yields Doppler ambiguities. In order to eliminate Doppler ambiguities, β_D should be sufficiently high, which requires PRI to be decreased.

2. The unambiguous range can be evaluated as

$$R_{ua} = \frac{c \cdot (PRI - PW)}{2}. \tag{2.10}$$

   That is, for a better R_{ua}, PRI should be increased.

It is important to note that there is a trade-off between β_D and R_{ua}. For a better β_D, PRI should be decreased causing R_{ua} to decrease.

Apart from the range and Doppler ambiguities, the Doppler resolution D_{res}, which is important for target detection, is also of concern. If the number of pulses is denoted by M, the increased PRI improves the Doppler resolution:

$$D_{res} = \frac{1}{total\ length} = \frac{1}{M \cdot PRI}. \tag{2.11}$$

Consequently, the slow time Nyquist sampling rate $F_{s,\,slow}$ can be determined considering the unambiguous Doppler spectrum width and unambiguous range requirements of the system together with the target detection concerns.

To sum up, the sampling rates in fast time and slow time of the data matrix can be mainly determined according to the Nyquist sampling theorem. However, some other criteria regarding the performance of the system, such as detection and imaging resolution and ambiguities, are also taken into account.

2.2 Spectral Analysis of Clutter

The spectral analysis of clutter is of great importance to successful design of radar processor. In order to better understand its importance, the principle period of a generic Doppler spectrum shown in Figure 2.3 should be examined [25]. In the figure, the spectral contents of targets, noise and clutter can be seen. In this spectrum, the zero-Doppler bin corresponds to the DC return, i.e., the returns from stationary targets. Moving targets appear in the spectrum according to their relative radial velocity with respect to the radar. The receiver noise is spread uniformly over the whole spectrum. Finally, the clutter occupies a region around the zero-Doppler bin due to the intrinsic motion of clutter sources.

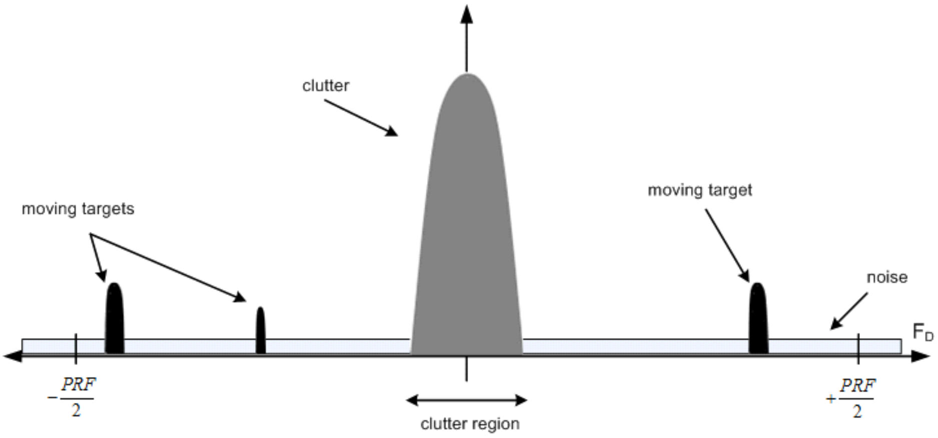

Figure 2.3: Generic Doppler spectrum

According to this spectrum, for a target which is outside the clutter region, the only interference is the thermal noise. However, the spectral contents at or near zero-Doppler frequency are dominated by the clutter. Hence, a target in this region should overcome this clutter besides noise in order to be detected. However, poor knowledge of the spectral characteristics of clutter may yield some degradation in the performance of moving target indication (MTI) radars.

Consider the data matrix which is constructed in Section 2.1. The Doppler spectrum for each range bin can be obtained by computing the discrete Fourier transform (DFT) over the slow-time samples. Then, the slow-time dimension of the data matrix is converted into the Doppler frequency.

Based on the Doppler spectrum obtained for a given range bin, the power spectral density (PSD) of the slow time samples $y(t)_{t=1}^{M}$ can also be estimated. In this nonparametric method, the PSD estimator, which is given in

$$\hat{\phi}_P(\omega) = \frac{1}{M}\left|\sum_{t=1}^{M} y(t)\, e^{-i\omega t}\right|^2, \tag{2.12}$$

is called the *periodogram*.

On the other hand, the concept of correlation time introduces another approach to the spectral information. In order to understand the behavior of clutter in time, it is also important to answer the following question: "How long does it take for the clutter component to change significantly?" As stated in [12], the temporal information contained in the correlation time is equivalent to the spectral information in the random process in time, based on the fact that the DFT of the autocorrelation function gives the power spectral density (Wiener-Khintchine Theorem). Then, assuming the stationarity of the slow time samples, the correlogram, which is also a nonparametric method, gives the PSD estimate according to

$$\hat{\phi}_C(\omega) = \sum_{k=-(N-1)}^{N-1} \hat{r}(k)\, e^{-i\omega k}, \tag{2.13}$$

where $\hat{r}(k)$ can be unbiased or biased autocovariance of the slow-time data sequence:

$$\hat{r}_{unbiased}(k) = \frac{1}{N-k}\sum_{t=k+1}^{N} y(t)\, y^*(t-k),\ 0 \leq k \leq N-1 \tag{2.14a}$$

$$\hat{r}_{biased}(k) = \frac{1}{N}\sum_{t=k+1}^{N} y(t)\, y^*(t-k),\ 0 \leq k \leq N-1 \tag{2.14b}$$

Note that, if the biased autocovariance is used, the correlogram estimate becomes equal to the periodogram [26].

Although both methods provide good resolution for sufficiently large data sequences, the variance of the estimates is high [26]. In these methods, when a data sample is added to the sequence, this new sample is used to make estimation at a new additional frequency instead of improving the estimate on hand. Hence, the variance of the estimate cannot be decreased by increasing the data length.

In order to improve the PSD estimate, various methods are proposed. For instance, as in the *modified periodogram method*, non-rectangular windows may be used to make the edges of the signal smoother, thereby reducing the spectral leakage.

Another method is the *Welch method*, in which the data sequence is divided into segments (the segments may overlap) and the modified periodogram is computed for each segment. Then, the average of the estimates from each segment gives the new PSD estimate.

In these methods, the variance of the PSD estimate is decreased relative to the periodogram. However, the following two points should be noted: 1) The average power of the windowed signal changes due the samples attenuated by the non-rectangular windows. Hence, a normalization should be taken into account. 2) There is a trade-off between the resolution and the variance of the estimate. Methods used to decrease the variance of the estimate degrades the spectral resolution.

The PSD estimate of the slow time samples gives an idea about the spectral characteristics of the clutter component in that range bin. In the literature, there are many studies on the spectral characterization of clutter. For instance, in [14], the spectral content of windblown trees is examined on the recorded radar clutter data and also a comprehensive comparison with the previous studies is provided. According to this study, the measured Doppler spread of windblown foliage is found to be about 1 m/sec under light wind conditions at levels of 60-80 dB below the zero-Doppler peak. Also, it is reported that the spread due to clutter is found to increase with the force of the wind. For windy conditions, the spread is reported as 3 m/sec. However, as opposed to many previous studies, the spread is expected not to exceed 4 m/sec even for gale force winds. The inconsistencies with the previous studies are mostly attributed to the problems of the measurement systems.

2.3 Statistical Analysis of Clutter

In a radar system, the interference and target echoes are represented by statistical models, hence radar detection can be considered as a statistical decision problem [25, chap 6]. For a given range cell, target detection can be modeled as a binary hypothesis testing where

$$H_0 \sim \text{Target is } \textit{absent}$$
$$H_1 \sim \text{Target is } \textit{present}$$

and the decision may result in one of the four possible cases given in Table 2.1.

Table 2.1: Target detection decision table

	Decide H_0	**Decide H_1**
Target absent	Correct rejection	False alarm
Target present	Miss	Detection

The decision of *absence* or *presence* of a target can be made according to a test statistic which is computed for the current scenario and compared to a threshold value. For example, the test statistic can be derived based on the Neyman-Pearson criterion, so that the probability of detection is maximized for a given probability of false alarm. Such detectors are referred to as *constant false alarm rate (CFAR) detectors*.

The probability of detection and the probability of false alarm can be expressed as

$$P_D = \int_{\mathfrak{R}_1} p_{\mathbf{y}}(\mathbf{y} \mid H_1)\, \mathbf{dy} \tag{2.15a}$$
$$P_{FA} = \int_{\mathfrak{R}_1} p_{\mathbf{y}}(\mathbf{y} \mid H_0)\, \mathbf{dy} \tag{2.15b}$$

respectively, where **y** represents the observation from the cell under test (CUT). The observation composing of N samples can be considered as a vector in an N-dimensional space:

$$\mathbf{y} = [y_1 \cdots y_N]. \tag{2.16}$$

Each vector in that space corresponds to one of the decisions H_0 or H_1. The region $\mathfrak{R}_1$ denotes the set of all observations for which H_1 is chosen. The conditional probability density functions (pdfs), $p_{\mathbf{y}}(\mathbf{y} \mid H_0)$ and $p_{\mathbf{y}}(\mathbf{y} \mid H_1)$, represent the relative likelihoods of observation $\mathbf{y}$ under each of the two hypotheses, i.e., H_0 and H_1, respectively. When the decision rule is derived based on the Neyman-Pearson criterion as in Appendix A, the test statistic in (2.17), which is also called the *likelihood ratio*, is found to be a function of these two conditional pdfs.

$$\frac{p_{\mathbf{y}}(\mathbf{y} \mid H_1)}{p_{\mathbf{y}}(\mathbf{y} \mid H_0)} \gtrless_{H_0}^{H_1} \gamma \tag{2.17}$$

In order to model these two conditional pdfs, the distribution of any interference that is present in the CUT should be given. Even all the parameters should be known as well as the distribution itself. Hence, in the presence of clutter besides noise, perfect knowledge of its distribution becomes important in determining the test statistic used in target detection.

Besides, the statistics of clutter is of great importance to the assignment of threshold value for the decision rule. The threshold level for the CUT is selected according to the level of interference, i.e., noise, jammer and clutter if present, in that CUT. The interference level is directly related to the parameters of the clutter distribution and it may vary in space and time.

Radar clutter statistics can be analyzed in two main frameworks: 1) spatial variation and 2) temporal behavior of the clutter [9], [12], [25, chap 2.3]. The former characterizes the cell-to-cell variation of clutter, whereas the latter is based on observation of a specific range cell over time. Generally, the spatial and temporal distributions are found to be different. Both spatial and temporal analyses are carried out on the clutter amplitude, in-phase (I) component, and quadrature (Q) component. The aim of these analyses is to assess the underlying distribution of the experimental radar clutter data.

In the first subsection, spatial analysis of clutter statistics is discussed. The significant role of spatial variation of clutter in radar detection and imaging mechanisms is stated. Theoretical distributions proposed in the literature up to now for clutter amplitude and I and Q components are presented.

The second subsection covers the examination of clutter statistics in terms of temporal variation. Distributions suggested to model the temporal characteristics of clutter in a specific range cell are also given.

In the third subsection, the concept of space-time compound model is explained and various compound distributions for the clutter amplitude statistics are presented in detail.

This section ends with the complementary methods used to check the fit of experimental data to the proposed hypothetical models. The main advantages and drawbacks of these empirical fitting methods are briefly explained.

2.3.1 Spatial Statistics of Clutter

At a given time, the clutter varies from one region to another. The variation of clutter in space is described by its spatial distribution. The distribution of clutter in space is crucial in terms of the performance of radar detection mechanisms. Moreover, in order to interpret high resolution SAR images for terrain classification and target recognition, it is required to extract the detailed spatial texture of clutter in the illuminated region [28]. As the range resolution increases, it becomes possible to resolve discrete structures in the region and the range heterogeneity of the clutter prevails. Hence, the spatial variance of clutter may increase. That is, the probability of clutter amplitude taking values away from the mean increases. Hence, an increase in the variance causes the tails of the clutter pdf to rise up.

The effect of the clutter tail on the radar detection performance can be explained as follows: Due to the long tail of the highly-varying clutter amplitude, the return signal may take larger values in some range cells. For the fixed threshold detectors, this may result in a misleading peak crossing the detection threshold level, hence the P_{FA} increases. As opposed to fixed threshold detectors, CFAR detectors provide adaptive threshold levels for different interference levels in different range cells in order to satisfy the required detection performance. However, if clutter is the dominant interference, rather than thermal noise, conventional CFAR detectors may suffer from high spatial variation of clutter [25, chap 7.4]. When the clutter is highly heterogeneous over the range cells, the parameters of clutter distribution, which are directly related to the clutter level, differ significantly from cell to cell. Hence, conventional CFAR detectors have difficulty in setting the correct threshold level near the clutter edges, which may result in either a false alarm or miss of a target in undesired proportions. Knowledge of the spatial variation of clutter helps to interpret these possible wrong decisions. Also, to overcome the problems in the clutter edges, understanding the spatial clutter statistics forms a base to develop alternative detection mechanisms, such as Greatest of CFAR (GO-CFAR) and Range Heterogeneous CFAR (RH-CFAR) [29].

Having explained the significance of spatial distribution of clutter in terms of detection and imaging performance, some hypothetical spatial models proposed in the literature can now be examined. However, before presenting the models, spatial calibration should be applied to the return signal. In the next section, these calibration operations are explained.

2.3.1.1 Calibration for Spatial Analysis

In order to make the spatial analysis of clutter data independent of distance and cell area of the illuminated region, two calibration operations should be applied to the received signal. For these calibrations, consider the fast time dimension of the data matrix explained in Section 2.1. The fast time complex samples represent the signal return from successive range cells in terms of voltage.

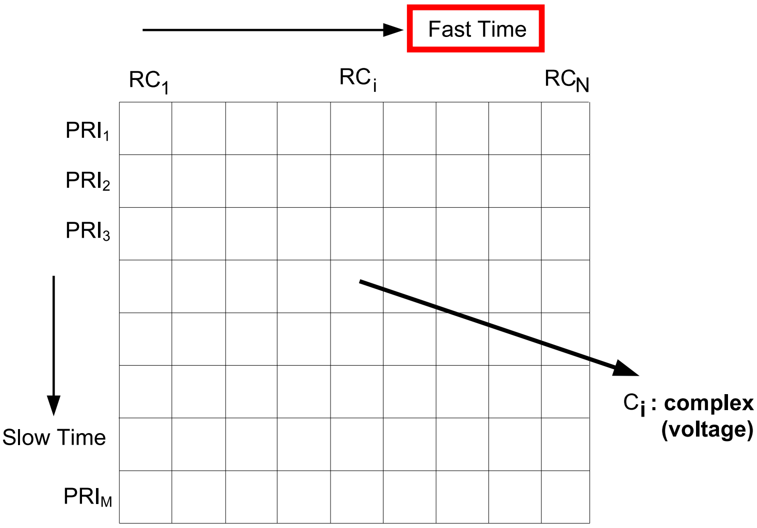

Figure 2.4: Data matrix and spatial calibration

For the first calibration, consider the radar power equation. According to the radar power equation, the power of the return signal decreases with the fourth power of the distance, D. That is,

$$P_{received} \propto \frac{1}{D^4} \tag{2.18}$$

Then, the received voltage decreases with D^2:

$$V_{received} \propto \frac{1}{D^2} \tag{2.19}$$

Hence, the decrease in the voltage of the fast time samples due to distance should be compensated by multiplying the samples with R_i^2, where R_i represents the distance of the i^{th} range cell to the antenna. In (2.20), R is the range cell spacing and i is the range cell index, i.e., $i = 1, 2, ..., N$.

$$R_i = i \cdot R \tag{2.20}$$

The second calibration required for the spatial statistical analysis is the calibration with respect to the illuminated cell area. Although the illuminated range cells are equally spaced, they are not of equal size due to the azimuthal beam of the antenna, θ. The effect of antenna beam on the cell area is illustrated in Figure 2.5.

According to the radar power equation, the power return is directly proportional to the cell area. Then, the relative return from the close-by cells will be smaller than the cells that are far from the antenna, since the cell area decreases as approached to the antenna. In order to eliminate the effect of unequal power return due to unequal cell areas, normalization is required. The power return of each range cell should be divided by the cell area A_i, where i represents the range cell index, i.e., $i = 1, 2, ..., N$. Equivalently, the complex baseband samples should be divided by the square root of A_i.

To sum up the calibration operations in the fast time, let C_i denote the complex baseband sample from the i^{th} range cell (Figure 2.4). Then, the calibrated sample

$$C_i \cdot \frac{R_i^2}{\sqrt{A_i}} \tag{2.21}$$

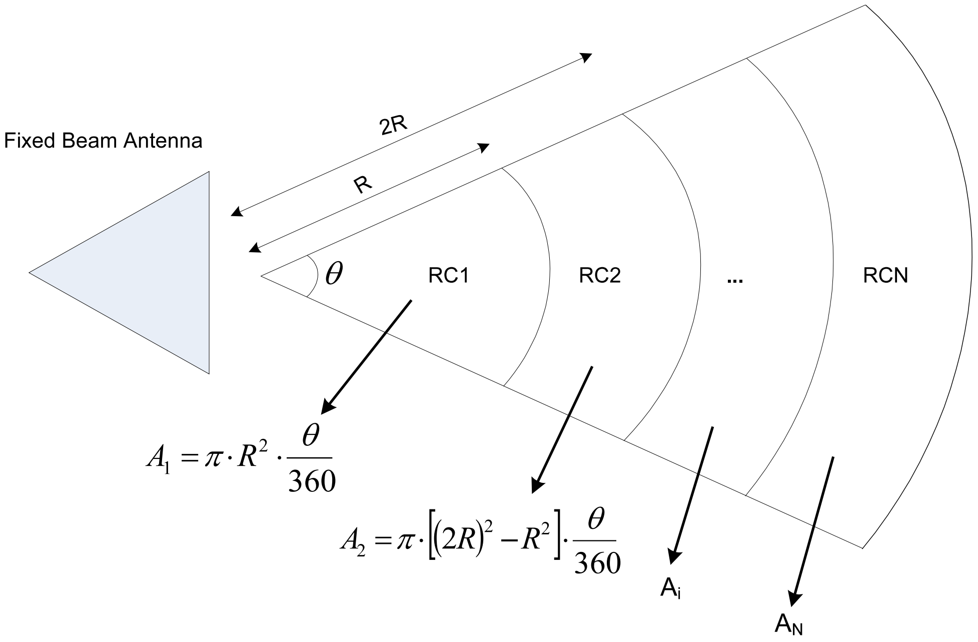

Figure 2.5: Azimuthal antenna beam and the area of the illuminated range cells

should be used in the spatial statistical analysis. In the end, the overall calibration factor is in the order of R_i.

Finally, it is important to note that these corrections are applied after the data are received, i.e., at the stage of data processing. However, there is also a mechanism not studied here called *sensitivity time control (STC)*, which provides a range-dependent gain during data acquisition [12], [17], [25], [33].

2.3.1.2 Spatial Clutter Models

There are various statistical models suggested for the spatial behavior of I and Q components and amplitude of the radar clutter. In this chapter, the proposed pdfs and their parameters are examined in detail. The properties of the distributions which will be required for the empirical fitting tests, such as cumulative distribution functions (CDFs) and raw moments are also presented in this section.

In radar systems with low range resolution, the spatial behavior of I and Q components of clutter can be modeled with Gaussian distribution [30]. Since the resolution is low, a range cell can be assumed to consist of a sufficiently large number of independent scatterers. Then, the resulting distribution can be approximated by Gaussian pdf based on the central limit theorem (CLT). Let the random variable S_{IQ} denote the voltage of I or Q component of the clutter in a range cell (‘S’ stands for spatial). Then, the proposed Gaussian pdf and CDF are given as follows

$$p_{Gaussian}(s_{IQ}) = \frac{1}{\sqrt{2\pi\sigma^2}} \exp\left[-\frac{(s_{IQ}-\mu)^2}{2\sigma^2}\right] \tag{2.22a}$$

$$F_{Gaussian}(s_{IQ}) = \frac{1}{2}\left[1 + \operatorname{erf}\left(\frac{s_{IQ}-\mu}{\sqrt{2\sigma^2}}\right)\right] \tag{2.22b}$$

where the parameters μ and σ represent the mean and the standard deviation and *erf(.)* is the error function. The effect of changing these two parameters on the distribution is depicted in Figure 2.6. The parameter μ changes the location of the pdf, where σ is related to the scale of the pdf.

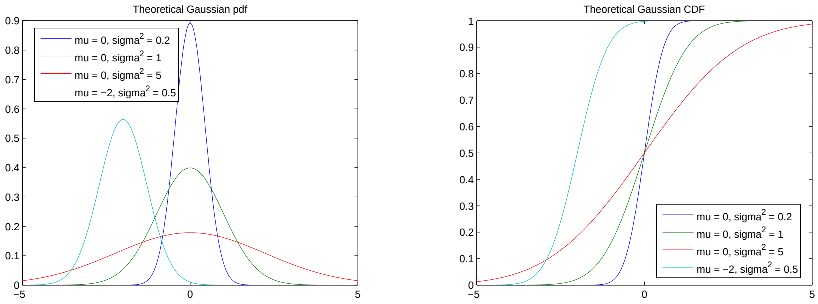

(a)

(b)

Figure 2.6: (a) Theoretical Gaussian pdf, (b) Theoretical Gaussian CDF

However, CLT fails as the range resolution is improved, since the number of scatterers in a resolution cell becomes finite or one of the scatterers dominates [29]. Hence, the assumption of Gaussian pdf for the distributions of I and Q components of the clutter is no more valid. It has been stated that the I and Q components of high resolution clutter are spikier than Gaussian distributed I and Q [17]. If the range resolution is sufficiently high, the radar system will be able to resolve the heterogeneity of the region. That is, radar becomes more sensitive to spatial variations of clutter from range cell to range cell, which results in a spiky characteristic.

For a complex random variable, whose real and imaginary parts are independent and Gaussian distributed, the amplitude is then Ricean or Rayleigh distributed. Thus, the amplitude of clutter in low resolution radar systems can be either Ricean or Rayleigh modeled. If the clutter amplitude in one range cell is denoted by the random variable, S_Z ,

$$S_Z = \sqrt{{S_I}^2 + {S_Q}^2} \tag{2.23}$$

where the I and Q components are Gaussian with non-zero mean

$$S_I \sim \mathcal{N}(\nu \cos\theta, c^2)$$
$$S_Q \sim \mathcal{N}(\nu \sin\theta, c^2)$$

then S_Z is Ricean distributed as in (2.24). ($I_0(.)$ is the modified Bessel function of the first kind with order zero.)

$$p_{Ricean}(s_Z;\, c, \nu) = \frac{s_Z}{c^2} \exp\left[-\frac{\left({s_Z}^2 + \nu^2\right)}{2c^2}\right] I_0\left(\frac{s_Z\, \nu}{c^2}\right), \quad s_Z \geq 0 \tag{2.24}$$

The Rayleigh distribution is a special case of Ricean distribution. If $\nu = 0$, the Ricean pdf is transformed into a Rayleigh pdf. That is, if

$$S_I \sim \mathcal{N}(0, c^2)$$
$$S_Q \sim \mathcal{N}(0, c^2)$$

then S_Z is Rayleigh distributed where $c > 0$ is the scale parameter:

$$p_{Rayleigh}(s_Z;\, c) = \frac{s_Z}{c^2} \exp\left[-\frac{{s_Z}^2}{2c^2}\right], \quad s_Z \geq 0 \tag{2.25a}$$

$$F_{Rayleigh}(s_Z;\, c) = 1 - \exp\left[-\frac{{s_Z}^2}{2c^2}\right], \quad s_Z \geq 0 \tag{2.25b}$$

The Rayleigh pdf and CDF are plotted in Figure 2.7. The k^{th} moment of Rayleigh distributed random variable is as follows

$$E\left\{S_{Z,\,Rayleigh}^{\;k}\right\} = c^k\, 2^{k/2}\, \Gamma\left(1+\frac{k}{2}\right) \tag{2.26}$$

where $\Gamma(.)$ is the gamma function.

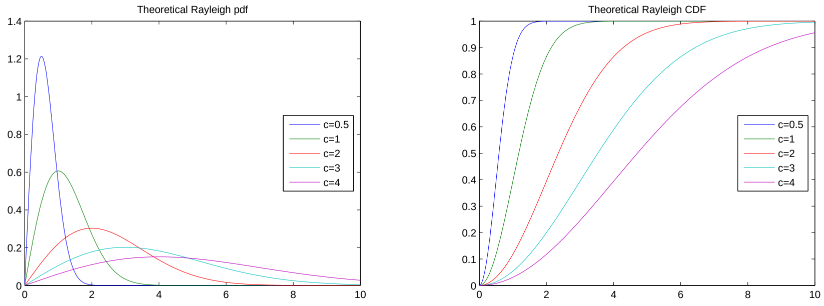

(a) (b)

Figure 2.7: (a) Theoretical Rayleigh pdf, (b) Theoretical Rayleigh CDF

Moreover, the intensity of a complex Gaussian clutter is denoted by S_P as in 2.27 and it is exponentially distributed.

$$S_P = {S_I}^2 + {S_Q}^2. \tag{2.27}$$

For high range resolution systems, since the I and Q components deviate from Gaussian, the deviation of amplitude statistics from Rayleigh (or Ricean) is obvious. As explained before, the spiky characteristic of the clutter amplitude due to high resolution makes the tail of the pdf rise up. Hence, distributions with longer tails are required to model clutter amplitude of high resolution. There are several distributions proposed to model the non-Rayleigh clutter amplitude. Among them, Log-normal and Weibull are the most common ones.

The Log-normal distribution is used to model the clutter amplitude in [3], [6], [32]. It has two parameters, namely, the mean μ, and the standard deviation σ. The pdf and CDF of

Log-normal distribution are given in (2.28) and plotted in Figure 2.8.

$$p_{Log-normal}(s_Z;\ \mu,\sigma) = \frac{1}{s_Z\sqrt{2\pi\sigma^2}}\exp\left[-\frac{(\ln s_Z-\mu)^2}{2\sigma^2}\right],\quad s_Z \geq 0 \tag{2.28a}$$

$$F_{Log-normal}(s_Z;\ \mu,\sigma) = \frac{1}{2}\left[1+\operatorname{erf}\left(\frac{\ln s_Z-\mu}{\sqrt{2\sigma^2}}\right)\right],\quad s_Z \geq 0 \tag{2.28b}$$

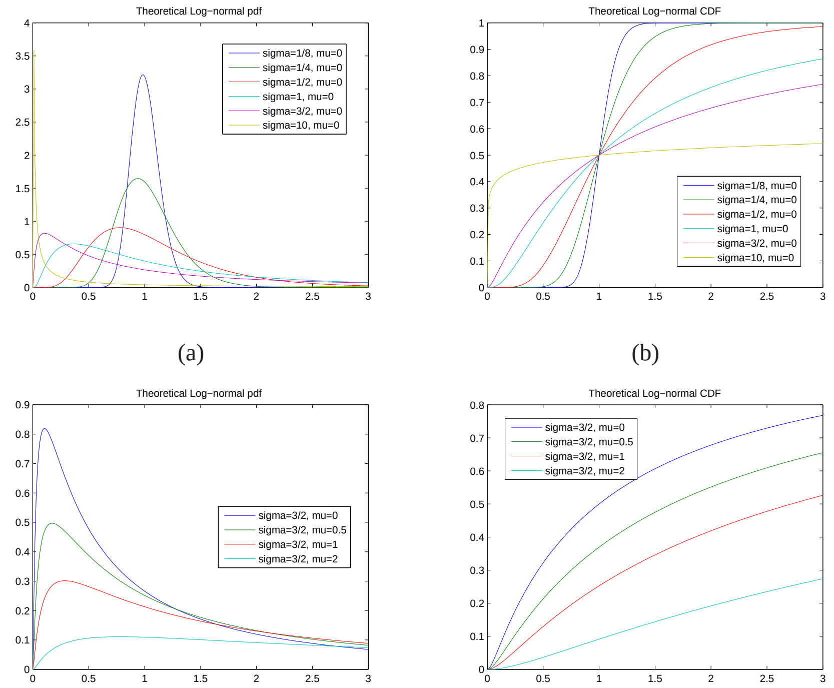

(a) (b)

(c) (d)

Figure 2.8: Theoretical Log-normal pdf and CDF

The k^{th} moment of a Log-normal random variable is

$$E\left\{S_{Z,\,Log-normal}^{\ k}\right\} = \exp\left[k\mu+\frac{1}{2}k^2\sigma^2\right] \tag{2.29}$$

Sometimes the tail of the Log-normal pdf is too long for clutter amplitude to fit [9]. In this case, the Weibull pdf, whose tail may be lighter than that of Log-normal, but still longer than Rayleigh, can be used to model clutter amplitude. Weibull distribution is a two-parameter distribution, where $a > 0$ is the scale parameter, and $b > 0$ is the shape parameter (2.30). As

b decreases, the tail becomes heavier. Figure 2.9 shows how the tail of the pdf changes with b. It can be inferred from the figure that it is the shape parameter which gives the Weibull distribution its flexibility. It is also important to note that Rayleigh is a special case of Weibull distribution for $b = 2$.

$$p_{Weibull}(s_Z;\ a, b) = b\, a^{-b} s_Z^{\ b-1} \exp\left[-\left(\frac{s_Z}{a}\right)^b\right], \quad s_Z \geq 0 \tag{2.30a}$$

$$F_{Weibull}(s_Z;\ a, b) = 1 - \exp\left[-\left(\frac{s_Z}{a}\right)^b\right], \quad s_Z \geq 0 \tag{2.30b}$$

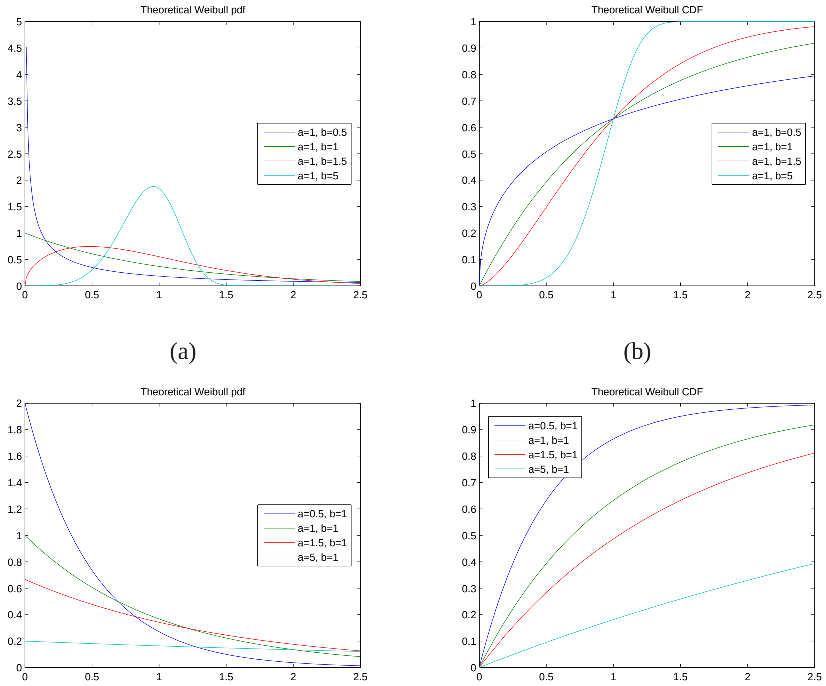

(a) (b)

(c) (d)

Figure 2.9: Theoretical Weibull pdf and CDF

The k^{th} moment of Weibull random variable is given by

$$E\left\{S_{Z,\,Weibull}^{\ k}\right\} = a^k\, \Gamma\left(1 + \frac{k}{b}\right). \tag{2.31}$$

2.3.2 Temporal Statistics of Clutter

So far, the spatial behavior of clutter, i.e., the change of clutter from one range cell to another, has been examined. However, the clutter in a range cell may also vary in time. Hence, in order to maximize the detection probability for a fixed false alarm probability, the detection threshold level should be adjusted in time considering the variation of clutter in a given range cell. That is, the knowledge of temporal behavior of clutter is important in terms of target detection mechanisms, as well as the spatial statistics. Thus, in this section, the temporal variations of clutter will be studied.

It is important to make the distinction between the reasons of spatial and temporal variations of clutter. The spatial variations of clutter are associated with the land cover, i.e., the layout of the backscatterers, such as buildings, trees, agricultural fields in the illuminated range cells. As explained in Section 2.3.1, the range resolution of the system is the main parameter that affects the spatial behavior of clutter. On the other hand, the temporal behavior of clutter mainly depends on the fluctuations of the backscatterers in a given range cell over time. However, it is important to consider the indirect effect of land cover on the temporal behavior of clutter. For instance, a range cell dominated by a stationary scatterer, such as a building, exhibits very small or no fluctuation in time, where a range cell containing trees usually exhibits more fluctuations. Thus, it can be concluded that the range resolution of the system also affects the temporal statistics of clutter by changing the contents of range cells [8].

Apart from the range resolution, it is self-evident that the weather condition leads to temporal fluctuations in clutter. For example, the wind causes the clutter amplitude to change in time. Here, a question may arise on how long the clutter must be observed in order to extract its temporal behavior. It is obvious that the observation time must be sufficiently long. However, the length of the observation time must be chosen according to the focus of interest. For example, a long-term observation on the order of days may help monitor the seasonal trends of clutter, where an observation length on the order of seconds may provide the short-term characterization of clutter [12]. However, it can be predicted that the observation length can be practically limited by the maximum allowable data record length of the data acquisition system [8].

In order to obtain the temporal statistics of clutter, the returns from M pulses are analyzed for a given cell. That is, the slow-time dimension of the data storage matrix is of interest (Figure 2.10). If the random variable T_Z denotes the clutter amplitude of a fixed range cell over a period of time ('T' stands for temporal), the distributions proposed for T_Z are examined in the following subsection.

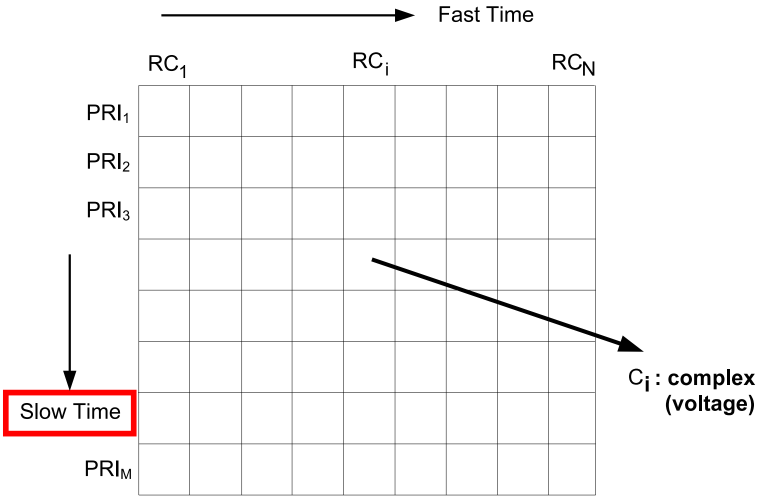

Figure 2.10: Data matrix for temporal statistics of clutter

2.3.2.1 Temporal Clutter Models

Also for the temporal statistics of clutter, a number of models are proposed in the literature. For the temporal case, the amplitude of clutter is considered to be either Ricean or Rayleigh distributed [8], [12].

The return from scatterers in a range cell can be classified into two types: a steady component and a diffuse component. The former is the return from fixed discrete objects such as buildings and it does not change in time; where the latter is formed by the returns from movable objects such as wind-blown foliage and it contributes to the nonstationarity of the clutter [8]. A range cell may contain one or both of these components.

The clutter amplitude with a large steady component and a diffuse component in a range cell is modeled with a Ricean distribution. That is,

$$p_{Ricean}(t_Z;\ c,\nu) = \frac{t_Z}{c^2}\exp\left[-\frac{\left({t_Z}^2+\nu^2\right)}{2c^2}\right] I_0\left(\frac{t_Z\,\nu}{c^2}\right), \quad t_Z \geq 0 \tag{2.32}$$

On the other hand, the diffuse component itself is modeled with a Rayleigh distribution, which is a special case of Ricean distribution.

$$p_{Rayleigh}(t_Z;\ c) = \frac{t_Z}{c^2}\exp\left[-\frac{{t_Z}^2}{2c^2}\right], \quad t_Z \geq 0 \tag{2.33a}$$

$$F_{Rayleigh}(t_Z;\ c) = 1 - \exp\left[-\frac{{t_Z}^2}{2c^2}\right], \quad t_Z \geq 0 \tag{2.33b}$$

As explained previously, the temporal behavior of clutter depends on the land cover and range resolution as well as the weather condition. The effect of range resolution on the temporal behavior can be exemplified as follows: If a fixed large scatterer is isolated from small moving scatterers as the range resolution improved, the range cell with moving scatterers approaches Rayleigh model where the range cell with the large scatterer is Ricean distributed. Consequently, it can be concluded that the temporal behavior of clutter may change from one range cell to another.

2.3.3 Space-Time Compound Clutter Statistics

Since both the spatial and temporal statistics of clutter play an important role in target detection mechanisms, it is sometimes useful to define the clutter as a function of both space and time. Based on this, a different approach to clutter modeling is introduced: the *compound clutter model*. The nature of the compound clutter model enables both temporal and spatial correlation properties of the returns to be taken into account [11], [27]. In this model, the clutter amplitude is decomposed into two independent processes, which are related to time and space.

The first component, the *speckle* represents the spatial voltage fluctuations in the fast time dimension. The speckle component generally exhibits a short decorrelation time. The speckle is modeled so that the mean of its power level $E\left\{|S|^2\right\} = 1$ [28]. The underlying power level of the clutter is related to the second component, namely the *texture*. The texture, which represents the ‘local power’ variation of the return signal, decorrelates in a relatively longer time [21]. The ‘local mean voltage’ level, which is square root of the texture, modulates the clutter amplitude, hence it is called the *modulating component*.

Accordingly, the clutter amplitude can be written as

$$C_Z = \sqrt{\tau} \times |S| \tag{2.34}$$

where

$|S|$: amplitude of the speckle

τ : texture

$\sqrt{\tau}$: modulating component

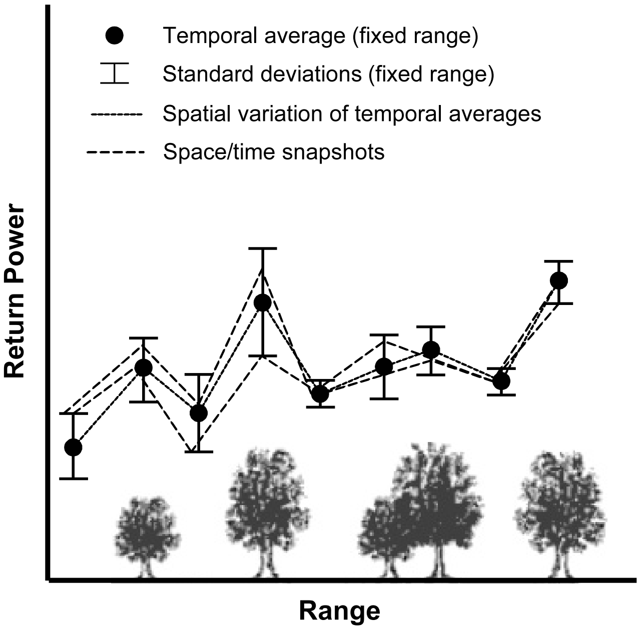

Figure 2.11: Space - time compound model [21]

Figure 2.11 illustrates the concept of space-time compound clutter model [21]. For a fixed range, the temporal average of the return power is calculated. This corresponds to the ‘local mean power’, which is a function of range. Then, the spatial variation of temporal averages is used to construct a space-time compound model. That is, given the temporal averages of local amplitudes, the spatial variation of clutter is expressed by the conditional probability

$p\left(c_Z \mid m\right)$ ('C' stands for compound). Here m denotes the local mean voltage, or equivalently the modulating component. Then, the clutter amplitude can be found from (2.35):

$$p\left(c_Z\right) = \int_0^\infty p\left(c_Z \mid m\right)\; p\left(m\right)\; dm. \tag{2.35}$$

2.3.3.1 Compound Clutter Models

The K-distribution is the most widely known model among the space-time compound models. It was first proposed for the sea clutter, but due to its ability of considering both spatial and temporal the correlation properties, it is also applied to the other types of clutter [27]. For the K-distribution, the speckle is Rayleigh distributed, and the texture is modeled with the Gamma or the Chi-square, which is a special form of Gamma [15]. (Accordingly, the modulating component is Root-Gamma or Chi distributed). Then, the clutter amplitude C_Z is K-distributed. In (2.36), the parameters a and ν are the scale and shape parameters, respectively. The shape parameter ν is related to the number of scatterers in a range cell. Hence, lower ν corresponds to smaller number of scatterers in a range cell, which yields a heavier tail due to spiky amplitude characteristics [35].

$$p_K(c_Z;\; a, \nu) = \frac{4}{a\Gamma\left(\nu\right)} \left(\frac{c_Z}{a}\right)^{\nu} K_{\nu-1}\left[2\frac{c_Z}{a}\right], \quad c_Z \geq 0 \tag{2.36a}$$

$$F_K(c_Z;\; a, \nu) = 1 - \frac{2}{\Gamma\left(\nu\right)} \left(\frac{c_Z}{a}\right)^{\nu} K_{\nu}\left[2\frac{c_Z}{a}\right], \quad c_Z \geq 0. \tag{2.36b}$$

The k^{th} moment of K random variable is given in (2.37).

$$E\left\{C_{Z,K}^{\;k}\right\} = a^k \frac{\Gamma\left(\nu + \frac{k}{2}\right)\Gamma\left(1 + \frac{k}{2}\right)}{\Gamma\left(\nu\right)} \tag{2.37}$$

K-distribution is also used to model the clutter intensity c_P [20]. The K-distributed clutter intensity is given as follows

$$p_K(c_P;\; a, \nu) = \frac{2}{a^{\nu+1}\Gamma\left(\nu\right)}\, c_P^{\;\frac{\nu-1}{2}}\, K_{\nu-1}\left[2a c_P^{\;\frac{1}{2}}\right], \quad c_P \geq 0. \tag{2.38}$$

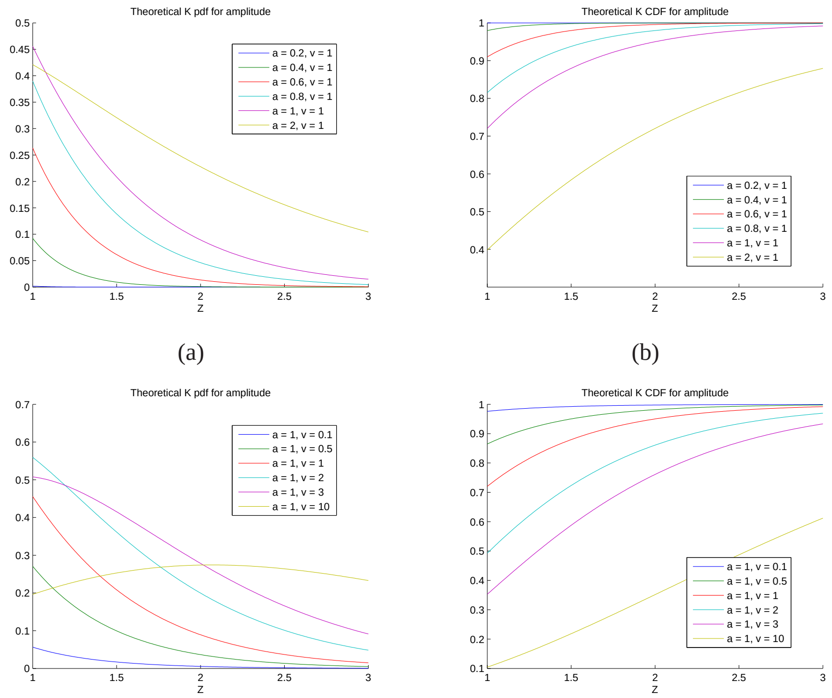

(a) (b)

(c) (d)

Figure 2.12: Theoretical K pdf and CDF

The K-distribution is widely used to model the clutter amplitude. However, the speckle amplitude and the texture may deviate from Rayleigh and Gamma distributions, respectively. As a result, the K-distribution loses its validity. For example, consider the texture component τ modeled with the Gamma distribution as in

$$p_{\Gamma}(\tau;\ a,\nu) = \frac{1}{a\Gamma(\nu)}\left(\frac{\tau}{a}\right)^{\nu-1}\exp\left(-\frac{\tau}{a}\right), \quad \tau \geq 0 \ and \ a = \frac{\mu}{\nu} \tag{2.39}$$

where μ is the mean and μ^2/ν is the variance of the texture. In [16], it has been stated that the texture may deviate from the Gamma distribution due to bad weather conditions. Moreover, if the parameter ν goes to ∞, the variance goes to zero and the texture τ approaches the mean μ. (This corresponds to the homogeneous texture and the parameter ν can be considered as a measure of texture homogeneity [28].) In this case, the clutter amplitude is a Rayleigh speckle multiplied with a constant modulating component, which results in another Rayleigh pdf instead of a K pdf.

From the point of speckle, the range resolution plays a dominant role in the distribution of the speckle amplitude. As the range resolution is improved, the speckle amplitude deviates from Rayleigh. Hence, the K-distribution is no longer a valid model for clutter amplitude.

Consequently, the need arises for defining general statistical models for both the speckle and modulating component. The generalized Gamma model will be an appropriate choice for both components, since many pdfs can be derived from this model. The generalized Gamma model $G\Gamma$ is given by (2.40), where $a > 0$, $b > 0$, and $\nu > 0$ are the scale, shape, and power parameters, respectively:

$$p_{G\Gamma}(x;\ a, b, \nu) = \frac{b}{a\Gamma(\nu)}\left(\frac{x}{a}\right)^{b\nu-1}\exp\left[-\left(\frac{x}{a}\right)^{b}\right], \quad x \geq 0. \tag{2.40}$$

Adjusting the parameters in (2.40), Gamma, Weibull, Rayleigh, Exponential, and Log-normal pdf can be obtained [16]:

- X $\sim G\Gamma(b = 1) \Rightarrow$ X $\sim$ Gamma (Γ) distributed
- X $\sim G\Gamma(\nu = 1) \Rightarrow$ X $\sim$ Weibull (W) distributed
- X $\sim G\Gamma(\nu = 1\ \&\ b = 2) \Rightarrow$ X $\sim$ Rayleigh (R) distributed
- X $\sim G\Gamma(\nu = 1\ \&\ b = 1) \Rightarrow$ X $\sim$ Exponential (E) distributed
- X $\sim G\Gamma(\nu \to \infty\ \&\ b \to 0) \Rightarrow$ X $\sim$ Log-normal (LN) distributed

For the generalized model, the distribution of speckle amplitude is denoted by

$$p_{G\Gamma}(c_Z \mid m;\ b_1, \nu_1) = \frac{b_1}{m\Gamma(\nu_1)}\left(\frac{c_Z}{m}\right)^{b_1\nu_1-1}\exp\left[-\left(\frac{c_Z}{m}\right)^{b_1}\right], \quad c_Z \geq 0 \tag{2.41}$$

and the pdf of the modulating component by

$$p_{G\Gamma}(m;\ a, b_2, \nu_2) = \frac{b_2}{a\Gamma(\nu_2)}\left(\frac{m}{a}\right)^{b_2\nu_2-1}\exp\left[-\left(\frac{m}{a}\right)^{b_2}\right], \quad m > 0 \tag{2.42}$$

Then, the pdf of clutter amplitude is called the *generalized compound (GC) model* [16] and it is obtained from

$$p_{GC}\left(c_Z\right) = \int_0^{\infty} p_{G\Gamma}\left(c_Z \mid m\right)\, p_{G\Gamma}\left(m\right)\, dm \tag{2.43}$$

Various clutter models can be obtained by adjusting the parameters of the GC model. For example, Weibull-speckle Gamma-texture compound model is a special case of the GC model. In this case, the deviation of speckle from the Rayleigh distribution is taken into account. On the other hand, for the *compound Gaussian (CG) models*, the speckle amplitude is Rayleigh distributed, but the texture differs. The K-model given previously in (2.36) and the generalized K model with Log-normal texture [28] are examples of the *GC* model. The *Generalized K (GK) model* is an important special case of the GC model, since both K and Weibull results from this model.

- X ~ $GC\left(b_1 = b_2 = b\right) \Rightarrow$ X ~ Generalized K (GK) distributed
- X ~ $GK\left(b = 2\ \&\ \nu_1 = 1\right) \Rightarrow$ X ~ K (K) distributed
- X ~ $GK\left(\nu_1 = 1\ \&\ \nu_2 = 0.5\right) \Rightarrow$ X ~ Weibull (W) distributed

2.3.4 Empirical Distribution Fitting

So far, the statistical distributions proposed to model radar clutter both in space and time have been presented. Once an experimental clutter data set is constructed, there are various methods used to check whether it fits a theoretical model or not. In the first instance, various exploratory tools based on graphical characteristics of the distributions, such as histogram, quantile - quantile (Q-Q) plot, etc., can be applied. This will help hold a rudimentary view about the distribution of experimental data. However, it will be definitely not enough to conclude. Hence, the preliminary guess about the empirical distribution should be verified by applying more formal methods, such as goodness-of-fit (GoF) tests. In this section, these complementary empirical fitting methods will be explained briefly.

At first, let **x** be the vector of empirical data samples, where x_i may represent the clutter amplitude or I/Q component in either slow time or fast time domain.

$$\mathbf{x} = \left[x_1 \cdots x_n\right] \tag{2.44}$$

In order to extract the underlying distribution of the empirical clutter data, it is usually better to plot the histogram of $\mathbf{x}$ and visually compare it to the pdfs of various theoretical distributions. By this way, some irrelevant distributions may be immediately eliminated, while some distributions may stand out.

During this preliminary step, some other measures can also be made use of. For instance, consider *skewness* and *kurtosis*, which are the 3rd and the 4th order normalized central moments, respectively. The skewness, given in (2.45a), is related to the asymmetry of a distribution around its mean. On the other hand, the kurtosis given in (2.45b) is a measure of relative peakedness or flatness of a distribution. Since both parameters are exactly equal to zero for Gaussian distribution, deviation of these parameters from zero can be considered as a measure of deviation from Gaussianity.

$$\gamma_3^Z = \frac{E\left\{(Z-\mu_Z)^3\right\}}{E\left\{(Z-\mu_Z)^2\right\}^{3/2}} \tag{2.45a}$$

$$\gamma_4^Z = \frac{E\left\{(Z-\mu_Z)^4\right\}}{E\left\{(Z-\mu_Z)^2\right\}^{2}} - 3 \tag{2.45b}$$

Having obtained a first guess about the theoretical model for the empirical data, GoF tests based on the statistical theory can be applied. Hence, first, a binary hypothesis test problem [1] is constructed where the *null* and *alternative* hypotheses are defined as follows:

$H_0 \sim$ Empirical data follow the specified distribution
$H_A \sim$ Empirical data do NOT follow the specified distribution.

The decision whether to accept or reject H_0 can be made based either on the pdf of the distribution as in the *area tests*, or on the CDF as in the *distance tests*.

There are various GoF tests such as Chi-Square (CS), Anderson-Darling (AD), Kolmogorov-Smirnov (KS). Among them, KS test is a commonly used tool to check goodness of fit due to its applicability to any distribution and straightforward computation. KS test depends on the comparison of empirical and hypothetical CDFs rather than their pdfs. In order to construct the empirical and hypothetical CDFs, first the empirical data, $\mathbf{x}$, are sorted in the ascending

---

[1] Hypothesis test terminology is given in Appendix B

order. The resulting empirical CDF is a step-function that increases by $1/n$ at each data value x_i (Figure 2.13). On the other hand, the hypothetical CDF is evaluated at each data value.

The test statistic of KS test is a measure of the maximum absolute difference between the empirical and hypothetical CDFs and is given by [2]

$$D_n = \sup_{x_i} |S_n(x_i) - F(x_i)| \,, \tag{2.46}$$

where,

x_i: Ordered data points; $i = 1, \ldots, n$
$S_n(x)$: Empirical CDF (step function)
$F(x)$: Hypothetical CDF.

D_n can be alternatively expressed as

$$D_n = \max_{1 \le i \le n} \left(F(x_i) - \frac{i-1}{n}, \frac{i}{n} - F(x_i) \right). \tag{2.47}$$

Once the test statistic is evaluated for the empirical data, it is compared to the *critical value* given in the standard KS table for some significance level α and sample size n. The critical values in the standard KS test table do not depend on the distribution which is being tested. (Standard critical values for KS test are provided in [1].)

Next, the decision is made according to the following rule:

$$\begin{aligned} \text{Reject } H_0, &\quad \text{if } D_n > \text{critical value} \\ \text{Accept } H_0, &\quad \text{if } D_n < \text{critical value} \end{aligned}$$

That is, if the difference between the empirical and hypothetical CDF exceeds some critical value, the empirical data cannot be said to follow the hypothetical distribution, hence it is rejected. In contrast, if the difference is below that critical value, the null hypothesis cannot be rejected.

---

[2] The *supremum*, or equivalently the *least upper bound*, of an ordered set S is the least element (not necessarily in S) which is greater than or equal to each element of S.

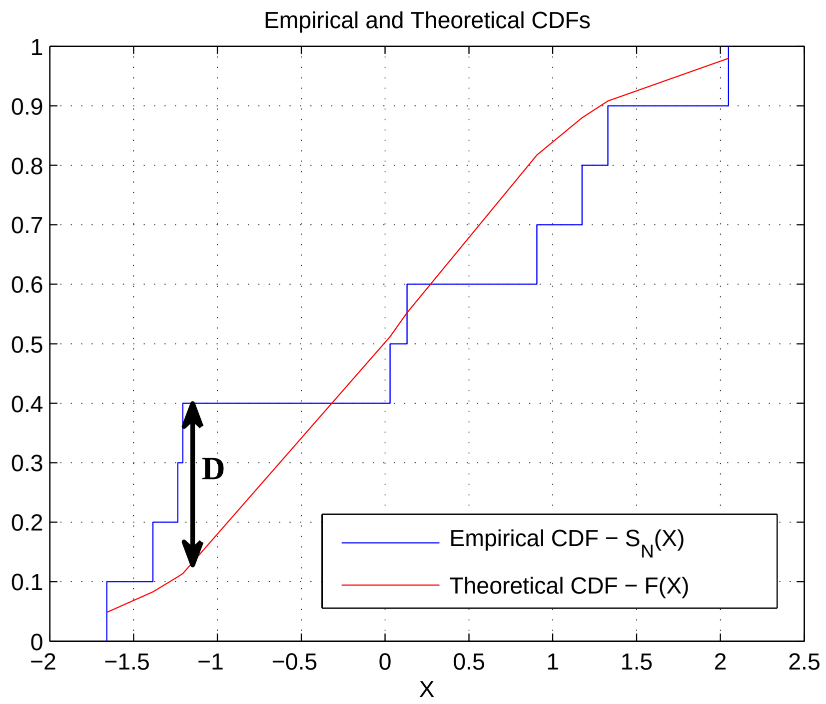

Figure 2.13: Kolmogorov-Smirnov test statistic

The main drawback of the KS test is that the hypothetical distribution should be completely specified, i.e., all its parameters should be determined, in order to evaluate it for each empirical data value. If no parameter of the hypothetical distribution is determined from the empirical data, the test statistic, D_n, is independent of the distribution. However, when the parameters of the hypothetical distribution are not given but instead estimated from the data, the result of the KS test is no more distribution independent [10].

If the standard KS table is used when the parameters are estimated from the data, the confidence level will be higher [10], and the actual significance level will be smaller than the value associated with the standard table [5]. Smaller α corresponds to a larger critical value, which makes it harder to reject the null hypothesis. This can be interpreted as the hypothesized CDF is made closer to the empirical data by estimating the parameters from the data. In this case, the probability of making an error by failing to reject the null hypothesis (i.e., Type-II error) may increase. Hence, the use of standard KS test table should be avoided when the parameters are estimated from the empirical data.

Similar to the KS test, the knowledge of distribution parameters is required for the AD test, which is a modified version of the KS test for a better performance at the tails of the distribution. Besides, AD test can only be applied for a few specific distributions. As opposed to the AD and KS tests, the CS test does not require to completely specify the distribution parameters. However, it is not a powerful test for small number of samples unlike AD and KS tests.

Considering the main drawbacks and superiorities of the GoF tests, a modified KS test with the extension of Monte Carlo approach will be used in this study. The principle of Monte Carlo approach in KS test can be explained as follows:

1. KS test statistic is computed for the empirical data and the hypothetical model. In this step, the hypothetical model is constructed by estimating the parameters from the empirical data. The parameters can be estimated by means of Method of Moments (MoM) [17], in which the k^{th} moment is equated to the k^{th} sample moment of the empirical data as in (2.48), t being the number of unknown parameters to be estimated.

   $$E\left\{X^k\right\} = \frac{1}{n}\sum_{i=1}^{n} x_i^k, \quad k = 1, ..., t \tag{2.48}$$

   Besides the MoM estimates, maximum likelihood (ML) estimates can be used as the distribution parameters.

2. A large number of synthetic data sets is generated, so that each set follows the hypothetical model with the parameters estimated for the empirical data in Step 1.

3. For each synthetic data set, its own parameters are estimated. Then, each data set is fit to the hypothetical model with the new estimated parameters. The KS test statistic is recorded for each fit. That is, the distribution of D_n is obtained for the case of estimated parameters (Figure 2.14).

4. The fraction of time in which the resulting KS test statistic for synthetic data is larger than or equal to that of the empirical data is determined. This fraction gives the *empirical p-value, p*.

5. Finally, the empirical p-value found by Monte Carlo method in Step 4 is compared to the significance level α:

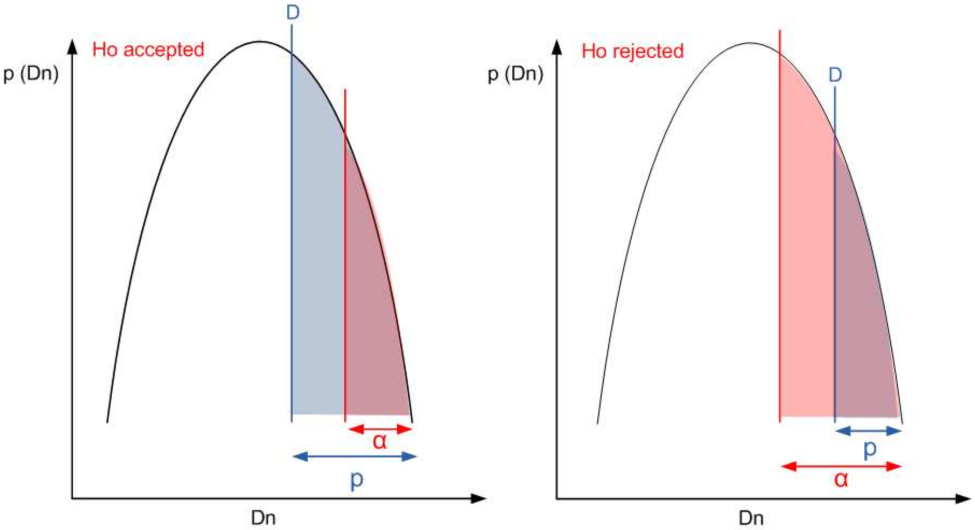

Figure 2.14: Distribution of D_n

$$\text{If } \alpha > p, \quad H_0 \text{ is rejected}$$
$$\text{If } \alpha < p, \quad H_0 \text{ is NOT rejected}$$

This is equal to comparing the new critical value to the empirical test statistic, D.

In the literature, there are many modifications of the standard KS test with tables extracted based on the Monte Carlo simulations for different distributions with unknown parameters. For instance, Lilliefors test checks whether the empirical data samples come from a distribution in the Gaussian family when the parameters are not specified [2]. Similarly, in [4] and [5], modified tables for Weibull and Gamma distributions are presented.

2.4 Clutter Reflectivity

In this section, the relative intensity which mainly depends on the type of clutter is presented. In order to explain the relative intensity, first, consider the radar power equation

$$P_R = \frac{P_T \cdot G_T \cdot G_R \cdot \lambda^2 \cdot \sigma_C}{(4 \cdot \pi)^3 \cdot R^4 \cdot L}, \tag{2.49}$$

where

P_R : Received power (W)

P_T : Transmitted power (W)

G_T : Gain of the TX antenna (W/W)

G_R : Gain of the RX antenna (W/W)

λ : Wavelength (m)

σ_C : Radar cross section (RCS) (m^2)

R : Range (m)

L : Losses (W/W).

The equation in (2.49) can also be written in terms of the clutter-to-noise ratio (CNR) as follows

$$CNR = \frac{P_T \cdot G_T \cdot G_R \cdot \lambda^2 \cdot \sigma_C}{(4 \cdot \pi)^3 \cdot R^4 \cdot k \cdot T \cdot B \cdot F \cdot L}, \tag{2.50}$$

where

k : Boltzmann constant, $1.38 \cdot 10^{23}$ (W/(Hz °K))

T : Temperature (°K)

B : Effective noise bandwidth (Hz)

F : Noise factor.

As it can be seen from the radar power equations above, the power of the received signal is proportional to the radar cross section (RCS) of the illuminated region. For the surface clutter (such as ground and sea returns), the return power depends on the area illuminated, where it depends on the illuminated volume for the volume clutter (such as weather and chaff).

In order to describe the surface or volume clutter independent of the illuminated area or volume, respectively, the *normalized radar cross section (NRCS)* is defined. The NRCS is also referred to as the *normalized radar reflectivity* or the *backscattering coefficient* [33].

For the surface clutter, NRCS can be obtained from

$$\sigma_0 = \frac{\sigma_C}{A_C}, \tag{2.51}$$

where σ_C is the RCS of clutter and A_C is the area of the illuminated region [33].

For a small azimuthal beamwidth of θ and a low grazing angle [3] of ψ, the area of a resolution cell at range R is calculated from

$$A_C = \frac{R \cdot \theta \cdot R_{res}}{\cos\psi}, \tag{2.52}$$

where $\mathrm{R_{res}}$ is the range resolution of the system.

Similarly, the volume clutter is described by the *clutter RCS per unit volume*, η, given in (2.53).

$$\eta = \frac{\sigma_C}{V_C} \tag{2.53}$$

Finally, in [9] and [33], it is stated that the NRCS for land clutter is greater than that of the sea and weather clutters. Among the types of land clutter, the cities and the mountains are reported to have the largest σ_0, where the agricultural fields and deserts have smaller σ_0.

---

[3] Grazing angle is the angle between the surface and the incoming radar illumination.

CHAPTER 3

EXPERIMENTAL DATA ACQUISITION AND DATA PROCESSING

The aim of this thesis is to perform the analyses discussed so far on experimental radar clutter data. Hence, a data acquisition set-up is established in order to make clutter measurements. After the whole system is implemented and its operation is verified in the laboratory, measurements are taken in the open terrain.

In this chapter, the general block diagram of the data acquisition system is given and the operation of the whole system is explained. The specifications and limitations of each block are discussed briefly. Further details about the data acquisition system are given in Kılıçoğlu's thesis [37].

3.1 General Block Diagram of the Data Acquisition System

The experimental radar system, which is used in this study for data acquisition, is constructed by using commercial off-the-shelf (COTS) test equipments. The transmitter unit is composed of:

- *MATLAB* as the waveform generator tool,
- *Agilent E8267D PSG Vector Signal Generator* [38] as the transmitter,
- *Agilent HP8348A Microwave Amplifier* [39] as the high power transmitter amplifier, and

- *GAH-1042* or *DRH-412* [1] as the transmitting antenna;

while the receiver unit is composed of:

- *GAH-1042* or *DRH-412* as the receiving antenna,
- Two cascaded *AML218L1502* [40] as the low noise amplifier (together with a 12V DC power supply),
- **Receiver option 1:**
  - *Agilent E4446A PSA Spectrum Analyzer* [41], [42] as the receiver together with
  - *Agilent 89601A Vector Signal Analysis Software* [43],

  Receiver option 2:
  - *Agilent N9010A EXA Signal Analyzer* [44], [45] as the receiver itself,
- *MATLAB* as the signal processing tool.

A computer is utilized, on which MATLAB, Agilent 89601A Vector Signal Analysis Software, Agilent Waveform Download Assistant, and other control interfaces of the COTS equipments, such as Agilent IO Connection Expert, are installed. The vector signal generator is connected to the computer via an Ethernet cable, and the spectrum analyzer (in option 1) or the signal analyzer (in option 2) is connected to the computer via USB interface (Figure 3.1 and Figure 3.2). These connections make the remote control of the instruments possible. The connections to the instruments can be verified by Agilent IO Connection Expert. Also, a graphical user interface is developed in MATLAB in order to control the data acquisition and measurement analyses via a user-friendly environment.

The general block diagrams of the system for both receiver alternatives are depicted in Figure 3.1 and Figure 3.2. A brief explanation of the system operation is as follows: First, the I and Q data of the transmit signal are generated in MATLAB and downloaded to the vector signal generator by means of Waveform Download Assistant Toolkit functions. Next, the baseband generator of the vector signal generator converts the digital I and Q data into analog

---

[1] Due to antenna reciprocity, these antennas can be used interchangeably for the transmitter and the receiver.

baseband signals. Then, the I/Q modulator of the vector signal generator modulates the baseband signal to the desired center frequency at the desired output power level. The resulting RF signal is amplified through a high power amplifier and routed to the transmitting antenna. On the receiver side, the returns from the scatterers are captured by the receiving antenna. The received signal is amplified by a cascaded two-stage low noise amplifier and sent to one of the two alternative receivers:

- For the first option, in which PSA Spectrum Analyzer together with Vector Signal Analyzer Software forms the receiver, the spectrum analyzer downconverts the RF signal into IF and then converts into digital. The digitized IF signal is sent to the Vector Signal Analyzer software, which performs the digital downconversion.
- For the second option, EXA Signal Analyzer performs analog downconversion, IF digitization and digital downconversion operations itself.

Finally, the digital baseband I and Q samples from either receiver options are saved into a file and then processed in MATLAB.

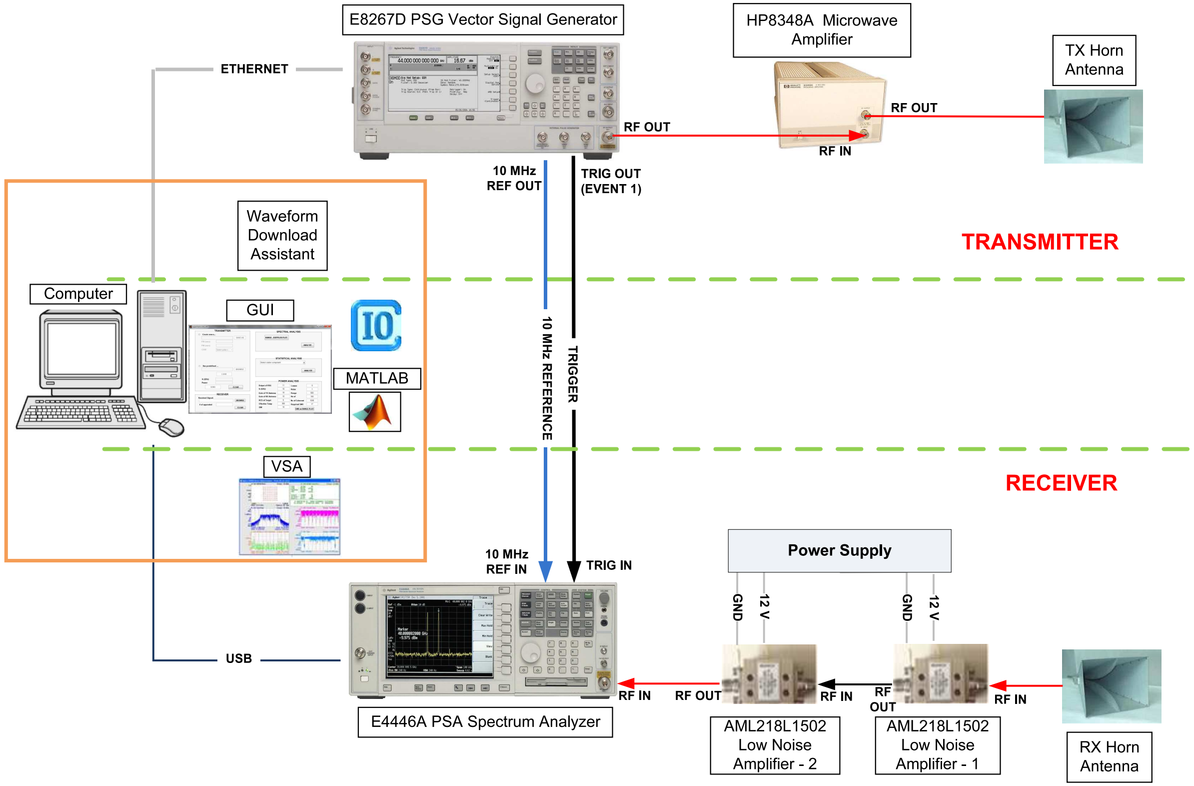

Figure 3.1: General block diagram of the data acquisition system - Receiver option 1

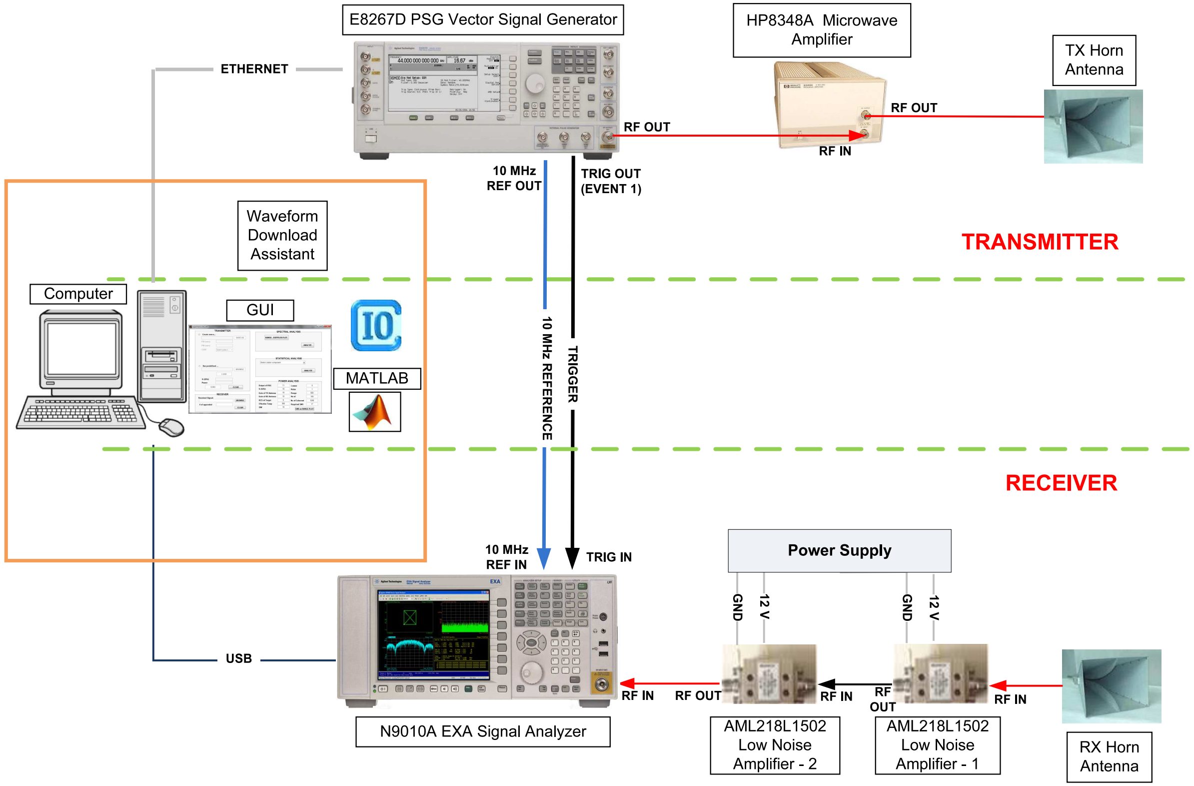

Figure 3.2: General block diagram of the data acquisition system - Receiver option 2

Two important connections in both Figure 3.1 and Figure 3.2 should be pointed out, namely the 10 MHz reference and trigger connections between the vector signal generator and the spectrum/signal analyzer.

1. If both of the vector signal generator and the spectrum/signal analyzer use their own internal reference oscillators in the same system, this may yield arbitrary frequency reading errors. In order to avoid these errors, all the oscillators in the system should have a common reference. Hence, the 10 MHz reference output of the vector signal generator should be connected to the 10 MHz reference input of the spectrum/signal analyzer, or vice versa. The former configuration is used in this system, and the 10 MHz reference source of the spectrum/signal analyzer is set to *external*. Here, it is important to check that an annunciator like *EXT REF* appears on the spectrum/signal analyzer and vector signal analyzer screens.
2. In radar systems, the delays of the echoes are important since they determine the range of the targets. Hence, the receiver (in this system, the spectrum analyzer and vector signal analyzer together, or the signal analyzer itself) should know when the transmission begins. This information can be provided to the receiver via a trigger pulse which is set to start at the beginning of the transmit signal. In this system, the trigger pulse is defined by a marker waveform and given out from the **EVENT1** output of the vector signal generator. (Defining marker waveforms are explained in detail in Section 3.2.1.2.) Then, if external triggering option is selected for the spectrum/signal analyzer and the **EVENT1** output of the vector signal generator is connected to its **TRIG IN** input, the measurement waits for the trigger pulse from the vector signal generator.

In the following sections, each block of the experimental radar system is explained starting with the elements of the transmitter unit. In Figure 3.3, a photo of the experimental radar system can be seen during data acquisition on the roof of METU Electrical and Electronics Engineering Department's Building D.

Figure 3.3: Experimental data acquisition system during measurements

3.2 Transmitter

In this section, the operation principle of the transmitter unit, which is given in Figure 3.4, is explained.

3.2.1 Generation of the Transmit Signal

3.2.1.1 Selecting the Transmit Signal

In this study, various transmitting signals, such as single pulse and phase coded pulses, have been used for system verification and experimental data analyses.

The phase coded pulses are constructed based on the pulse compression technique. In this technique, high resolution of a short pulse width is combined with the high energy of a long pulse width. Hence, a long pulse which has a bandwidth corresponding to a short pulse is transmitted. In order to achieve this, the pulse is either modulated or coded (e.g. frequency

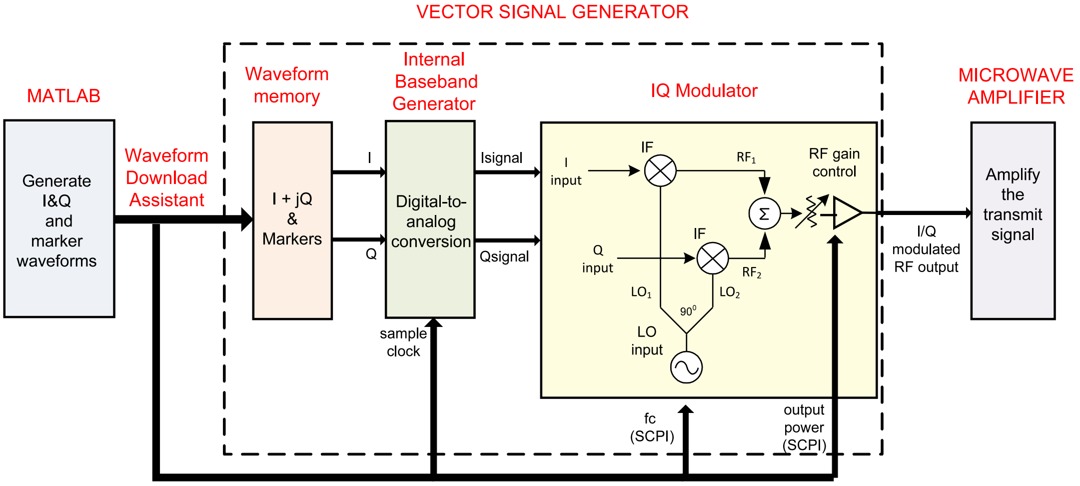

Figure 3.4: Operation principle of the transmitter

modulation and phase-coded pulses). For phase-coded pulses, the pulse width is divided into a number of chips of equal length and each chip is transmitted with a particular phase. The bandwidth of the phase coded pulse is determined by the chip width (or, compressed pulse width), T_{chip}, instead of the pulse width itself. This results in a larger bandwidth and a better resolution achieved with the same energy. Equivalently, for a given range resolution (or chip width) and total pulse energy, if more chips are used, the transmitter power is reduced due to the increased total pulse width.

Here, the pulse compression ratio, PCR, is defined as the ratio of the range resolution of an unmodulated pulse of length τ to that of the modulated or coded pulse of the same length and bandwidth of B. This ratio can be considered as the SNR improvement factor. From (3.1), it can be concluded that if the same pulse width is divided into more chips, the SNR is increased more:

$$PCR = \frac{\frac{c\cdot\tau}{2}}{\frac{c}{2\cdot B}} = B\tau. \tag{3.1}$$

In phase-coded pulses, the phase of each chip is determined according to a phase code. Barker-7, random phase codes, and P4 codes are examples of the phase codes used in this study. Among them, the P4 code is the mostly used one in the experiments. P4 codes can be defined for any number of chips, and the phase of the i^{th} chip, Φ_i, is determined by

$$\Phi_i = \frac{\pi}{L}(i-1)(i-L-1) \quad i = 1, 2, \ldots, L \tag{3.2}$$

where L is the number of chips. In Figure 3.5, the phase history of the 100-chip P4 code is shown as an example. It is also important to note that P4 codes are discrete approximations to linear FM (LFM), which is also a widely used pulse compression technique [18].

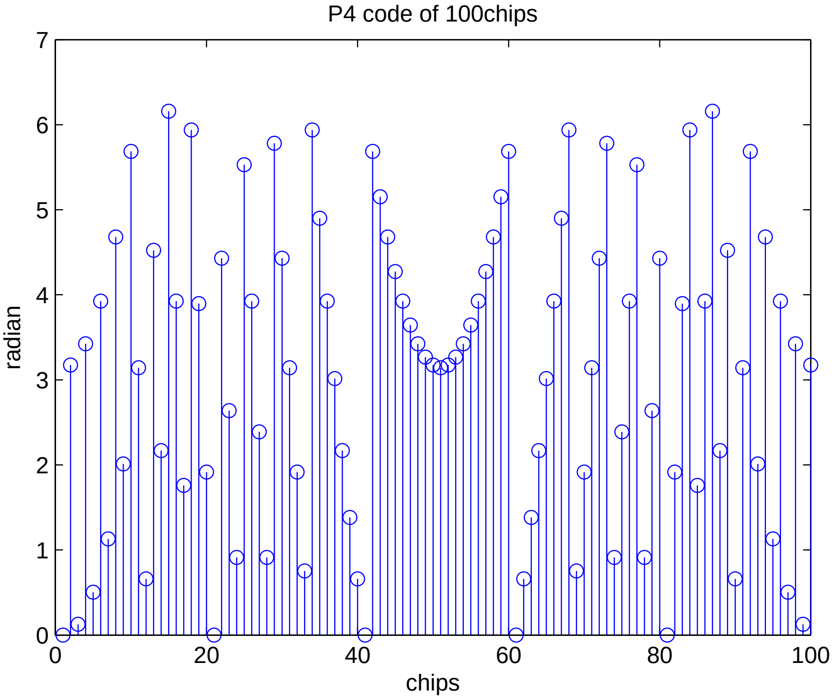

Figure 3.5: Phases of 100-chip P4 code

On the other hand, a single pulse has been widely used to verify the system. However, coded pulses are preferred due to the improvement factor of L they introduce to the SNR.

3.2.1.2 Generation of the IQ Data

Once the transmitting signal is chosen and all its parameters (PW, PRI, pulse code, number of chips) are determined considering the requirements of the experiment, the I and Q waveforms of the signal can be constructed. However, not only the I and Q waveforms, but also the sample clock information and the marker waveforms should also be provided to the vector signal generator (VSG):

1. **Complex IQ data array:**

   In order to define I and Q waveforms of the transmitting signal, first an amplitude array and a phase array are constructed in MATLAB as follows:

$$A = [\alpha_1\ \alpha_2\ \alpha_3\ \cdots\ \alpha_K] \tag{3.3a}$$

$$P = [\phi_1\ \phi_2\ \phi_3\ \cdots\ \phi_K] \tag{3.3b}$$

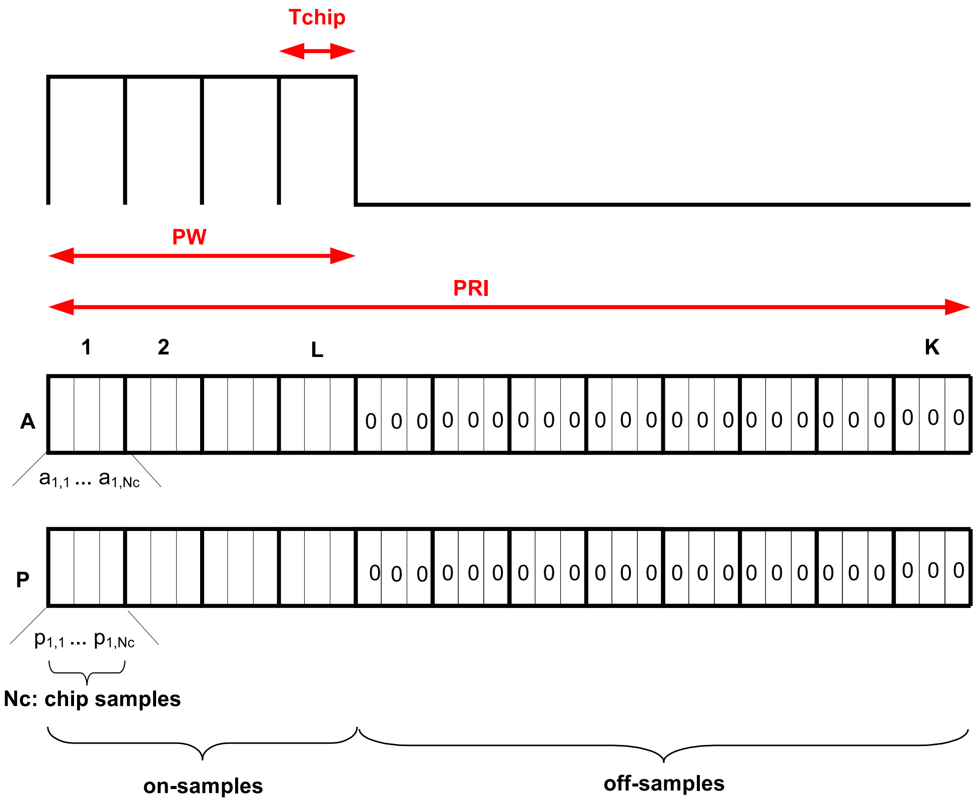

Figure 3.6: Amplitude and phase arrays

If the whole PRI is divided into K chips [2], ϕ_j and α_j in (3.3b) and (3.3a) are the phase and amplitude of the j^{th} chip, respectively. The amplitude array is constructed according to the PW and PRI, while the phase array is constructed according to the phase

---

[2] For simplicity, one PRI is chosen to consist of an integer number of chips.

code of the pulse. Construction of the amplitude and phase arrays of a coded pulse is depicted in Figure 3.6.

Next, the I and Q waveforms are generated as given below

$$I = A \cdot \cos(P) \tag{3.4a}$$

$$Q = A \cdot \sin(P)\,. \tag{3.4b}$$

The VSG accepts the user defined I and Q waveforms in the form of a complex array given in (3.5).

$$IQ = I + j \cdot Q \tag{3.5}$$

According to the specifications of the VSG, the complex IQ data array must consist of at least 60 samples. The maximum number of samples is also specified as 64 Megasamples [38]. The complex IQ waveform downloaded into the waveform memory is repeated continuously.

2. **Sample clock:**

   Together with the I and Q waveforms, the choice of sampling clock for the digital-to-analog converters (DACs) of the baseband generator is provided to the VSG. The maximum sampling rate of the VSG is 100 Msamples/sec, i.e., the time between two samples can be minimum 10 nsec [38].

   Starting from 100 MHz, the maximum sampling rate, for which the number of samples per chip is an integer, is selected for simplicity. For example, consider a pulse of 1 usec PW and 7 chips. The maximum sampling rate is chosen as 98 MHz, for which the number of samples per chip is 14.

3. **Waveform Markers:**

   In order to mark specific positions on the I and Q waveforms, two marker waveforms are defined, one for triggering and one for PULSE/RF blanking. In MATLAB, a marker matrix is constructed, so that each row corresponds to a marker waveform, and the number of columns is equal to the length of the I and Q waveforms. In the beginning, all entries of the marker matrix are zero, which means that no marker is set yet. The markers are activated by setting the necessary entries to 1 (marker polarity is positive).

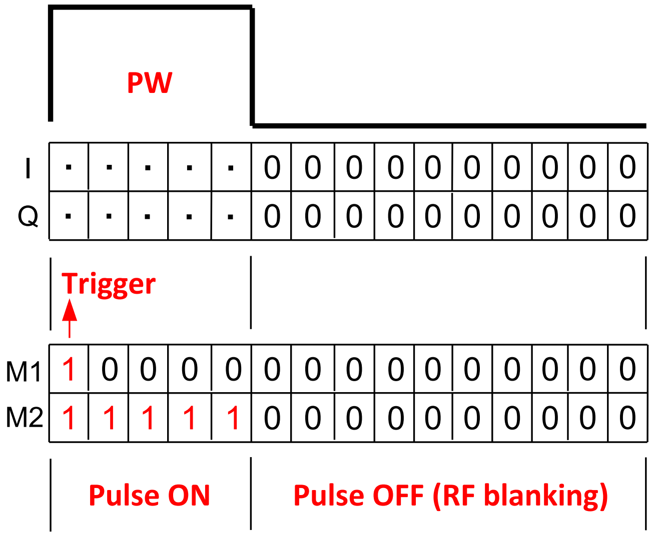

I	·	·	·	·	·	0	0	0	0	0	0	0	0	0	0
Q	·	·	·	·	·	0	0	0	0	0	0	0	0	0	0
M1	1	0	0	0	0	0	0	0	0	0	0	0	0	0	0
M2	1	1	1	1	1	0	0	0	0	0	0	0	0	0	0

Figure 3.7: Waveform markers

The first marker (M1) is configured to indicate the beginning of the I and Q waveforms at which a trigger pulse will be generated. That is, in order to activate M1, the first entry of the first row is set to 1. When M1 is on, the trigger pulse is automatically sent to the **EVENT1** output port of the VSG.

On the other hand, the second marker (M2) shows where the pulse is ON in order to make the VSG blank the RF output during OFF samples of the pulse. The PULSE/RF blanking operation, which also enables the Automatic Level Control (ALC) hold function, is important to maintain the output power level of the RF signal. If PULSE/RF blanking and ALC are OFF, VSG may fail to maintain the correct output level. (The effect of PULSE/RF blanking and ALC hold functions on the power levels is shown in Appendix C.1.) Therefore, the entries of M2 corresponding to the pulse width of the signal are set to 1 for PULSE/RF blanking (Figure 3.7). In addition, the PULSE/RF blanking function is assigned to M2 by means of an SCPI command (See Table 3.1). After downloading the markers to the VSG as it will be described in Section 3.2.1.3, it should be checked that the annunciator *ENVLP* representing the RF blanking appears on the screen of VSG.

3.2.1.3 Waveform Download Assistant

Agilent Waveform Download Assistant Toolkit provides a set of MATLAB functions required to download the complex IQ data array into the VSG, such as *agt_newconnection*, *agt_query*, *agt_waveformload*, *agt_sendcommand*. The steps of the downloading process are as follows:

1. **Open a new connection session with the VSG over the LAN interface:**

   The LAN connection between the VSG and the computer is established using the *agt_newconnection( )* function, which takes the IP address of the VSG as the input.

   Using *agt_query( )* function, the IEEE SCPI query command **idn?* can be sent to the VSG in order to verify the connection. If the connection fails, an error message is displayed.

2. **Download the IQ waveform to the VSG:**

   Once the connection is established, the IQ waveform, sampling rate and the marker waveforms can be downloaded to the VSG using *agt_waveformload( )* function. If the download fails, an error message is displayed. If the download is successful, the annunciators *ARB* and *IQ* appear on the screen of VSG.

3. **Configure VSG:**

   Each of the configuration settings, such as center frequency, output power level, marker functions, etc. can be defined as an SCPI string (Table 3.1). These SCPI strings are sent to the VSG as the input argument of *agt_sendcommand( )* function.

Table 3.1: SCPI commands for VSG

SCPI command	**Meaning**
‘SOURce:FREQuency 10GHz’	Sets the center frequency to 10 GHz
‘POWer 10dBm’	Sets the output power 10 dBm
‘OUTPut:MODulation:STATe ON’	Turns the modulator ON (MOD ON)
‘OUTPut:STATe ON’	Turns the RF output power ON (RF ON)
‘SOURce:RADio:ARB:MDEStination:PULSe M2’	Assings the RF blanking function to M2

3.2.1.4 Vector Signal Generator

Once the user defined I and Q waveforms are downloaded to the VSG, they are written on the waveform memory and repeated continuously until a new waveform is downloaded.

Next, the digital I and Q waveforms are sent to the internal baseband generator block of the VSG (in Dual Arbitrary Waveform Generator mode). In this block, the digital-to-analog conversion of the I and Q waveforms are performed using the sample clock information, which is also downloaded from the computer together with the I and Q waveforms.

Then, in order to upconvert the signal to the desired carrier frequency (in this study, 10 GHz [3]), analog baseband I and Q signals are fed into the IF ports of the I/Q modulator of the VSG [46] (Figure 3.4). The output of the I/Q modulator is at the desired center frequency and power level.

3.2.2 High Power Amplifier

The received power is directly proportional to the transmitted power. In order to improve the received power and the SNR, the transmit power should be increased.

In order to increase the transmit power further, a high power amplifier is required after VSG (Figure 3.1 and Figure 3.2). In this study, *Agilent HP8348A Microwave Amplifier*, whose P_{out} vs. P_{in} graph at the frequency of interest, i.e., at 10 GHz, is given in Figure 3.8, is utilized. As it can be seen from the figure, the amplifier provides about 30 dB linear gain at 10 GHz.

It should be noted that the RF input to the amplifier should not exceed the maximum continuous power +22 dBm [39]. Detailed specifications of the high power amplifier are provided in [37] and [39].

---

[3] The carrier frequency is selected considering the frequency range of the antennas at hand.

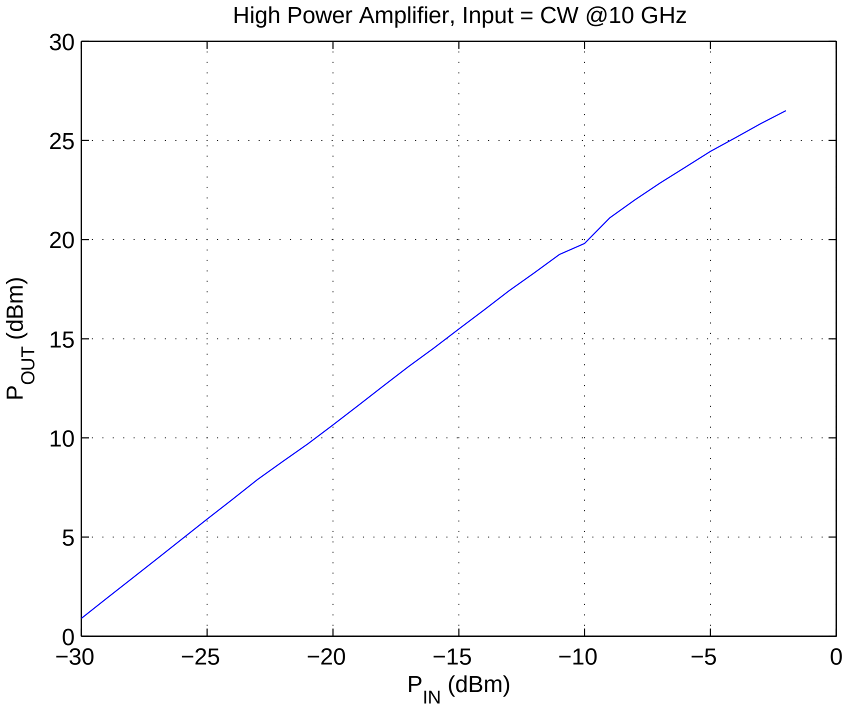

Figure 3.8: P_{out} vs. P_{in} graph of HP8348A @ 10 GHz CW input

3.3 Receiver

As explained before, two alternative receivers have been used in this study. In this section, the operation principle of these receivers is explained (Figure 3.9).

3.3.1 Low Noise Amplifier

In order to amplify the weak return signal received by the antenna, an amplifier is required at the front-end of the receiver. However, any component inserted in the system introduces some noise on the received signal, which effects the signal-to-noise ratio (SNR). The SNR degradation caused by components in an RF system is measured by noise factor (F) and noise

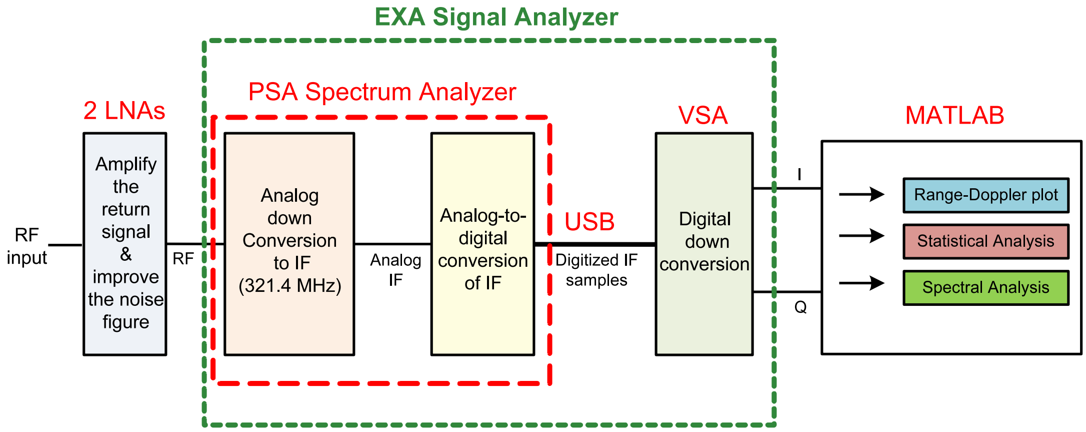

Figure 3.9: Operation principle of the receiver

figure (NF) of the system:

$$F = \frac{SNR_{in}}{SNR_{out}} \tag{3.6a}$$

$$NF(dB) = 10\log_{10}(F) = SNR_{in,dB} - SNR_{out,dB} \tag{3.6b}$$

For a cascaded N-stage system, the overall noise factor can be found from the Friis' formula

$$F_{overall} = F_1 + \frac{F_2 - 1}{G_1} + \frac{F_3 - 1}{G_1 G_2} + \cdots + \frac{F_N - 1}{G_1 G_2 \cdots G_{N-1}}, \tag{3.7}$$

where F_i and G_i denote the noise factor and linear gain of the i^{th} stage of the system, respectively. According to (3.7), the overall noise factor of the system mostly depends on the noise factor of the first stage, since the contribution of the subsequent stages to the noise factor is reduced by the gain of the previous stages. Hence the amplifier, which will be added as the first stage of the receiver, should have a low noise figure.

In this system, *AML218L1502 Low Noise Amplifier (LNA)* with a noise figure of maximum 3 dB is utilized as the first stage of the receiver. It also provides about 18 dB gain at 10 GHz [40]. Using such an LNA with quite high gain, the effect of high noise figure of the PSA spectrum analyzer, which is about 25 dB, is alleviated. (For the second receiver option, the noise figure of the EXA signal analyzer is about 2 dB worse than that of the PSA spectrum analyzer in the first option.) From the Friis' formula for the current receiver system

$$F_{overall} = F_{LNA} + \frac{F_{PSA/EXA} - 1}{G_{LNA}}, \tag{3.8}$$

the overall noise figures of two receiver options are found to be 8.446 dB and 9.966 dB. The overall gain of the receiver unit is 18 dB. (Figure 3.10)

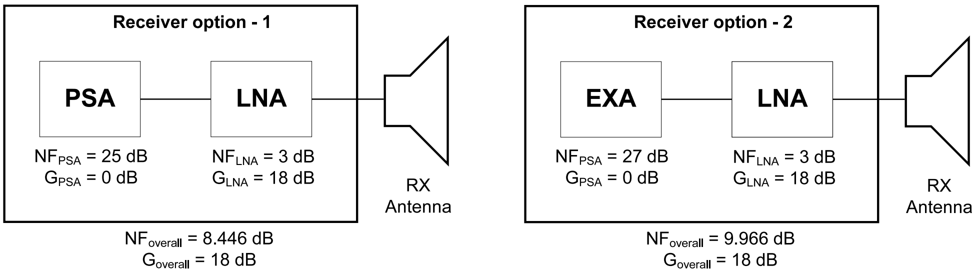

Figure 3.10: Overall noise figure and gain of the receiver with 1 LNA

In order to improve the noise figure of the receiver further, two *AML218L1502* LNAs are cascaded (Figure 3.1 and Figure 3.2):

$$F_{overall} = F_{LNA1} + \frac{F_{LNA2} - 1}{G_{LNA1}} + \frac{F_{PSA/EXA} - 1}{G_{LNA1} G_{LNA2}}. \tag{3.9}$$

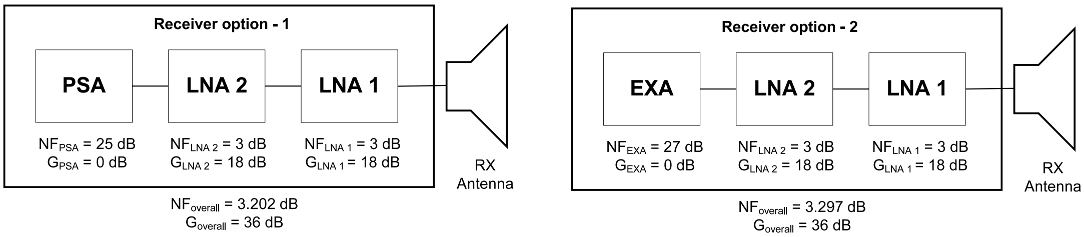

Figure 3.11: Overall noise figure and gain of the receiver with 2 LNAs

Then, the resulting noise figures of two receiver options are 3.202 dB and 3.297dB, while the overall gain of the receiver unit is 36 dB. (Figure 3.11)

3.3.2 Receiver Option 1

The first receiver option is composed of PSA Spectrum Analyzer and Vector Signal Analyzer software (Figure 3.1).

3.3.2.1 PSA Spectrum Analyzer

In this option, *Agilent E4446A Performance Spectrum Analysis (PSA) Spectrum Analyzer* forms the hardware of the receiver unit. It can be classified as a superheterodyne receiver. The spectrum analyzer first downconverts the received signal into IF frequency and then digitizes it (Figure 3.9). Then, it performs all processing in digital domain.

In order to perform the radar signal analyses explained in Section 2, the receiver should provide the time domain I and Q data. Besides frequency domain analyses, the spectrum analyzer can perform time domain analyses in its *Basic Mode*. In this mode, the spectrum analyzer is capable of downconversion of digital IF and then storing maximum 10^6 complex baseband time samples with a time resolution of 66.7 nsec (at IF BW = 10 MHz [4]) in its memory [42]. That is, the corresponding maximum total time record length is about 66.7 msec. In Basic Mode, it is possible to download 10^6 complex baseband samples directly from the spectrum analyzer's memory and save it into a '.mat' file on the computer (in this study, via USB interface).

However, there is a limitation on the center frequency, for which the time domain analyses can be performed by the spectrum analyzer. The maximum frequency allowed in Basic Mode is 3 GHz. For the center frequencies higher than *3 GHz*, the Vector Signal Analyzer software is required for time domain analysis. Hence, the digitized IF signal is sent to the Vector Signal Analyzer, where the digital downconversion is performed.

3.3.2.2 Vector Signal Analyzer Software

Agilent 89600 Vector Signal Analyzer (VSA) is a software tool which works with various hardware measurement platforms and processes the data in time, frequency and modulation domains [43]. In this study, VSA 89601A is used with E4446 PSA spectrum analyzer, which

---

[4] The IF BW is chosen according to the bandwidth of the signal, which is generally 10 MHz in this study.

is configured as its analog-to-digital converter module. VSA takes the digitized IF samples from the spectrum analyzer over the USB interface in between.

In this experimental system, the main operation of the VSA is the downconversion of digital IF signal into the baseband. The detailed block diagram and working principle of the vector signal analyzer can be seen in [37]. Basically, after downconversion into baseband, the data are recorded into a sample memory. Then, all of the frequency, time and modulation domain analyses are performed on these samples.

In this study, the time domain I and Q data provided by the VSA are recorded in a '.mat' file to process in MATLAB. In order to make accurate measurements, the optimum configuration of the VSA should be done as follows:

The input range: Setting the input range too low introduces distortion in the measurements, while a too high input range yields loss of dynamic range. For instance, the effect of low input range on the measurements is illustrated in Figure C.2. Hence, selecting the optimum input range for the received signal is important in terms of the measurement accuracy.

Time record length: The time record length depends on the frequency span, the frequency points, and the RBW [5] [43]. The total time length can be calculated from

$$\text{Total time record length (sec)} = \frac{\text{Number of frequency points} - 1}{\text{Span}}. \tag{3.10}$$

The total time record length is important in terms of the Doppler resolution as given in 2.11. The higher the total length is, the better the Doppler resolution is. Besides, for the temporal statistics of the return signal, where the behavior of the clutter over time is analyzed, it is better to observe a range cell longer. Hence, the time record length is desired to be as long as possible. Then, the number of frequency points is selected as maximum as possible, where the frequency span is required to be the minimum.

Time sample resolution: The time resolution of the received samples, *XDelta*, is directly related to the range resolution. Hence, the time resolution should be adjusted in VSA in such a way that the range resolution requirement of the system is satisfied.

---

[5] RBW is set to arbitrary at auto coupled mode.

$$\text{XDelta} = \frac{1}{1.28 \cdot \text{Span}} \tag{3.11}$$

As discussed in Section 2.3, both temporal and spatial behavior of clutter statistics strongly depend on the range resolution. Besides, the range resolution is important in target detection. In this experimental study, the range resolution, or equivalently the time resolution, is desired to be sufficiently high. Here, it should be stated that the best time resolution that can be achieved by this set-up, i.e., receiver option 1, is about 97 nsec, since the maximum frequency span of the VSA is 8 MHz.

It can be easily observed from (3.10) and (3.11) that the selection of the frequency span is critical due to the trade-off between the time resolution and the total time record length. This trade-off stems from the limited memory reserved for the frequency points per span. The maximum number of frequency points allowed per span, i.e., the maximum frequency display points, is 524288 [6], while the corresponding total time points can be equal to or less than this number (if zero padding is required before the FFT process). Due to the fixed number of total time points, the total time record length decreases if the time resolution is improved further, or vice versa. Hence, an optimization is required considering the system requirements.

For instance, consider a P4-coded pulse whose signal parameters are as follows: PW = 4 usec, PRI = 100 usec, number of chips = 40. Then, the chip width of the pulse is 100 nsec, which corresponds to a range resolution of 15 m. For simplicity, the time resolution of the VSA is chosen to be 100 nsec, so that each received sample corresponds to a chip. Then, from (3.11), the required frequency span is 7.8125 MHz. The corresponding maximum total time length, calculated from (3.10) is only 52.4 msec.

In order to increase the total time length, it can be suggested that successive time recordings can be appended. However, it has been observed that the phase of the signal differs significantly from one recording to another, which may result in loss of phase coherency. Therefore, this approach cannot be utilized for spectral analysis, which is directly influenced by the phase of the signal. On the other hand, for statistical analysis of clutter in space, the total time length of the measurement is not significant. Hence, there is no need to append successive files in order to increase the total length. However, it can be proposed that for statistical analysis, in

---

[6] Note that, the maximum number of sample points is limited further by VSA since the waveform memory of 1 Gsamples, available in Basic Mode of spectrum analyzer, cannot be utilized.

which the phase coherency is not essential and a long time dwell is required, the method of appending successive recordings can be used.

As a consequence, due to the limitations of the VSA and PSA, the system requirements should be well defined and the optimization of the system parameters should be done accordingly.

3.3.3 Receiver Option 2

The time record length of the first receiver option is quite short (52.4 msec at 15 m range resolution). Hence, in order to improve the time record length further, other alternatives have been sought (details are given in [37]). Among them, it has been possible to realize only the following option due to time and resource shortage: *Agilent N9010A EXA Signal Analyzer* itself is utilized as the receiver of the system (Figure 3.2).

3.3.3.1 EXA Signal Analyzer

As it can be seen from Figure 3.9, the EXA performs analog downconversion, IF digitization and digital downconversion operations. The specifications of EXA signal analyzer, which are of interest for this study, are almost the same as the PSA spectrum analyzer, except the following two:

1. EXA signal analyzer is able to make time domain measurements up to 13.6 GHz, where PSA spectrum analyzer allows up to 3 GHz. By this means, it becomes possible to omit VSA at the frequency of interest, i.e., at 10 GHz, and use EXA itself in *I/Q Analyzer Mode* for digital downconversion. Then, the limit on the number of samples brought by VSA can be eliminated and the whole waveform memory can be used for time domain IQ waveform analysis.

2. EXA signal analyzer is able to record maximum 4.10^6 samples with a time resolution of 66.7 nsec (at 10 MHz IF BW) [45], i.e., 4 times that of PSA spectrum analyzer can do in its Basic Mode. As a result, the total length will be 266.67 msec at 10 m range resolution.

The time record length is still on the order of msec, however, it is improved together with the range resolution with respect to the first receiver option. The maximum time record lengths and the corresponding Doppler resolutions achieved by the two receiver options at the best available range resolutions are tabulated in Table 3.2.

Table 3.2: Time record lengths and Doppler resolutions for the receiver options

	Receiver Option 1 **PSA + VSA**	**Receiver Option 2** **EXA**
Best range resolution	15 m	10 m
Total time record length	52.4 msec	266 msec
Doppler resolution	19 Hz	3.8 Hz

3.4 Antennas

In this study, separate antennas are utilized for the transmitter and the receiver. As it can be seen from Figure 3.3, the antennas are placed next to each other while pointing in the same direction. The positions of the antennas are fixed during measurements.

First, spiral antennas were used as the transmitting and receiving antenna. However, since their beamwidths are very large and they have low gains, they were replaced by double ridged horn antennas *GAH-1042* and *DRH-412*. The gains and the radiation patterns of these antennas at the frequency of interest were measured in the anechoic chamber. The details of the measurements are given in [37] and the results are presented in Table 3.3 and Figure 3.12.

Table 3.3: Gain of the antennas

	Antenna 1 **(GAH-1042)**	**Antenna 2** **(DRH-412)**
@ 9GHz	15.5257 dBi [7]	11.1457 dBi
@ 10GHz	15.3757 dBi	11.8457 dBi

---

[7] *decibels relative to isotropic* - gain of an antenna relative to an isotropic antenna, which uniformly distributes energy in all directions

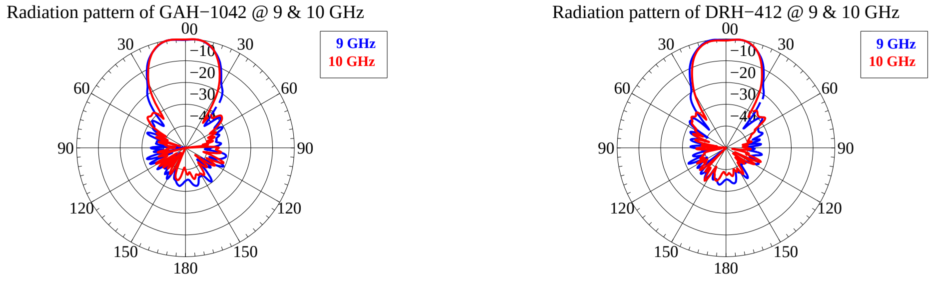

(a)

(b)

Figure 3.12: Measured radiation patterns of the antennas (E-plane)

As it can be seen from the radiation patterns, the 3dB-beamwidths of both antennas in the azimuth plane are around 30°. The beamwidth of the antenna is of great importance to the spatial calibration discussed in Section 2.3.1.1. It also determines the angular resolution as a distance at range R, which is calculated from (3.12), θ being the antenna beamwidth (Figure 3.13). For example, two targets at a range of 2.5 km should be separated by a distance of at least 1.3 km in order to be resolved in this system.

$$S_{res} = 2R \sin \frac{\theta}{2} \tag{3.12}$$

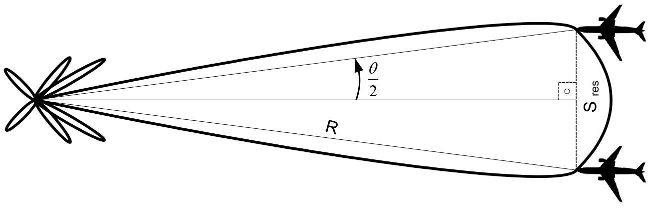

Figure 3.13: Angular resolution

Besides, both of the antennas are vertically linear polarized. Furthermore, these antennas can be used interchangeably for the transmitter and receiver units owing to the antenna reciprocity.

If a single antenna were used for both transmitter and receiver, a circulator (duplexer) would be required. In this case, the receiver would be *off* during transmission. After the transmission is completed, the antenna would be switched to the receiver by means of the circulator. However, in this study, since separate antennas are used for transmitting and receiving, and the reception is triggered at the beginning of the transmit signal (3.2.1.2), reception continues during the transmission period. Then, although the antennas are placed as far as possible from each other for isolation, the coupling of the transmit signal directly into the receiver antenna cannot be avoided. Hence, the transmit signal, which is not reflected from the scatterers but directly coupled into the receiver, should be removed from the received signal. This operation can be performed during data processing which will be explained in Section 3.5.

However, this isolation problem may yield much critical problems, such as RF input port of the receiver being subjected to a high RF power level. This may result in less sensitivity of the analog-to-digital converter (ADC) circuitry to weaker signals or even damage to the receiver. In this case, it is always useful to measure the RF level at the receiver side and make sure that the received power does not exceed the maximum input level of the receiver.

Besides, it should be noted that the LNAs may not operate anymore in the linear region during the pulse widths because of the high RF power due to the coupled transmit signal. Operating beyond their compression point, gain of the LNAs decreases. Consequently, the desired noise figure cannot be achieved. By removing the samples corresponding to the coupled transmit signal from the received signal, this problem can be eliminated. During the *off* times of the transmitter, the LNAs are expected to operate in their linear region again.

3.5 Processing the Received I and Q vs. Time Data

The last block of the receiver is the receiver processing block, which is implemented in MATLAB. The processor gets the received complex IQ time data saved into a '.mat' file by VSA or EXA, in which all the settings are also included. The processor also knows the transmitted signal and its parameters.

Then, the flow of the process is as follows (Figure 3.14):

1. First, as described in Section 3.4, the samples of transmitting signal, which are directly coupled into the receiver due to isolation problems, should be removed as if reception is off during transmission. Hence, the received IQ time samples corresponding to the first pulse width are removed from each pulse repetition interval. Considering the delay of the trigger pulse and the recovery time of LNAs to get off the compression region, a

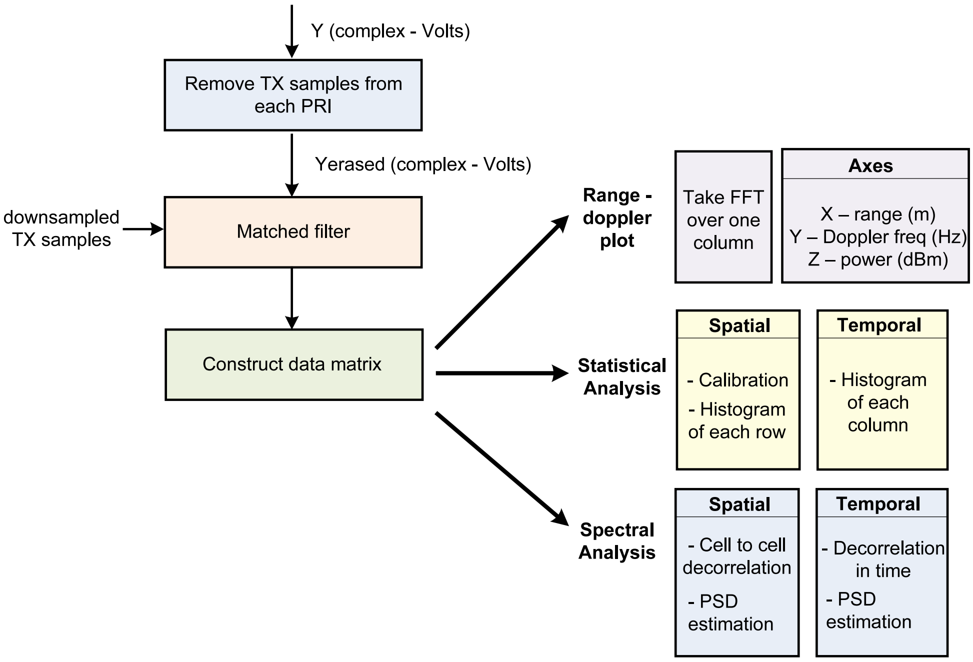

Figure 3.14: Flow of the receiver processing

few extra samples may be removed.

Here, it should be noted that, although separate antennas are used for transmission and reception in this system, by removing the first samples received during transmission, the bistatic radar system turns into a monostatic radar, in which the receiver waits for the whole transmit pulse to leave the antenna and the range that corresponds to the pulse width and recovery time is said to be eclipsed. Hence, the system used in this study is also exposed to that blind range of monostatic radars. This blind range, R_{min}, can be expressed as follows:

$$R_{min} = \frac{c \cdot (\text{pulse width} + \text{recovery time})}{2}, \tag{3.13}$$

Although an echo from a range closer than R_{min} cannot be received completely due to the off time of the receiver, less samples can still be received. In such cases, since less samples enters the matched filter, the peaks at the output of the matched filter may not be so clear. This blind zone can be excluded by removing another pulse width from the received signal.

2. Next, in order to maximize the signal-to-noise ratio, the matched filtering operation

is performed. The received IQ time samples are convolved by the conjugate of time reversed IQ data samples of the transmitting signal. Here, it is important to note that a correction is required due to the different transmitting and receiving sampling rates. The transmitting signal is generated by a sample clock of maximum 100 MHz, where the maximum sampling rate of the receiver is about 10 MHz. Hence, the IQ samples of the transmitting signal is downsampled before matched filtering.

3. After matched filtering, an MxN data matrix, which is explained in Section 2.1 is constructed. Each row of this data matrix is composed of samples from one pulse repetition interval and each column represents the samples from one range cell. For a coded pulse, data matrix is constructed so that each chip corresponds to a range cell. Once the data matrix is constructed, various digital signal processing operations can be performed along its dimensions. In this study, the range-Doppler processing of the received signal is performed; spatial and temporal spectrum of the received signal are observed; spatial and temporal statistical distributions are determined.

   Range-Doppler plot: In order to get the range-Doppler plot, FFT is taken in the columns of data matrix by means of the *fft()* function of MATLAB. Since the *fft()* function of MATLAB does not perform any normalization, the output should be divided by the FFT size.

   By taking FFT columnwise, it can be concluded that there is a target in a particular range cell if there is a return from that range cell in all pulse repetition intervals. Besides, if there is a target moving in a particular range, the non-zero Doppler shift due to its motion can be observed in that range cell.

   The axes of the range-Doppler plot are arranged as follows:

   - X-axis (Range axis): Since the time resolution (XDelta) is known, the fast-time samples can be written in terms of seconds and then converted into the corresponding ranges. Here, it is important to note that if the blind zone is excluded from the analysis as explained above, the range axis should be arranged accordingly.
   - Y-axis (Doppler range axis): The slow-time samples can be transformed into the Doppler frequency. Doppler axis can be chosen to be between (-1/2PRI, 1/2PRI) or (0, 1/PRI) if it is known that all the targets are approaching; (1/PRI, 0) if it is

known that all the targets are moving away.

- Z-axis (Amplitude): In VSA and EXA, the received IQ time data samples are saved into the files in terms of *Volts*. The amplitude is converted into power in *dBm* by the following formula:

$$\begin{aligned}
\text{Power (Watts)} &= \frac{(\text{Volts}/\sqrt{2})^2}{\text{R}(\Omega)} * \text{duty ratio} && \text{(3.14a)}\\
&= \frac{(\text{Volts}_{\text{rms}})^2}{50(\Omega)} * \frac{\text{PW}}{\text{PRI}} && \text{(3.14b)}\\
\text{Power (dBm)} &= 10\log_{10}(\text{Power (Watts)}) + 30 && \text{(3.14c)}
\end{aligned}$$

Spectral analysis: By means of various methods, the power spectral density estimates of the slow-time and the fast-time samples are obtained (Section 2.2).

Statistical analysis: The histogram of the slow-time and the fast time samples are plotted and various goodness-of-fit test are applied on both dimensions in order to extract the temporal and spatial statistical behavior of the return signal (Section 2.3).

3.6 Verification of the System Using Generic Signals

In order to verify the system, the signal generator and the spectrum analyzer are directly connected to each other, without using antennas. A generic signal is constructed and after the received signal is processed, the results are evaluated.

3.6.1 Ability of Doppler Shift Detection

As explained in Section 3.1, if the oscillators of the signal generator and the spectrum analyzer do not use the same 10 MHz reference, the frequency reading at the spectrum analyzer will be incorrect. This error can be interpreted as a Doppler shift in the carrier frequency and it is expected to be observed on the range-Doppler plot after the signal processing.

Equivalently, the carrier frequency can be set to a value slightly different than the intended operating frequency. For instance, the VSG center frequency is set to 10 GHz + 2000 Hz and

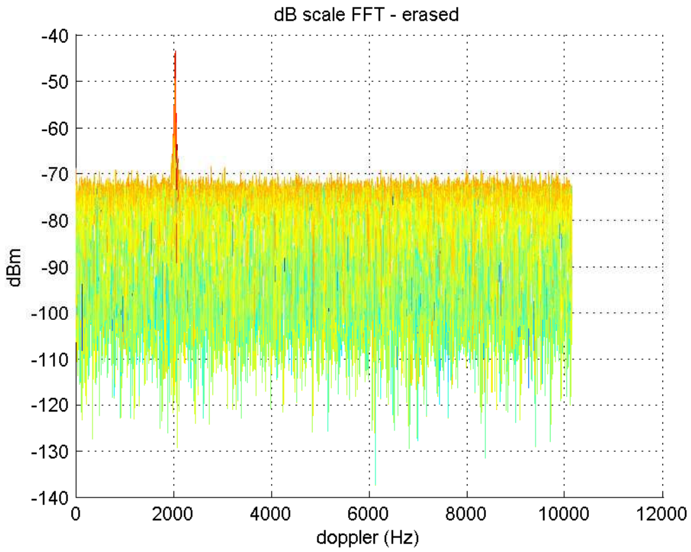

Figure 3.15: Doppler shift

the spectrum analyzer center frequency is adjusted to 10 GHz as usual. When the received signal is processed, the Doppler shift of 2000 Hz can be seen on the range-Doppler plot, as expected (Figure 3.15).

3.6.2 Ability of Finding the Target Location

In order to verify the ability of target range detection, a transmit pulse with an inherent delay is generated. Since the trigger is taken from the first sample of the whole PRI, the pulse seems to be received after some delay. For example, a pulse with 40-chip-P4 code, 4 usec PW and 100 usec PRI is sent as in Figure 3.16(a) with a delay of 40 usec, which corresponds to a range of 6000 m. The result is shown in Figure 3.16(b), where it can be seen that there is indeed a target at 6000 m.

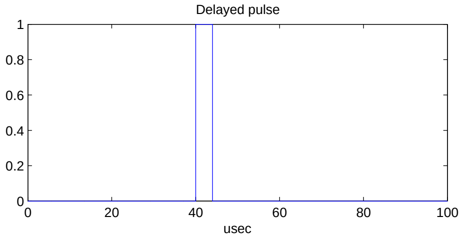

(a)

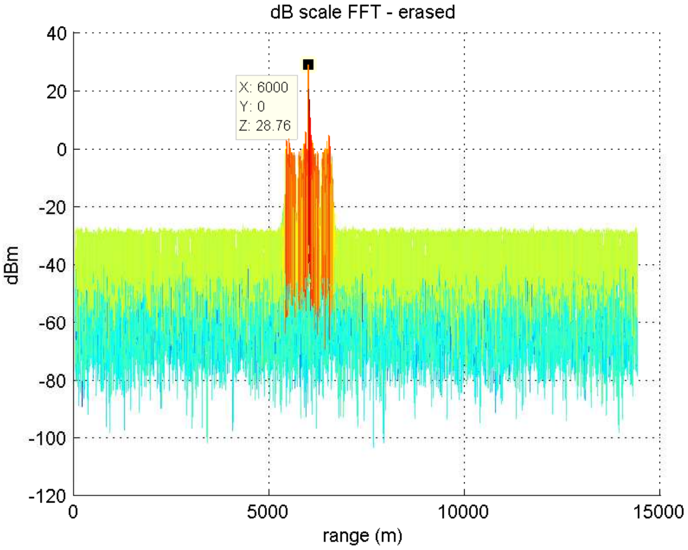

(b)

Figure 3.16: (a) Delayed transmit pulse, (b) Target detected at 6000 m

3.7 Graphical User Interface

The graphical user interface (GUI) is developed in MATLAB. It allows the user to enter the transmitting signal parameters, such as PW, PRI, number of chips and pulse code, in order to create and save a new transmitting signal. The user may also select a predefined signal to transmit. The IQ waveform is downloaded to the VSG by means of the SEND command. Also, the carrier frequency and the output power can be adjusted via the GUI. It lets the user browse the received signal files saved by VSA and EXA and select the file to be analyzed. Statistical and spectral analyses on the received signal can be controlled by means of the GUI. A screenshot of the GUI can be seen in Figure 3.17.

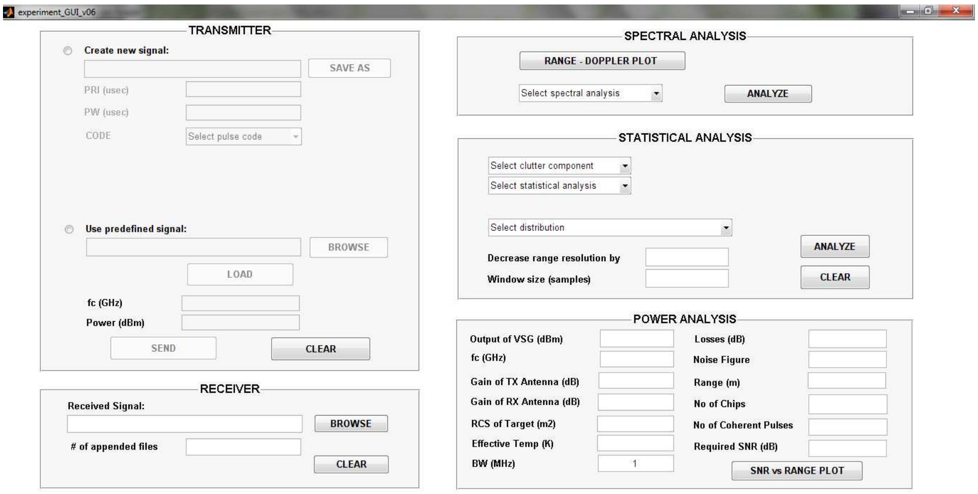

BW (MHz) 1

Figure 3.17: Graphical user interface

3.8 Comparison of the System with the Previous Studies

In the literature, many studies conducted on experimental radar clutter data can be found. Among them, studies performed by Billingsley at MIT Lincoln Laboratory (MIT-LL) are quite comprehensive [7], [12], [14]. Many measurements were taken at different sites, and the details of the measurement systems and the sites were published as technical reports. During the establishment of the experimental data acquisition system for this study, these technical reports have been frequently referred. In this section, the data acquisition system used in this study is compared to the systems used by MIT-LL.

MIT-LL performed clutter measurements with two different radars, namely the Phase One and L-Band Clutter Experiment (LCE), at different frequency ranges. Also, different systems and parameters were used for spatial and temporal analyses. For instance, short time dwell measurements were used for spatial analyses, while the temporal analyses were based on long time dwell measurements. In addition, the antenna beam was rotated in each PRI for cell-to-cell clutter characterization, while the measurements for temporal analyses were taken with a stationary beam antenna.

In Table 3.4 and Table 3.5, the main system parameters are compared for spatial and temporal clutter analyses, respectively. For comparison, a set of most commonly used system parameters is used.

Table 3.4: Comparison of MIT-LL Phase One radar clutter measurement system and the experimental data-acquisition system used in this study for spatial analysis

System parameter	**MIT-LL Phase One [12]**	**System-1 (PSA + VSA)**	**System-2 (EXA)**
Frequency	X-Band (9.1 GHz)	X-Band (10 GHz)	X-Band (10 GHz)
Antenna	Rotating	Stationary	Stationary
Polarization	VV or HH	VV	VV
3-dB beamwidths	1°az. & 3°el.	30°az.	30°az.
Pulse width	100 nsec	4 usec	5.32 usec
Number of chips	1 (uncoded pulse)	40 (P4 coded pulse)	40 (P4 coded pulse)
Chip width	100 nsec	100 nsec	133 nsec
Bandwidth	10 MHz	10 MHz	7.5 MHz
Range resolution	15 m	15 m	20 m
RX sampling rate	10 MHz in range	10 MHz	15 MHz
Samples/chip	1	1	2
Range cell spacing	15 m	15 m	10 m
TX power	50 kW peak (34 dBm average)	7.5 dBm average	7.5 dBm average
PRI	2 msec	100 usec	133 usec
Calibration wrt. cell area	YES	YES	YES
Calibration wrt. distance	YES (STC [8])	YES	YES

---

[8] Sensitivity time control

Table 3.5: Comparison of MIT-LL radar clutter measurement systems and the experimental data-acquisition system used in this study for temporal analysis

System parameter	**MIT-LL Phase One [14]**	**MIT-LL LCE [14]**	**System - 1 (PSA + VSA)**	**System - 2 (EXA)**
Frequency	X-Band (9.1 GHz)	L-Band (1.23 GHz)	X-Band (10 GHz)	X-Band (10 GHz)
Antenna	Stationary	Stationary	Stationary	Stationary
Polarization	VV or HH	VV or HH	VV	VV
3-dB beamwidths	1°az. & 3°el.	6°az. & 3°el.	30°az.	30°az.
Pulse width	1 usec	1 usec	4 usec	5.32 usec
Number of chips	1 (uncoded pulse)	1 (uncoded pulse)	40 (P4 coded pulse)	40 (P4 coded pulse)
Chip width	1 usec	1 usec	100 nsec	133 nsec
Bandwidth	1 MHz	1 MHz	10 MHz	7.5 MHz
Range resolution	150 m	150 m	15 m	20 m
RX sampling rate	1 MHz	2 MHz	10 MHz	15 MHz
Samples/chip	1	2	1	2
Range cell spacing	150 m	75 m	15 m	10 m
PRI	2 msec	2 msec	100 usec	133 usec
Number of pulses/record	30720	30720	524	2000
Time record length	61.44 sec	61.44 sec	52.4 msec	266 msec
Doppler resolution	0.016 Hz	0.016 Hz	19.08 Hz	3.8 Hz
TX power	50 kW peak (44 dBm average)	8 kW peak (36 dBm average)	7.5 dBm average	7.5 dBm average

CHAPTER 4

ANALYSIS OF THE MEASURED RADAR CLUTTER

In this study, the experimental radar system, whose principle of operation, specifications and verification are discussed in Chapter 3, is used to measure radar clutter. The measurements are carried out on the roof of the METU Electrical and Electronics Engineering Department's Building D.

Two different terrains are illuminated with the same transmit signal and the measurements are taken on the same day with the same system shown in Figure 3.2, i.e., the option with EXA Signal Analyzer and 2 LNAs. The system parameters used for clutter measurements can be summarized as in Table 4.1.[1]

After the I/Q data samples are recorded by EXA Signal Analyzer, the steps described in Section 3.5 are applied.

In this chapter, the results of the analyses performed on the experimental radar clutter data are presented in detail. The results are interpreted in the light of the characteristics of the illuminated regions. The photos taken on the day of the measurement together with the top views obtained from the Google Earth application are made use of while making comments on the results.

---

[1] A comparison of the system parameters used during measurements and in the previous studies on radar clutter is given in Section 3.8.

Table 4.1: System parameters used during measurements

THE TRANSMITTER	THE RECEIVER
• P4 coded pulse @ 10 GHz • Pulse width = 5.32 usec • Number of chips = 40 • Chip width = 133 nsec • PRI = 133 usec • 7.5 dBm average transmit power	• Sampling rate = 15 MHz (i.e., 2 samples/chip) • Total time record length = 266 msec
Blind zone = ~ 800 m Range resolution = ~ 20 m Range cell spacing (RC)[2] = ~ 10 m Doppler resolution = ~ 3.8 Hz Maximum unambiguous range = ~ 19 km	

---

[2] Two samples are recorded for each resolution cell. Each sample is referred to as a range cell throughout this chapter.

4.1 Terrain - 1

A photo of the first terrain is shown in Figure 4.1.

Figure 4.1: Terrain - 1 on the day of measurements

Before moving to the analyses of the measured data, the boundaries of the illuminated region are first determined. Hence, the red lines indicating the azimuthal beam of the antenna are first drawn on the Google Earth top view as in Appendix D.1. The antenna beamwidth is generally defined as the 3-dB beamwidth. However, the returns are accepted from a larger angle, obviously with less power. In this study, an area shaded by an angle of 40° is marked as the beam of the antenna.

Next, successive paths at certain intervals are drawn in the beam of the antenna. These paths are of length equal to the theoretical maximum unambiguous range, which is about 19 km. Their altitude profiles obtained from the Google Earth application are given in Appendix D.1. These paths are examined in order to extract the altitude characteristics of the illuminated region. For instance, the presence of a hill at about 5 km can be deduced from these profiles.

It is obvious that the frequency of the paths and their placement may affect the results significantly. Hence, the paths are tried to be placed such that they give a reasonable idea about the altitude of the illuminated area.

Then, for each path, the points which may cause shadowing are determined. Here, it should be noted that, the altitude profiles provided by Google Earth do not include the heights of the buildings. Besides, the grazing angle of the radar should be taken into account in determining the shadowed regions. In this case, it is useful to examine the photo of the illuminated region. Hence, considering the altitude profiles, the heights of the buildings and the grazing angle together, the points causing shadowing are marked. For the first observation area, it can be roughly said that the hill at about 5 km is expected to shadow its back to some range according to the grazing angle. Also, it is possible to see peaks beyond 11 km due to the returns from higher hills at these ranges.

4.1.1 Range-Doppler Processing for Terrain - 1

For the first illuminated region, the power vs. range plot is given in Figure 4.2(a). Here, it should be noted that the first 800 m in the power vs. range plot corresponds to the blind zone. The blind zone can be ignored by removing an extra PW from the received time data.[3] For the range plot given in Figure 4.2(b), a total number of 41 chips (i.e., 82 RCs) are removed: 40 chips for the pulse width and 1 chip for the recovery time of the receiver. Hence, the returns from up to 800 m + 20 m = 820 m are excluded and the range axis starts after 820 m.

As it can be seen from Figure 4.2(a) and Figure 4.2(b), there is actually no return beyond 5 km up to a range of 11 km. Also, peaks with reasonable SNRs can be observed beyond this point as expected. However, it is quite hard to distinguish the scatterers at these ranges due to the quite large angular resolution.

On the other hand, the SNRs of the returns from the first 5 km are quite high. For a detailed range analysis, the range plot is zoomed into this crowded region. In this region, there are many point scatterers such as buildings (Figure 4.3(a)). The ranges of some possible scatterers are marked on the top view of the zoomed region as in Figure 4.3(b), where the red lines show the antenna beam and the blind zone is shaded with green lines. When the range plot in

---

[3] Note that, a pulse width has already been removed due to the isolation problems. Now, a second pulse width is removed in order to eliminate the blind zone.

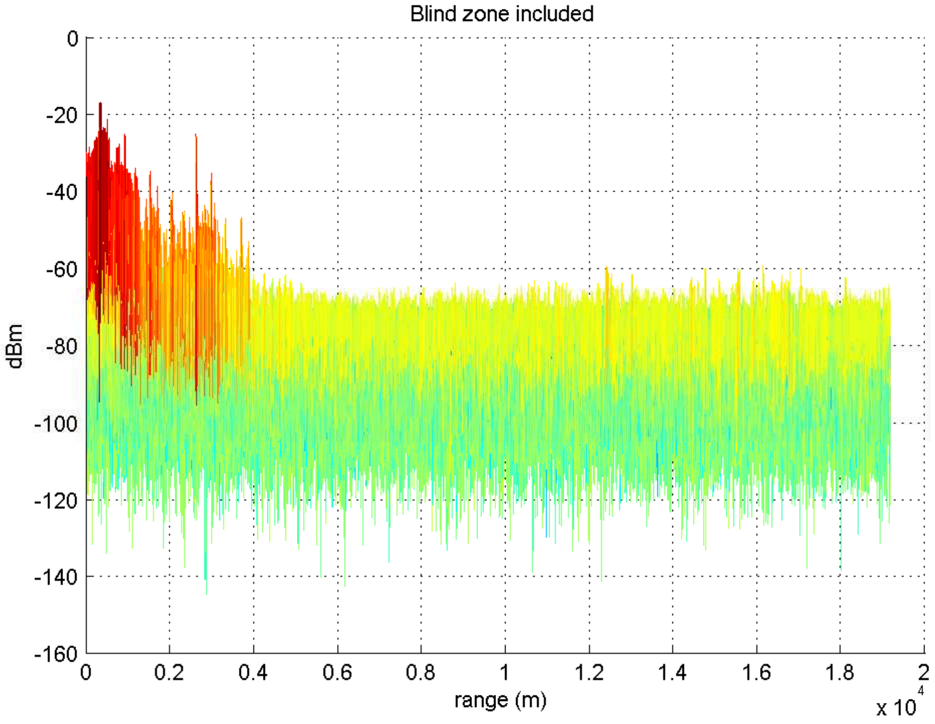

(a) Blind zone included

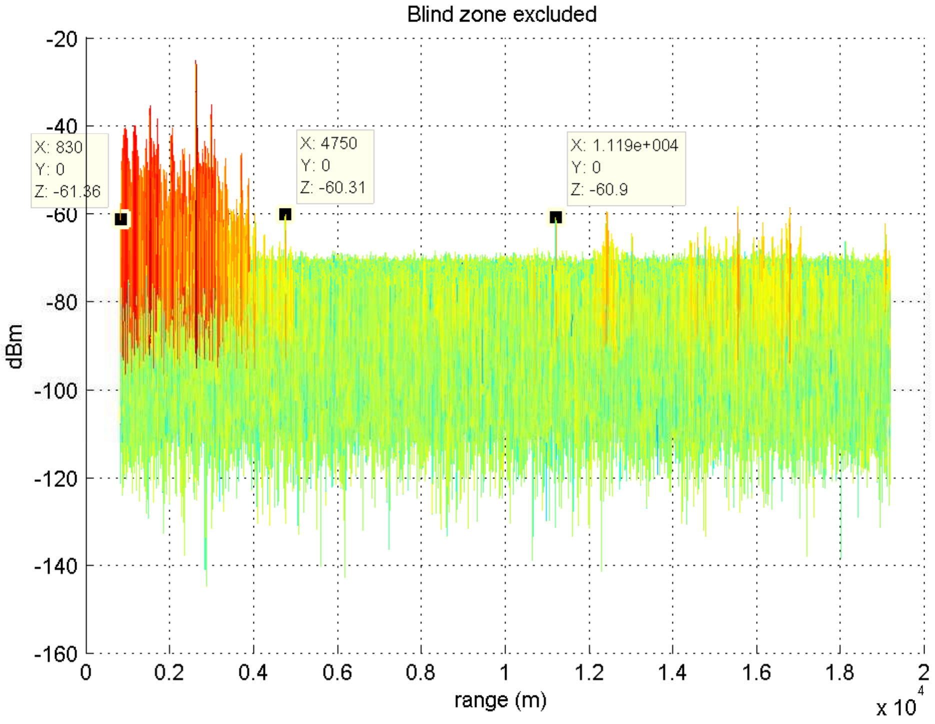

(b) Blind zone excluded

Figure 4.2: Power vs. range plot for Terrain - 1

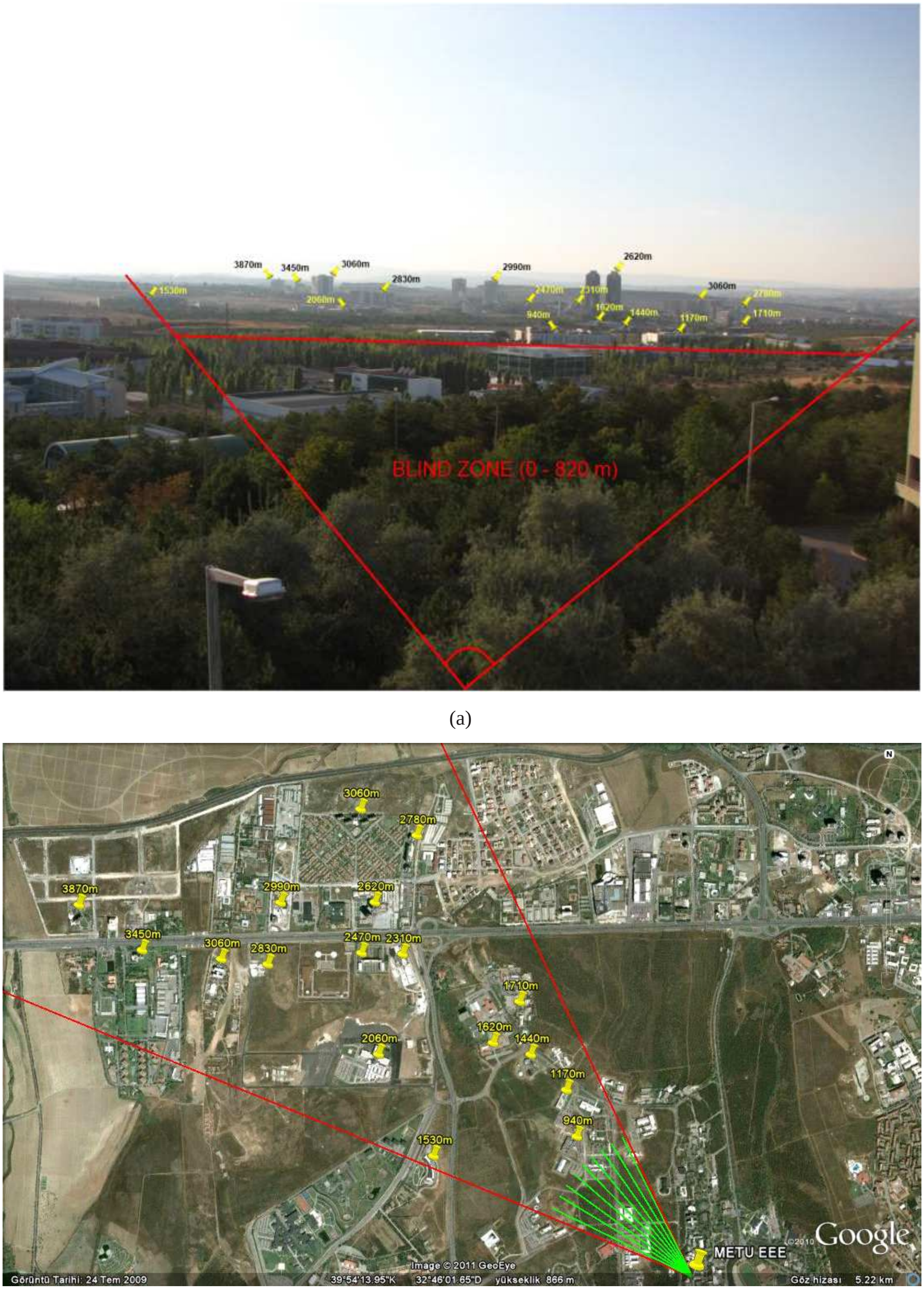
(a)

(b)

Figure 4.3: Ranges of the possible scatterers in Terrain - 1

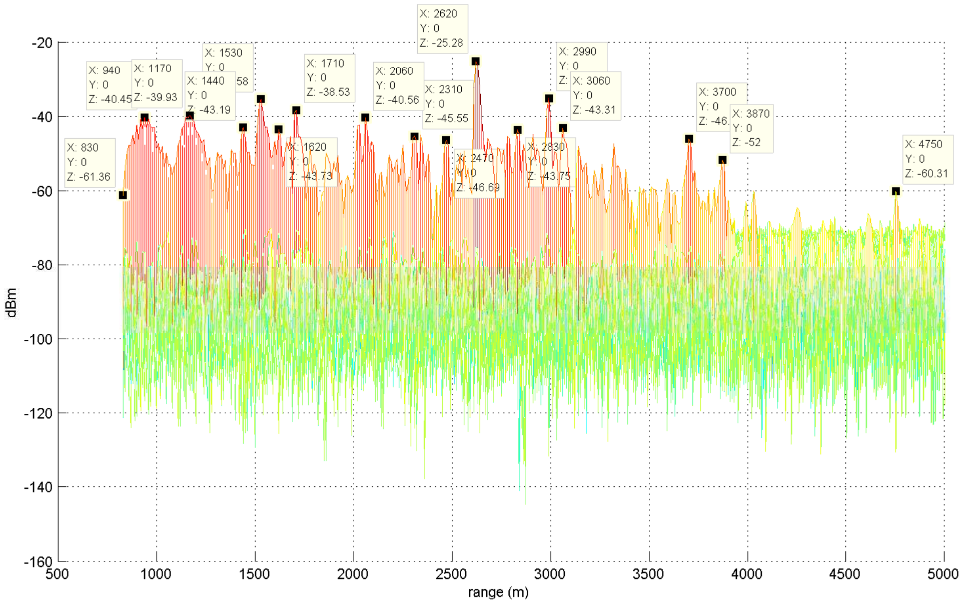

Figure 4.4: Power vs. range plot for Terrain - 1 with blind zone removed (500 m - 5 km)

Figure 4.4 is compared to the photos in Figure 4.3, the ranges of the scatterers mostly seem to be consistent with the range of the peaks in the power vs. range plot.

The range - Doppler plot for the first terrain can be seen in Figure 4.5(a). The Doppler axis is zoomed to the first 50 Hz. Considering the Doppler resolution of the system, which is about 3.8 Hz, no Doppler spread can be observed beyond 820 m. This may be reasonable since the scatterers in this region are mostly buildings and bare hills. Hence, it is not surprising that such stable scatterers do not yield a Doppler spread.

The blind zone is also examined in terms of Doppler spread. Hence, the range - Doppler plot is redrawn with the blind zone included as in Figure 4.5(b). From this plot, a Doppler spread of 15-20 Hz can be immediately seen in the blind region. This may be explained by the fact that the region is mostly crowded with trees and the movement of the leaves may result in a Doppler spread. Besides, the air is still during the measurements. In the presence of wind, the Doppler spread is expected to be greater. Detailed examination is given in the following subsection.

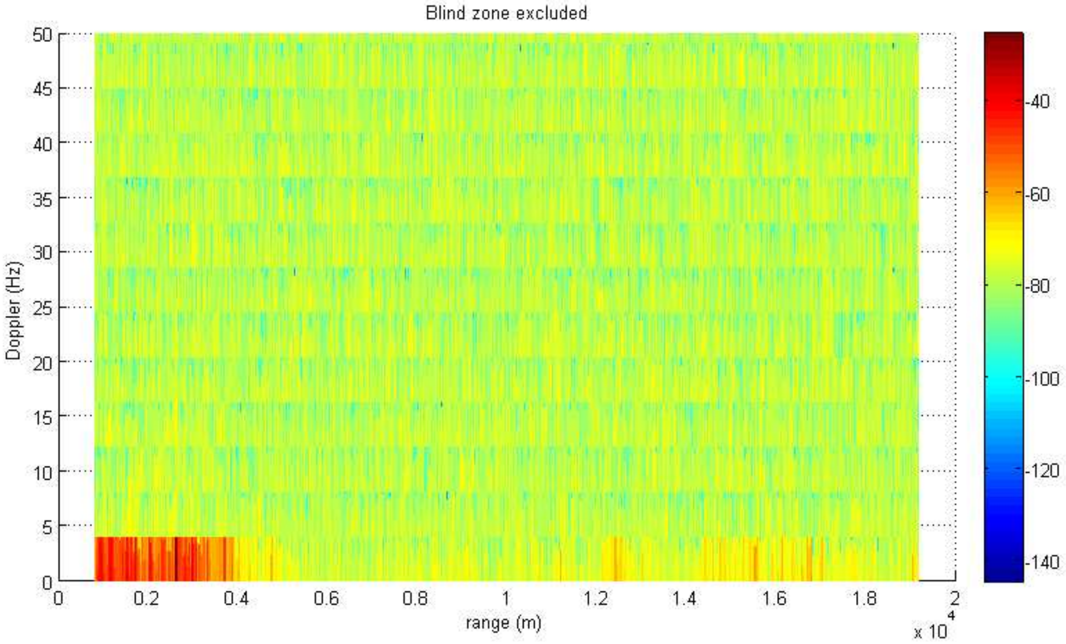

(a) Blind zone excluded

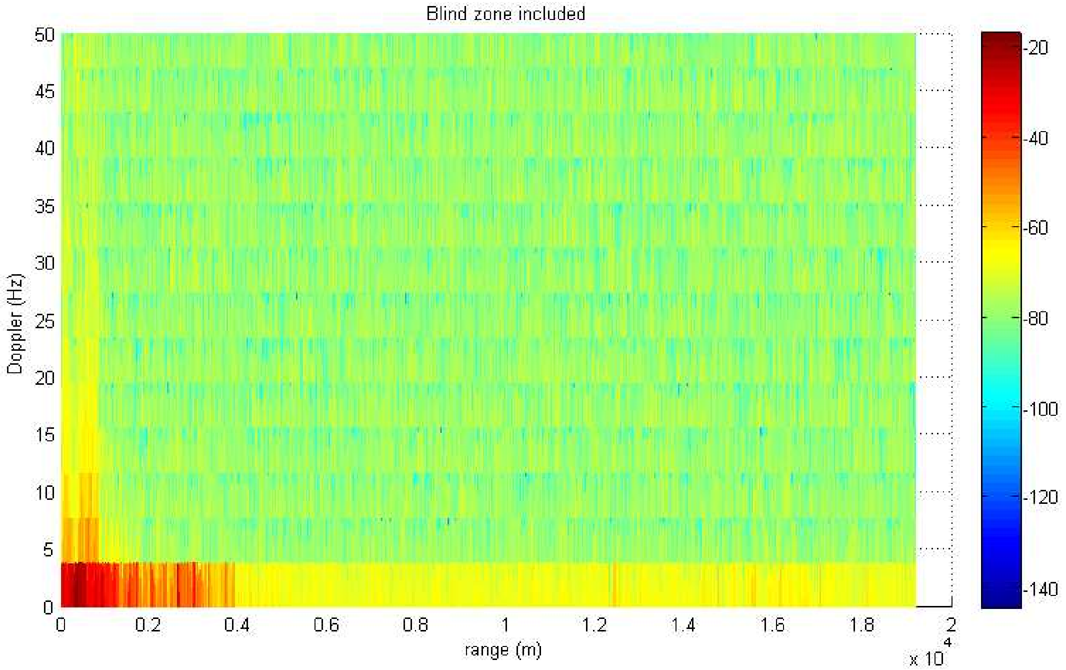

(b) Blind zone included

Figure 4.5: Doppler vs. range plot for Terrain - 1 (0 - 50 Hz)

4.1.2 Spectral Analysis for Terrain - 1

The Doppler axis in the Doppler vs. range plot gives an idea about the spectral characteristics of a range cell. Here, two different range cells marked in Figure 4.6 are examined in detail. The first range cell is filled with trees while the second cell consists of a building.

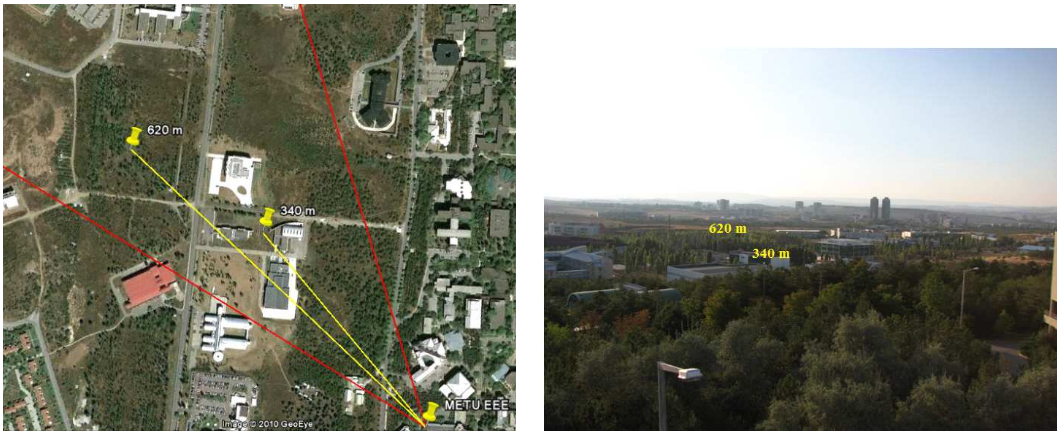

(a) (b)

Figure 4.6: RCs at 340 m and 620 m for detailed spectral analyses (Terrain - 1)

First, consider the range cell with trees at 620 m, for which the I/Q components and the amplitude of the returns from 2000 successive pulses are plotted in Figure 4.7(a). These samples are examined with various methods in order to obtain a PSD estimate for this range. The PSD estimate based on the periodogram method is given in Figure 4.7(b) and Figure 4.7(c). A spread of 30 Hz can be seen 50 dB below the zero-Doppler. The same result can be seen from Figure 4.7(d) and Figure 4.7(e), which show the correlogram with biased autocorrelation of the slow-time samples.

In order to compare the result with that of the MIT-LL studies [14], [19], the periodogram in Figure 4.7(c) is plotted with respect to the Doppler velocity (v_D) instead of the Doppler frequency (f_D) according to the following equation [4]:

$$v_D(m/s) = \frac{f_D(Hz) \cdot \lambda(m)}{2} \tag{4.1}$$

---

[4] The measurements of MIT-LL at different frequencies are reported in terms of Doppler velocity for frequency-independent comparison.

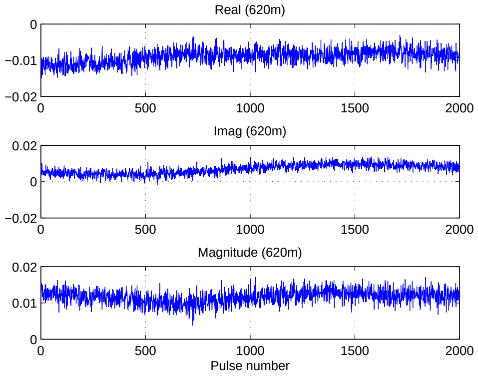

(a) I/Q components and amplitude

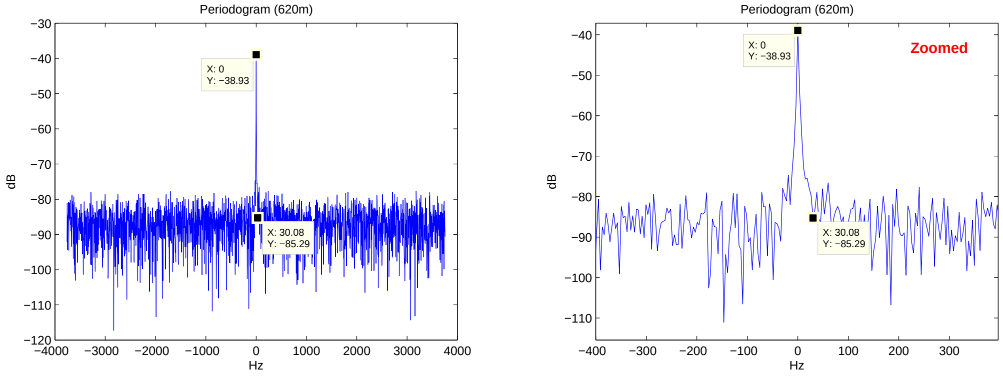

(b) Periodogram

(c) Periodogram (zoomed)

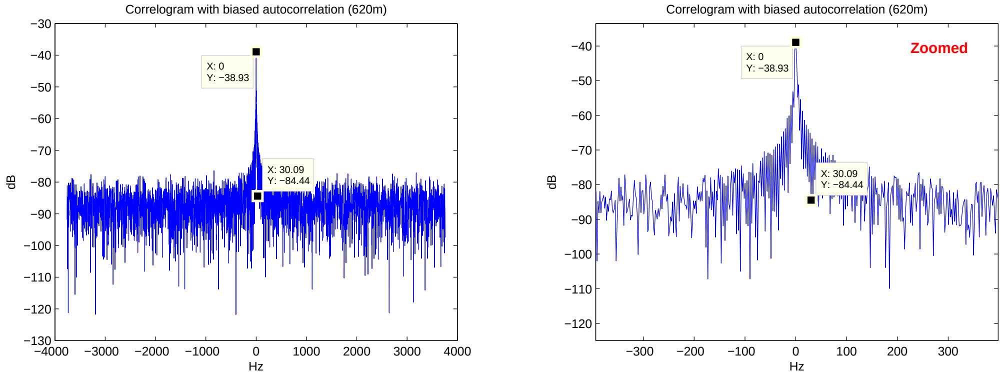

(d) Correlogram

(e) Correlogram (zoomed)

Figure 4.7: PSD estimate based on periodogram and correlogram for the range cell filled with trees (620 m)

As previously discussed in Section 2.2, in [14], it is reported that the measured Doppler velocity spectral extent from windblown trees at levels 60 to 80 dB below the zero-Doppler peak is about 1 m/s under light wind condition. The Doppler velocity increases up to about 3 m/s for windy conditions and it is estimated not to exceed 4 m/s for gale force winds (Figure 4.8(b)).

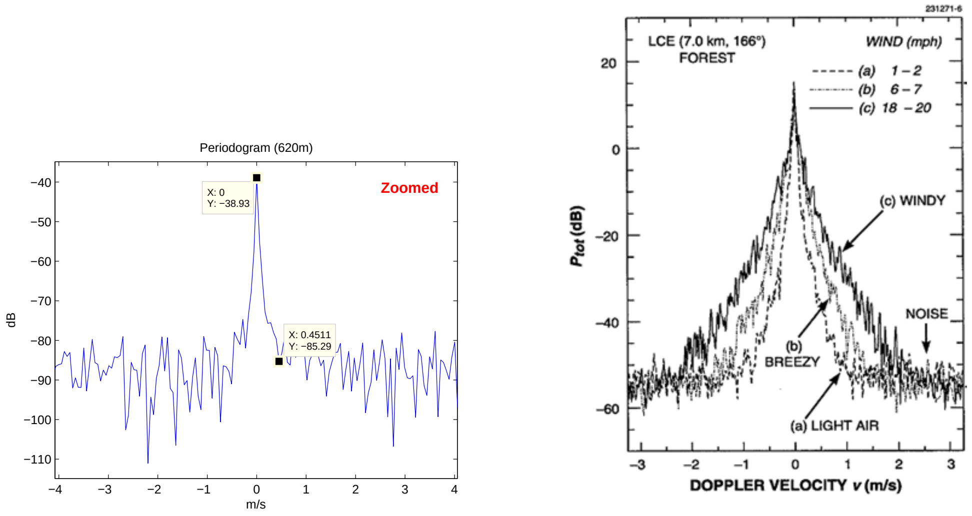

(a) Doppler velocity at 620 m

(b) Results of MIT-LL studies

Figure 4.8: Comparison of the Doppler spread at 620 m with the MIT-LL studies

In this study, the measured Doppler velocity 45 to 50 dB below zero-Doppler is about 0.45 m/s (Figure 4.8(a)) under still air. The dynamic range is smaller than that of the MIT-LL measurement results. Hence, the comparison may be performed for the levels 45 to 50 dB below zero-Doppler. At these levels, the MIT-LL clutter is found to spread up to 0.5 m/s, which is close to the result of this study. However, it should be noted for the future works, the transmitter power of this system should be increased in order to improve the SNR and consequently the dynamic range, so that more reliable comments can be made.

The PSD estimate based on the periodogram has a high variance as it can also be observed from Figure 4.7. In order to improve the variance of the PSD estimate, various methods such as modified periodograms with different windows and Welch method are utilized (Figure 4.9). Among them, the Welch method yields the best result in terms of estimate variance; however, the resolution is decreased considerably. Hence, without decreasing the resolution as much as possible, the variance of the estimate is tried to be decreased with some other methods. For instance, the periodograms or modified periodograms of 3 different records of 2000 pulses each are averaged. According to Figure 4.9(b) and Figure 4.9(c), the Welch method still having the least variance, the averaging seems to work and the result may be improved further by increasing the number of records averaged.

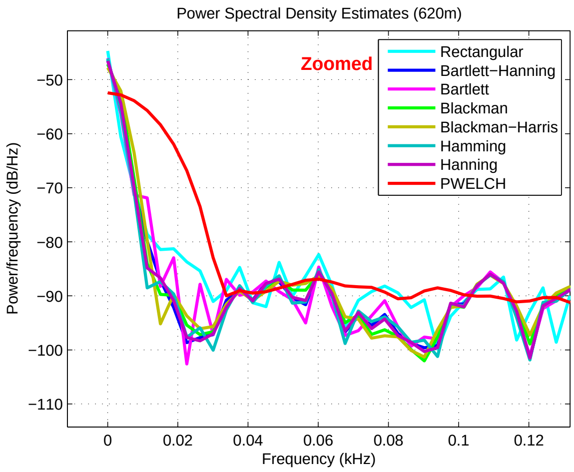

(a) Modified periodogram with different windows and Welch method

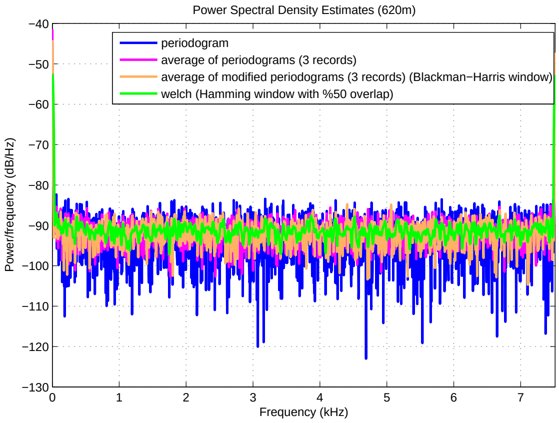

(b) Averaging periodograms and modified periodograms

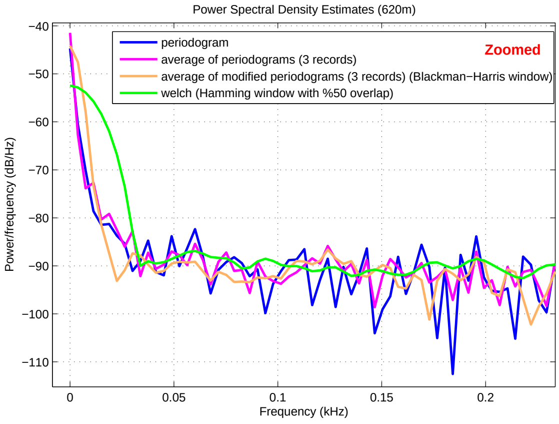

(c) Averaging periodograms and modified periodograms (zoomed)

Figure 4.9: Further spectral analysis of the range cell at 620 m for a better PSD estimate

The next range cell to be analyzed is dominated by a building at 340 m rather than trees. Accordingly, less or no Doppler spread is expected to be observed for this range cell.

The spectral analyses are performed similarly and the results are given in Figure 4.10 and Figure 4.11. The Doppler velocity at levels about 60 dB below zero-Doppler is about 0.06 m/s (Indeed, it corresponds to the first Doppler bin). That is, in contrast to the range cell with trees at 620 m, almost no Doppler spread is observed.

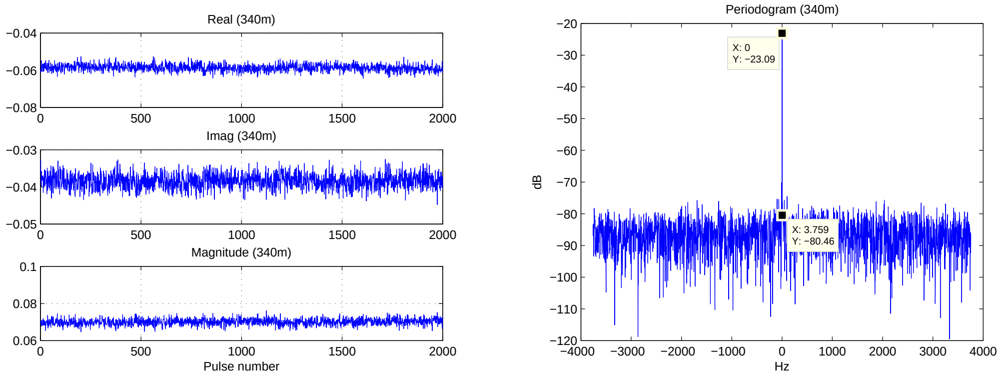

(a) I/Q components and amplitude (b) Periodogram

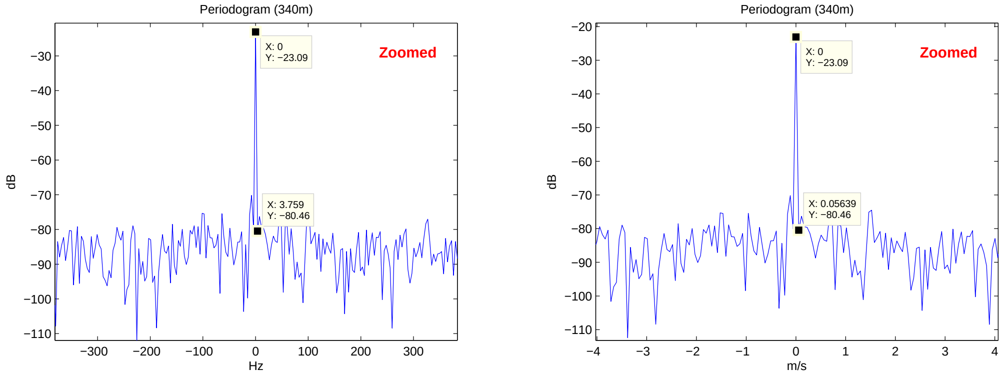

(c) Periodogram (zoomed) (d) Doppler velocity at 340 m

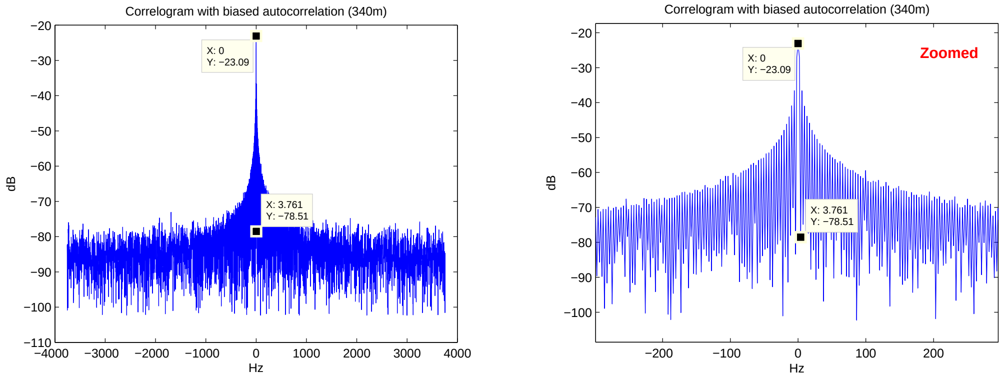

(e) Correlogram (f) Correlogram (zoomed)

Figure 4.10: PSD estimate based on periodogram and correlogram for the range cell with a building in it (340 m)

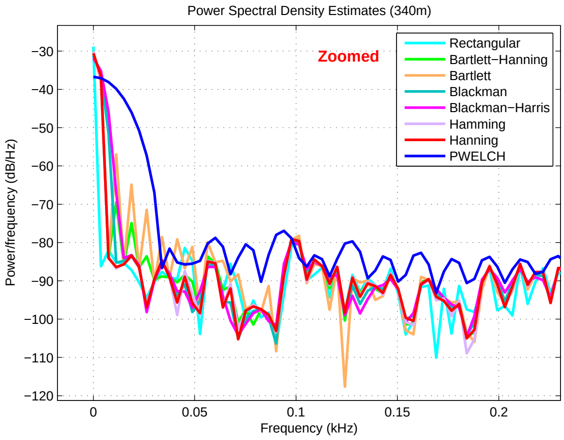

(a) Modified periodogram with different windows and Welch method

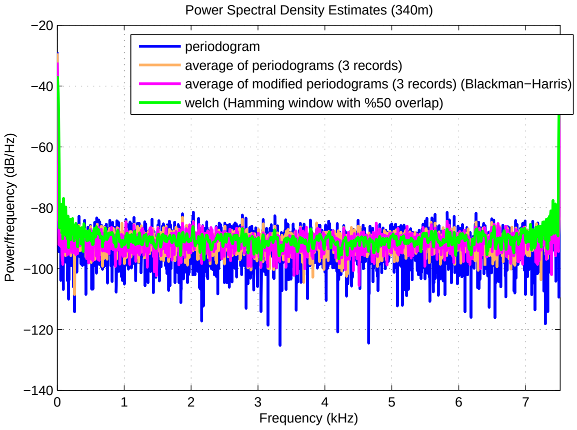

(b) Averaging periodograms and modified periodograms

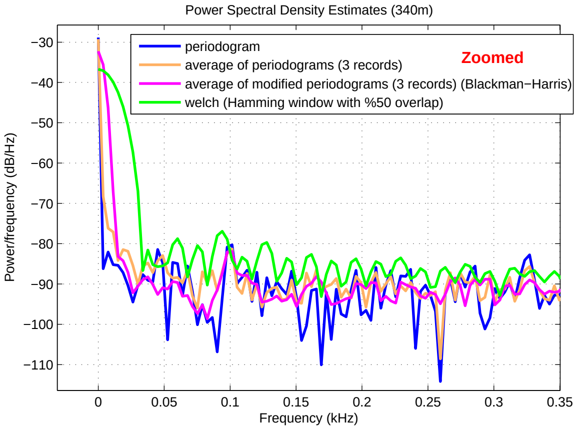

(c) Averaging periodograms and modified periodograms (zoomed)

Figure 4.11: Further spectral analysis of the range cell at 340 m for a better PSD estimate

4.1.3 Statistical Analysis for Terrain - 1

4.1.3.1 Temporal Analysis for Terrain - 1

In this study, the temporal statistical characteristics of the crowded region outside the blind zone are examined. The region between 820 m and 3880 m, which consists of 305 samples, is investigated over time. The number of analyzed pulses is changed in order to check whether the observation time affects the temporal statistics of clutter.

The normality of I and Q data are checked by means of the Lilliefors test. The results are tabulated in Table 4.2 and Table 4.3. According to the tables, it can be said that the number of RCs for which normality is rejected does not seem to be affected with the observation time or number of pulses analyzed.

Table 4.2: Temporal fit of clutter I/Q data between 820 m - 3880 m to Normal distribution (First L pulses)

Number of pulses analyzed (L)	**Corresponding time length**	**Number of RCs for which Normality is rejected - I (LILLIETEST)**	**Number of RCs for which Normality is rejected - Q (LILLIETEST)**
2000	266 msec	19/305	8/305
1000	133 msec	19/305	21/305
500	66.5 msec	13/305	12/305
200	26.6 msec	12/305	17/305
100	13.3 msec	16/305	18/305

Table 4.3: Temporal fit of clutter I/Q data between 820 m - 3880 m to Normal distribution (1:step:2000)

Number of pulses analyzed (1:step:2000)	**step**	**Corresponding time length**	**Number of RCs for which Normality is rejected - I (LILLIETEST)**	**Number of RCs for which Normality is rejected - Q (LILLIETEST)**
2000	1	266 msec	19/305	8/305
1000	2	266 msec	13/305	8/305
500	4	266 msec	19/305	13/305
200	10	266 msec	10/305	12/305
100	20	266 msec	10/305	8/305

On the other hand, the Rayleigh distribution is widely proposed to model temporal characteristics of clutter amplitude in an RC as discussed in Section 2.3.2.1. Hence, the fit of empirical clutter amplitude to Rayleigh distribution is checked with both the standard KS test and the modified KS (MKS) test with the Monte Carlo approach (with a significance level of 0.05). For each of 305 RCs, the parameters of the Rayleigh distribution are estimated from the empirical clutter amplitude with ML method. The results are given in Table 4.4 and Table 4.5.

Table 4.4: Temporal fit of clutter amplitude between 820 m - 3880 m to Rayleigh distribution (First L pulses)

Number of pulses analyzed (L)	**Corresponding time length**	**Number of RCs for which Rayleigh is rejected (KS TEST)**	**Number of RCs for which Rayleigh is rejected (MKS TEST)**
2000	266 msec	94/305	120/305
1000	133 msec	77/305	103/305
500	66.5 msec	63/305	96/305
200	26.6 msec	44/305	73/305
100	13.3 msec	32/305	63/305

Table 4.5: Temporal fit of clutter amplitude between 820 m - 3880 m to Rayleigh distribution (1:step:2000)

Number of pulses analyzed (1:step:2000)	**step**	**Corresponding time length**	**Number of RCs for which Rayleigh is rejected (KS TEST)**	**Number of RCs for which Rayleigh is rejected (MKS TEST)**
2000	1	266 msec	94/305	120/305
1000	2	266 msec	76/305	107/305
500	4	266 msec	63/305	94/305
200	10	266 msec	48/305	82/305
100	20	266 msec	29/305	70/305

First of all, the standard KS test is expected to reject the hypothesized distribution less, since it is made closer to the empirical distribution by estimating the parameters from the empirical data as discussed in Section 2.3.4. Indeed, the number of RCs for which Rayleigh is rejected by the MKS test is greater than the number in the standard KS test in Table 4.4 and Table 4.5.

Second, it can be seen that the rejection of Rayleigh distribution increases as the number of analyzed pulses increases as opposed to the normality rejection. For the MKS test, the ratio of rejection increases from 20% to 40% as the observation time increases from 13.3 msec to 266 msec or the number of pulses increases from 100 to 2000.

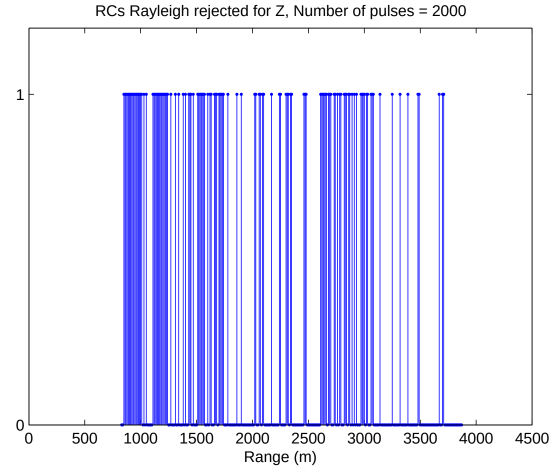

(a) RCs for which Rayleigh distribution is rejected to model clutter amplitude

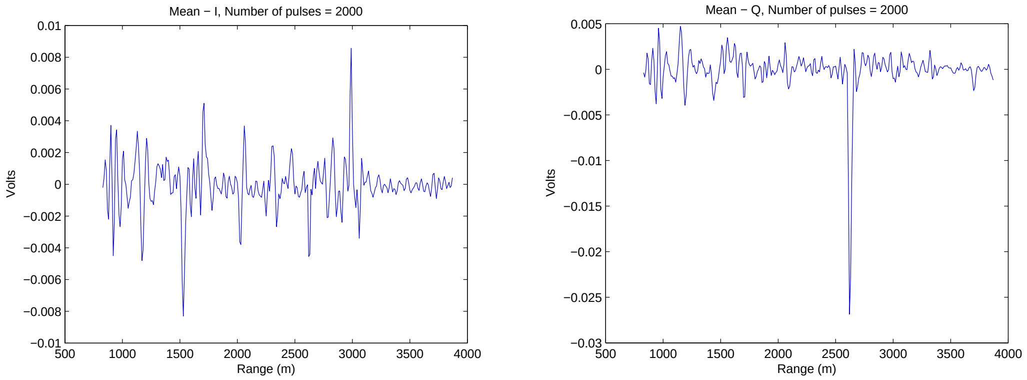

(b) Mean of I component in each RC

(c) Mean of Q component in each RC

Figure 4.12: Temporal analysis of clutter amplitude between 820 m - 3880 m in 266 msec

To better understand the results, consider the plot which shows the RCs for which Rayleigh is rejected to model clutter amplitude (Figure 4.12(a)). When this plot is compared to the range characteristic of the region which is given in Figure 4.4, it can be seen that the RCs for which Rayleigh is rejected and the peaks of the power vs. range plot are quite correlated. That is, an RC with a scatterer in it tends to reject Rayleigh clutter amplitude. This may be interpreted as follows: Considering the structure of the terrain with mostly point scatterers, an RC may be dominated by one scatterer since the range resolution of the system is quite fine. Hence, the clutter amplitude in time may deviate from Rayleigh and be rather modeled with Ricean distribution. The point of Ricean distribution is that both I and Q have non-zero means. This explains the result of relatively less rejection of I/Q normality than that of Rayleigh model for clutter amplitude: I and Q may still be normally distributed, although Rayleigh amplitude requires normal I/Q components with zero mean. Actually, the consistency between non-zero mean of I/Q data and the tendency to reject Rayleigh amplitude can be seen from Figure 4.12(b) and Figure 4.12(c) which show the spatial change of temporal means of I/Q components over 820 m - 3880 m.

4.1.3.2 Spatial Analysis for Terrain - 1

So far, the temporal statistical characteristics of the clutter have been explored. Next, the spatial statistical analysis is carried out over the fast time axis after the spatial calibration operation explained in Section 2.3.1.1 is performed.

For instance, consider the samples between 820 m - 3880 m in the 20th pulse. According to the Lilliefors test and the skewness - kurtosis values, the I/Q data deviates from normality. It can be seen from Figure 4.13(a) and Figure 4.13(b). Since the skewness of the I component is much closer to zero than that of the Q component, the histogram of the I component is expected to be relatively more symmetrical. Similarly, the kurtosis values are greater for the Q component. Consequently, its histogram is spikier.

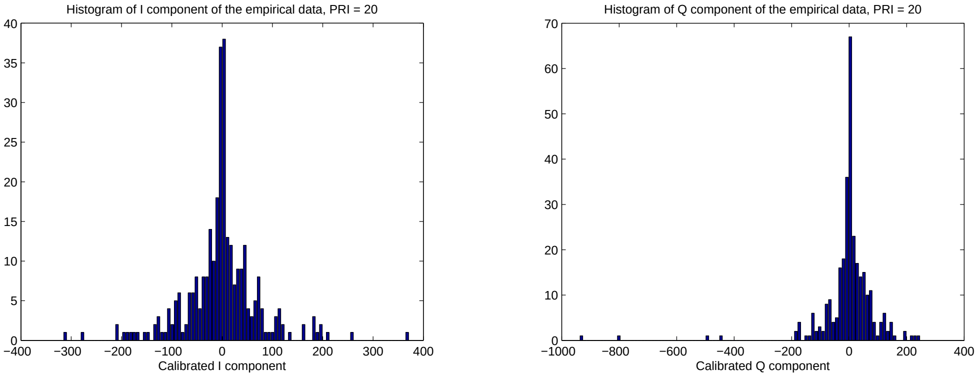

(a) (b)

Figure 4.13: Histogram of the I and Q components between 820 m - 3880 m for the 20th pulse

On the other hand, the histogram and the cumulative histogram of the corresponding 305 calibrated amplitude samples are given in Figure 4.14(b) and Figure 4.14(c). The Rayleigh, Log-normal and Weibull models are checked to model clutter amplitude. ML estimates of the parameters are used and the MKS test is applied with a significance level of 0.05. The results are given in Figure 4.14(d) - 4.14(f). Log-normal and Rayleigh are rejected while the Weibull distribution is not rejected.

Then, the space-time compound analyses are performed for the same range interval. The texture and speckle components are derived as explained in Section 2.3.3.1. Using the MKS test, the speckle is found to be Rayleigh distributed. For the clutter amplitude to be K-distributed, the texture should be Gamma distributed. However, the texture does not fit to any of the Gamma, Log-normal and Exponential distributions. The results are shown in Figure 4.15.

In addition, the spatial analyses performed on the range interval of 820 m - 3880 m for the 20th pulse are repeated for the first 50 pulses. For each pulse, the normality of I/Q data is checked by the Lilliefors test, and the MKS test is applied in order to check the fit of the clutter amplitude to the Rayleigh, Log-normal and Weibull distributions. The significance level is 0.05 for all tests. The results are given in Table 4.6.

Table 4.6: Spatial fit of I/Q data and amplitude of clutter for the first 50 pulses (820 m - 3880 m)

Lillifors test results for I/Q components 820 m - 3880 m (305 samples)	**MKS test results for clutter amplitude 820 m - 3880 m (305 samples)**
• I - Normality rejected for 50 pulses out of 50 pulses • Q - Normality rejected for 50 pulses out of 50 pulses	• Rayleigh rejected for 50 pulses out of 50 pulses • Log-normal rejected for 50 pulses out of 50 pulses • Weibull rejected for 18 pulses out of 50 pulses

As it can be seen from Table 4.6, normality of I/Q data is rejected for all pulses. Also, the skewness and kurtosis values calculated for each pulse are consistent with this result. Among all, the values for the 10th, 20th, 30th, 40th and 50th pulses are tabulated in Table 4.7 as an

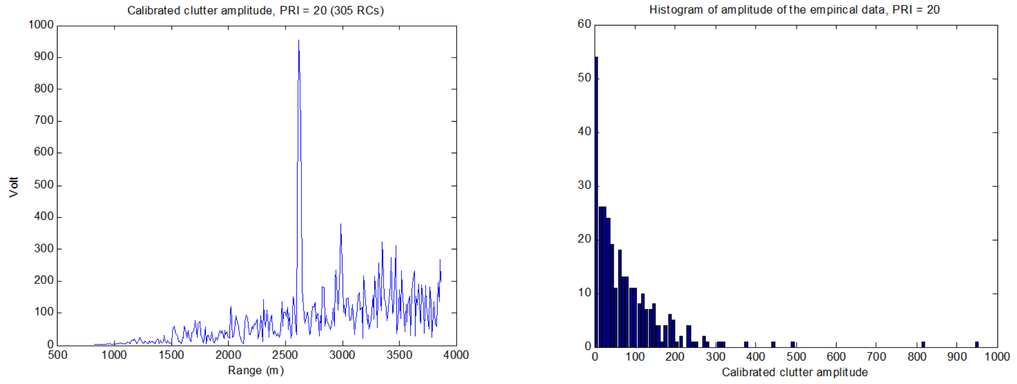

(a) (b)

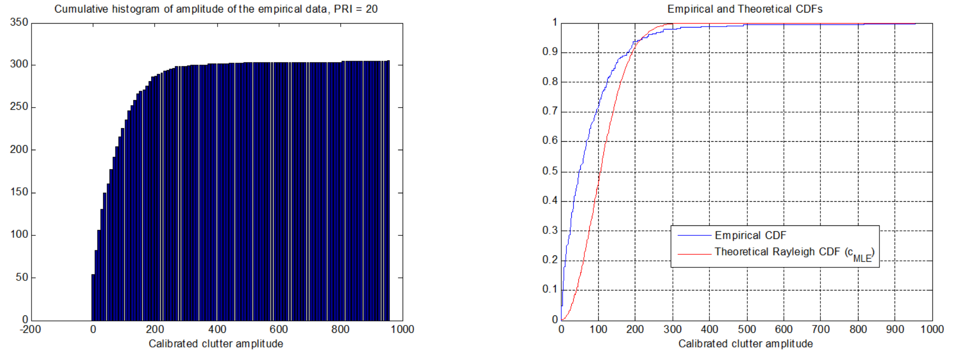

(c)

p-value = 0% < 5%

→ RAYLEIGH REJECTED

(d)

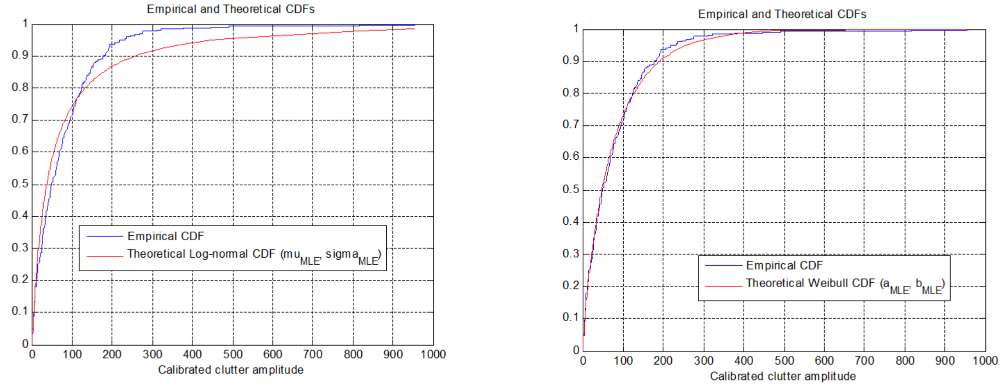

p-value = 0% < 5%

→ LOG-NORMAL REJECTED

(e)

p-value = 27.14% > 5%

→ **WEIBULL NOT REJECTED**

(f)

Figure 4.14: Spatial analysis of clutter amplitude between 820 m - 3880 m for the 20th pulse

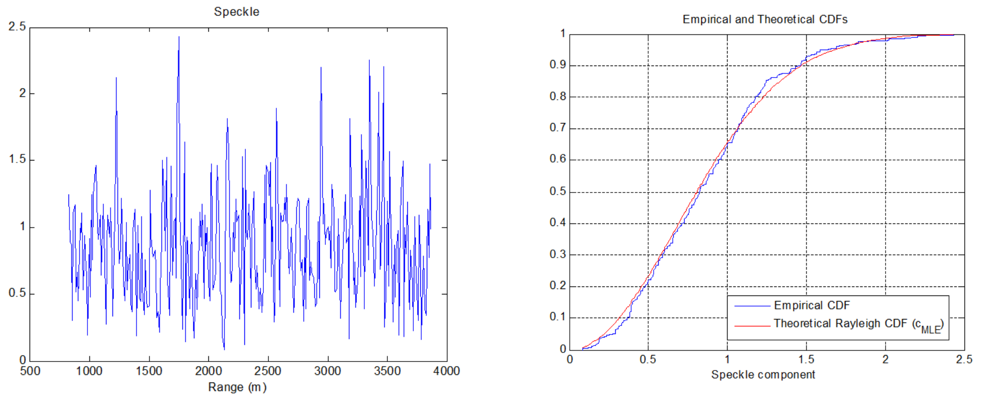

$\longrightarrow$ p-value = 41.66% > 5%
Rayleigh speckle NOT rejected

(a)

(b)

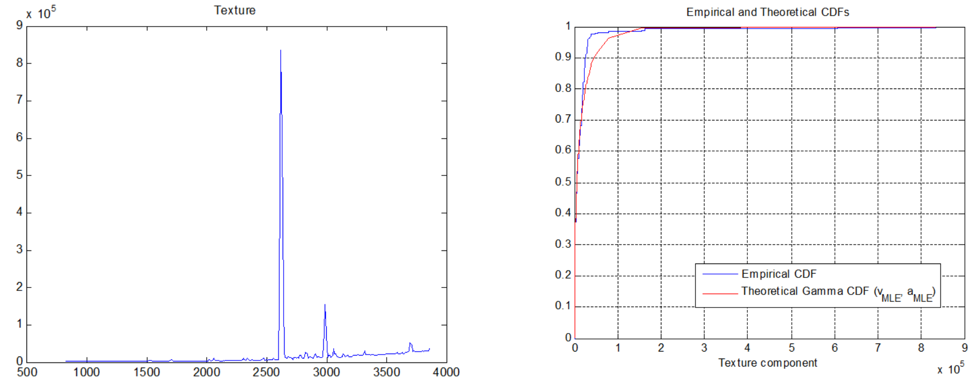

p-value = 0% < 5%
$\longrightarrow$ Gamma texture rejected

(c)

(d)

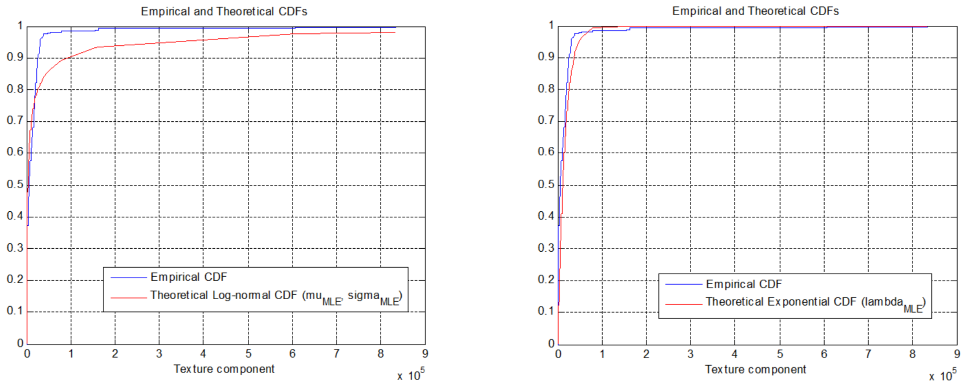

value = 0% < 5%
$\longrightarrow$ Log-normal texture rejected

(e)

p-value = 0% < 5%
$\longrightarrow$ Exponential texture rejected

(f)

Figure 4.15: Space - time compound analysis of clutter amplitude between 820 m - 3880 m for the 20th pulse

Table 4.7: I/Q skewness and kurtosis values for pulse number = 10, 20, 30, 40, 50 (820 m - 3880 m)

Pulse number	SKEWNESS-I	KURTOSIS-I	SKEWNESS-Q	KURTOSIS-Q
10	0.328	-3.122	2.952	22.157
20	0.137	-4.451	4.140	34.649
30	0.325	-3.951	1.951	29.106
40	0.220	-3.528	3.124	24.691
50	0.393	-4.175	3.393	31.684

example.

On the other hand, the Rayleigh distribution is rejected to model the clutter amplitude. This result is expected since the range heterogeneity of clutter dominates for high range resolution. The Log-normal distribution is also rejected for all pulses while the Weibull distribution is rejected with 40%.

Instead of analyzing the full range of 820 m - 3880 m, smaller windows may be investigated. A window of size W is swept over the fast time samples in order to observe the change of spatial characteristics of clutter amplitude. In this study, three different window sizes are used: 25, 50 and 100 samples, which correspond to a window length of 250 m, 500 m, and 1 km, respectively. For each window, the parameters are estimated by ML method and the spatial changes of these parameters are plotted. Also, in each window, the MKS test is applied for the corresponding theoretical model. The results of MKS test are assessed together with the spatial change of the distribution parameters.

The results of the analyses for the 20th pulse with three different window sizes are given in Figure 4.16, Figure 4.17, and Figure 4.18. For each window size, the shape and scale parameters of Log-normal and Weibull distributions are plotted so that the x-axis shows the range where a window starts. For instance, for W = 50, the parameter estimate read at 1000 m belongs to the window between 1000 m and 1500 m.

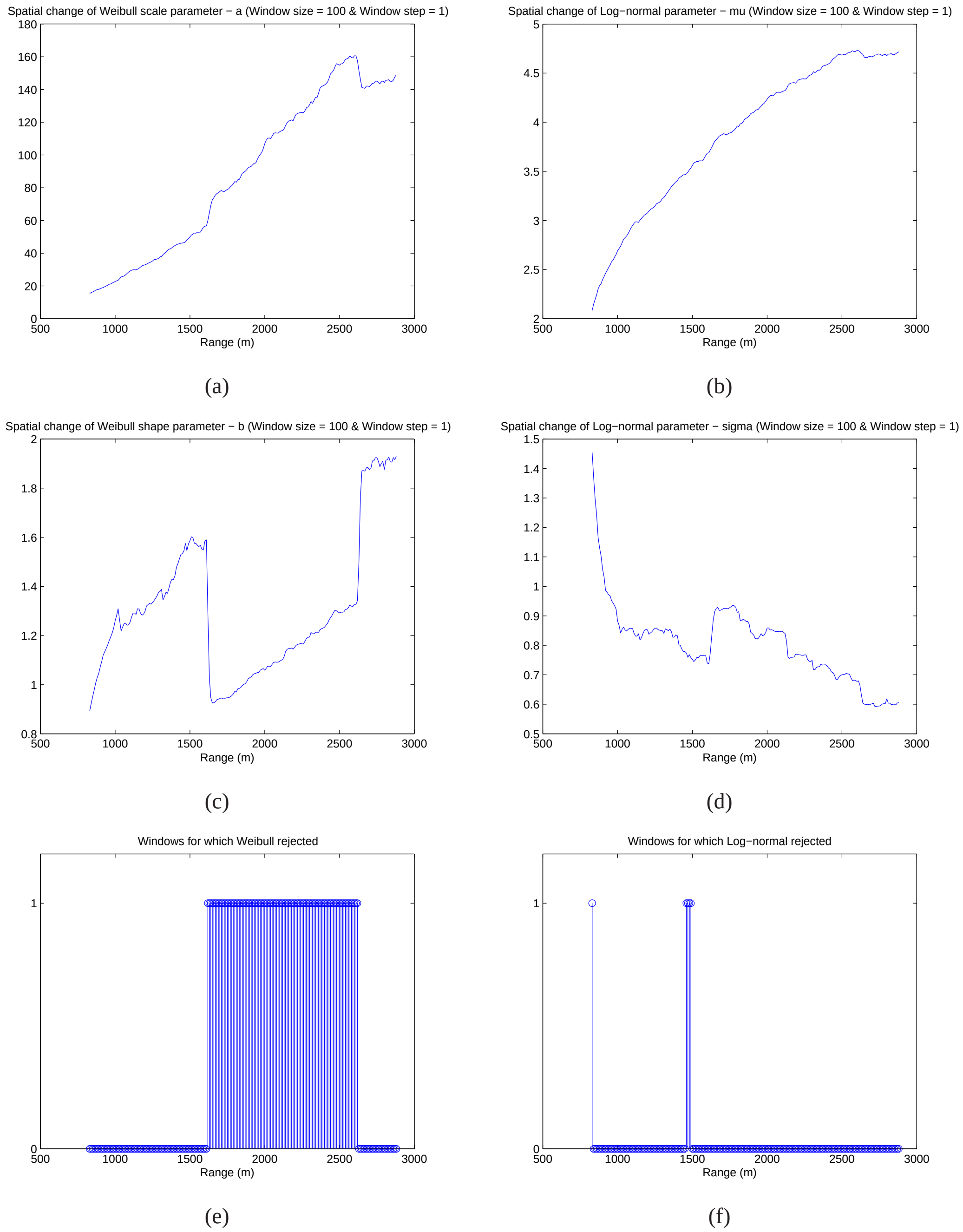

(a) (b) (c) (d) (e) (f)

Figure 4.16: Spatial changes of the shape and scale parameters of Weibull and Log-normal distributions for the 20th pulse (Window size = 100)

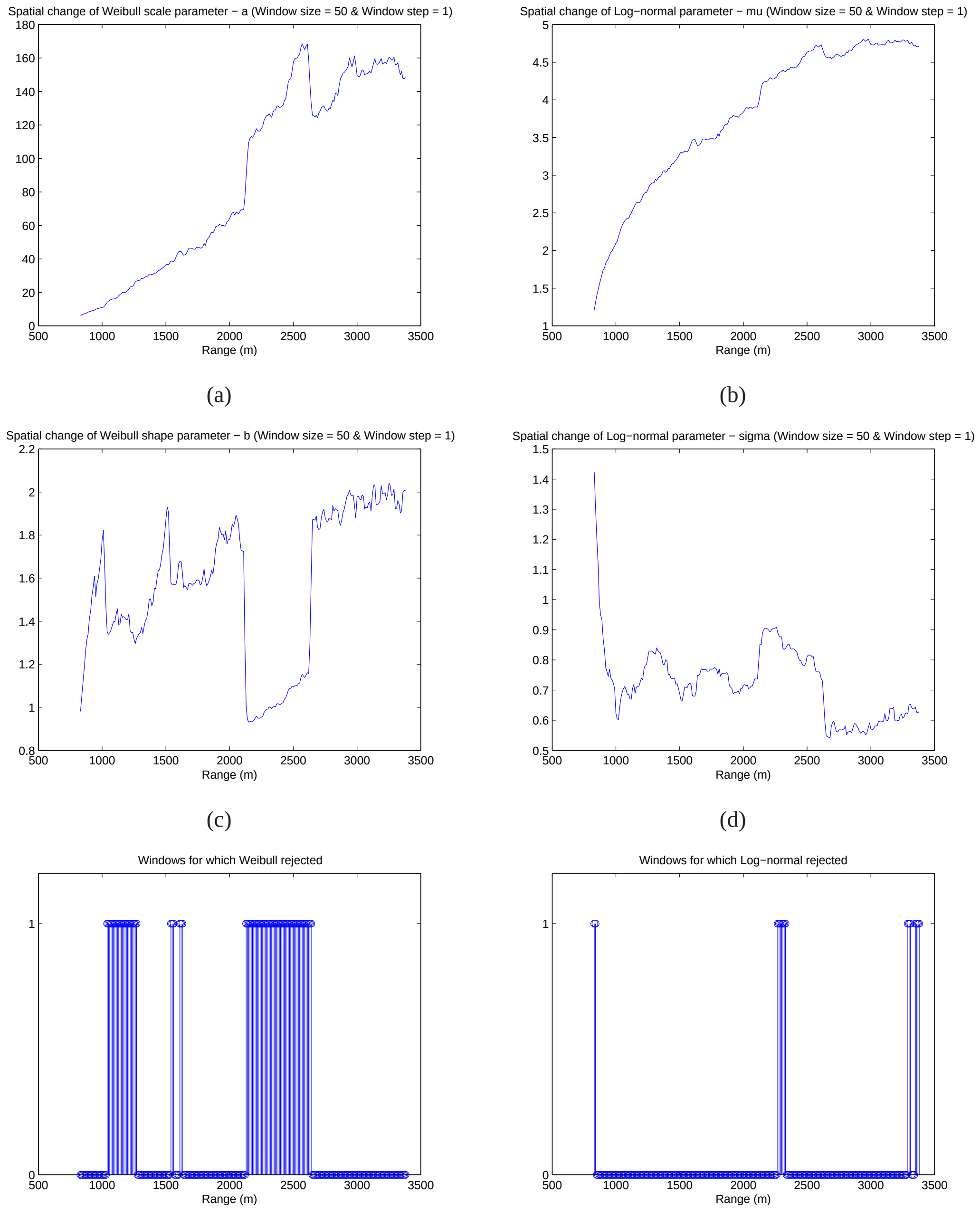

(a) (b)

(c) (d)

(e) (f)

Figure 4.17: Spatial changes of the shape and scale parameters of Weibull and Log-normal distributions for the 20th pulse (Window size = 50)

(a) (b)

(c) (d)

(e) (f)

Figure 4.18: Spatial changes of the shape and scale parameters of Weibull and Log-normal distributions for the 20th pulse (Window size = 25)

First of all, it should be noted that as the window size decreases, the spatial change of shape or scale parameters becomes more apparent. On the other hand, for smaller windows, the distribution fitting is performed based on less samples. This trade-off should be considered before deciding on the window size. That is, the window size should be fine enough to extract the spatial characteristics of the region while containing sufficient samples for a successful distribution fitting.

According to the Figures 4.16 - 4.18, as the window size decreases, the rejection of Weibull decreases while the rejection of Log-normal increases. This result may be explained as follows: The smaller the window size is, the more homogeneous the window becomes. Hence, the variance of a window decreases and the tails becomes lighter yielding the Log-normal model to be rejected more.

In both of the Weibull and Log-normal plots, the scale parameter seems to be much more related to the spatial calibration operation than the shape parameter. That is, it can be roughly inferred that the scale parameter is connected with the power level of the returns while the shape parameter depends on the dispersion of the scatterers on the terrain.

For detailed analysis, consider the estimates of the parameters over a window of W = 50 (500 m) given in Figure 4.17. The shape parameter of Weibull distribution decreases mainly in three points (Figure 4.17(c)). A decrease in the shape parameter of Weibull means an increase in the variance and a heavier tail. Hence, such heterogeneous regions may be considered as clutter edges. The MKS test result for each window plotted in Figure 4.17(e) also seems to be correlated with these edges. That is, for the windows rejected to be modeled with Weibull distribution, the shape parameter estimation decreases sharply. Besides, Log-normal distribution may be proposed to model these windows based on Figure 4.17(e) and Figure 4.17(f). As opposed to the result of the full range, i.e., 820 m - 3880 m, for smaller windows Log-normal is accepted and the Weibull is rejected more.

4.1.4 Surface Clutter Reflectivity for Terrain - 1

In this section, the clutter RCS and reflectivity are calculated for the range interval of 820 m - 3880 m.

The radar power equation given in (2.50) is used to calculate the clutter RCS (σ_C). The required parameters are tabulated in Table 4.8 and the CNR values are obtained from the power vs. range plot for this terrain (Figure 4.4). Here, it is important to note that the CNR values obtained from the range-Doppler plot include the improvement factors due to the pulse compression and coherent pulse integration. Hence, the actual CNR values without improvements should be used in (2.50). These CNR values are plotted in Figure 4.19(a).

Once σ_C is calculated from (2.50), the clutter reflectivity (σ_0) is obtained by dividing the σ_C into the range cell area, which is calculated considering the azimuthal beamwidth of the antenna (θ) and the grazing angle (ψ).

Table 4.8: Parameters for calculation of clutter reflectivity

Parameter	**Value**
P_T	7.5 dBm
$G_T + G_R$	27.2 dB
G_{LNA}	36 dB
λ	0.03 m
T	298 °K
B	7.5 MHz
F	3.3 dB
L	10 dB
θ	30 °
ψ	0 °
Number of chips	16 dB
Number of integrated pulses	33 dB

The resulting clutter RCS and clutter reflectivity for Terrain - 1 are given in Figure 4.19(b) and Figure 4.19(d), respectively.

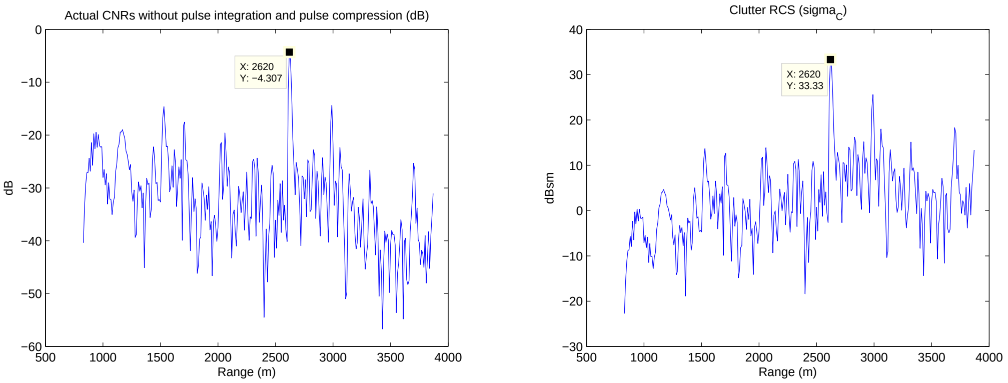

(a) Actual CNRs without improvement factors

(b) Clutter RCS

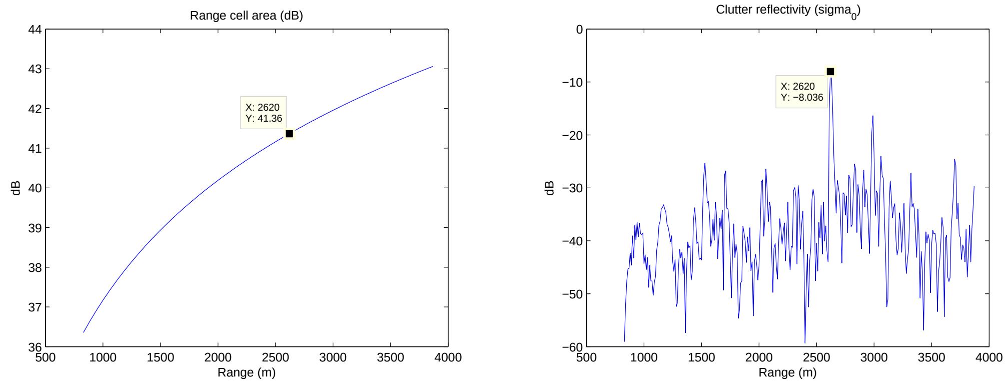

(c) Range cell area

(d) Clutter reflectivity

Figure 4.19: Clutter RCS and reflectivity for 820 m - 3880 m

4.2 Terrain - 2

The second illuminated terrain can be seen in Figure 4.20.

Figure 4.20: Terrain - 2 on the day of measurements

Before analyses, the similar preliminary work is conducted for the second terrain, such as determination of the boundaries, altitude profiles and the shadowed regions of the illuminated area. The altitude profiles are given in Appendix D.2. Analyzing the hills inside the beam of the antenna from these profiles, the points shadowing their backs are marked with blue pointers. According to these pointers, a horizon line is expected to be seen at about 5.5 km.

4.2.1 Range-Doppler Processing for Terrain - 2

The power vs. range plot for this terrain is given in Figure 4.22(a). According to this plot, there is no return beyond 5 km, as opposed to Terrain - 1. Considering the high buildings located just before the peak of the first hill, the horizon line which is expected to be at 5.5 km may be brought closer to 5 km. Hence, the result seems to be reasonable. Excluding the blind zone from the analyses, the range-Doppler graph can be plotted as in Figure 4.22(b).

Figure 4.21: Ranges of the possible scatterers in Terrain - 2

The blind zone for this terrain is composed of many trees which yields a Doppler spread up to 25-30 Hz. The range-Doppler plot for this terrain is given in Figure 4.23.

4.2.2 Spectral Analysis for Terrain - 2

For detailed spectral analyses, the range cell at 380 m is chosen (Figure 4.24) and the results are plotted in Figure 4.25 and Figure 4.26. The Doppler velocity for this range under light air is found to be about 0.4 m/s at levels 45 dB below zero-Doppler peak (Figure 4.25(d)).

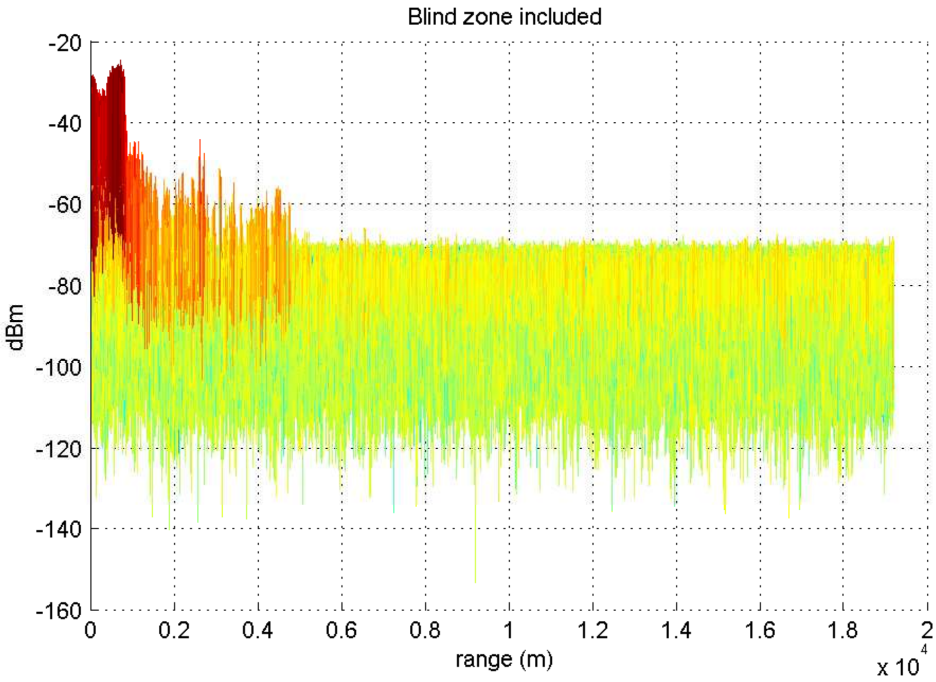

(a) Blind zone included

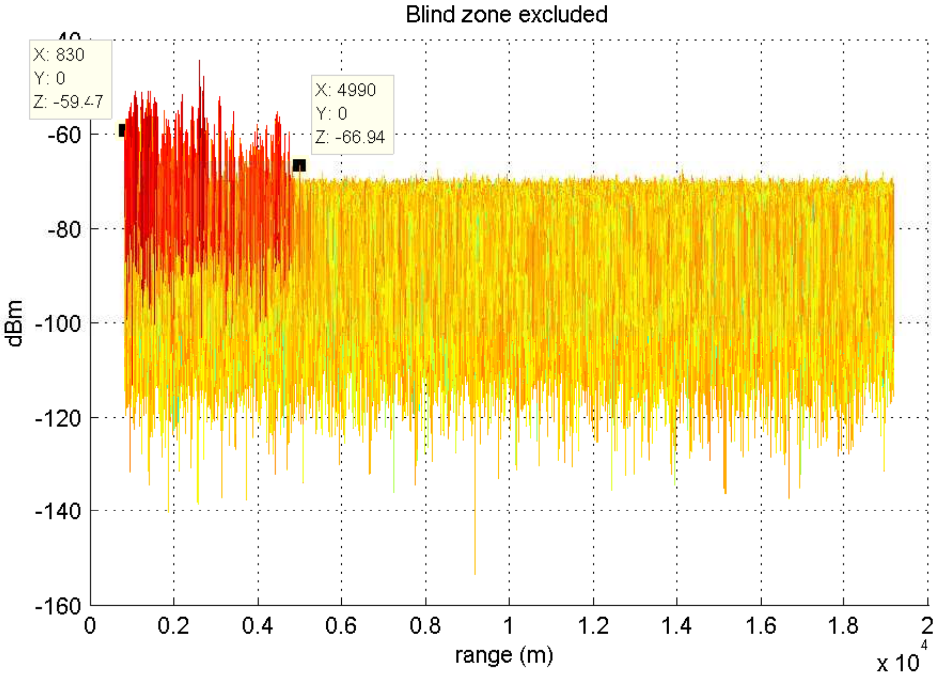

(b) Blind zone excluded

Figure 4.22: Power vs. range plot for Terrain - 2

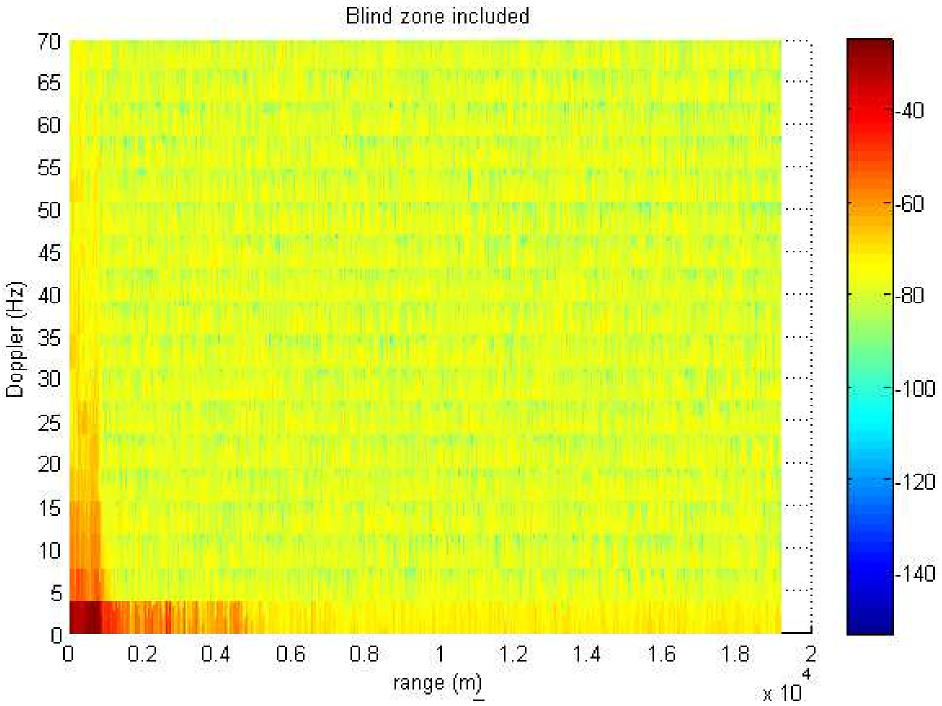

Figure 4.23: Doppler vs. range plot for Terrain - 2 with blind zone included (0 - 70 Hz)

(a) (b)

Figure 4.24: RC at 380 m for detailed spectral analyses (Terrain - 2)

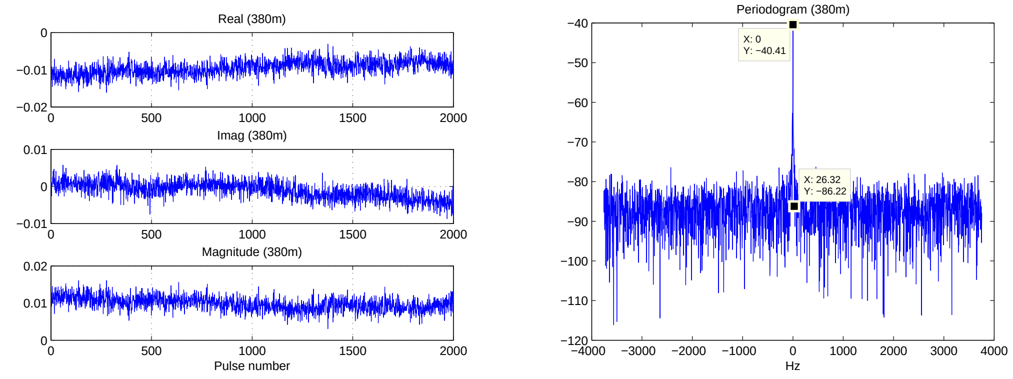

(a) I/Q components and amplitude (b) Periodogram

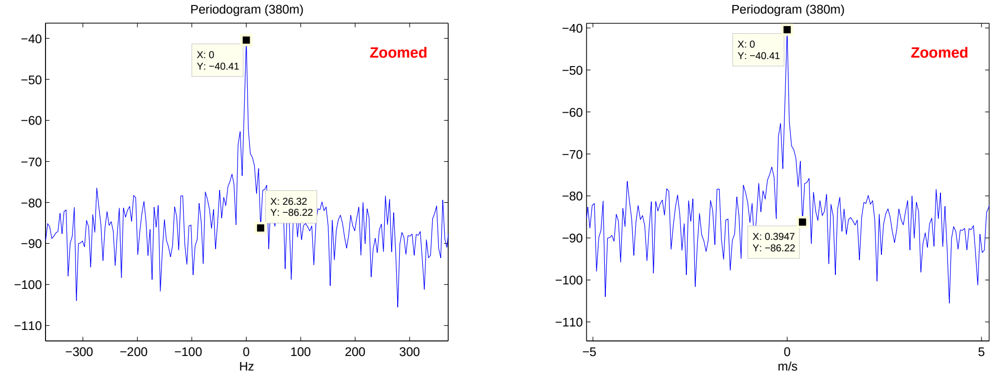

(c) Periodogram (zoomed) (d) Doppler velocity at 380 m

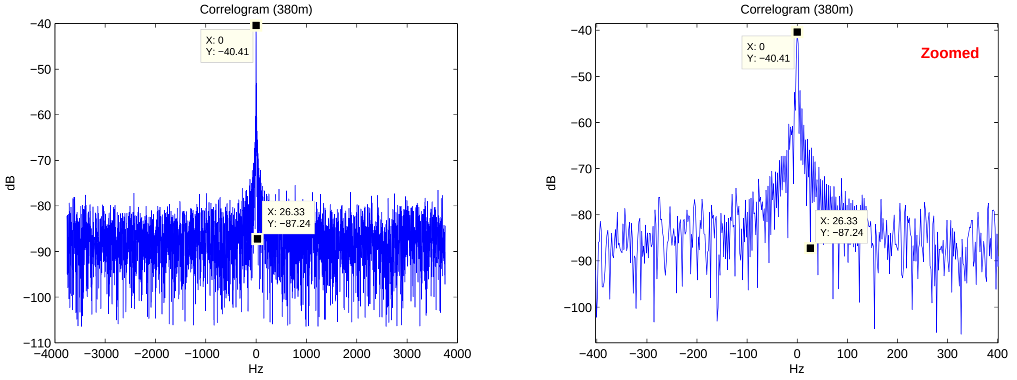

(e) Correlogram (f) Correlogram (zoomed)

Figure 4.25: PSD estimate based on periodogram and correlogram for the range cell filled with trees (380 m)

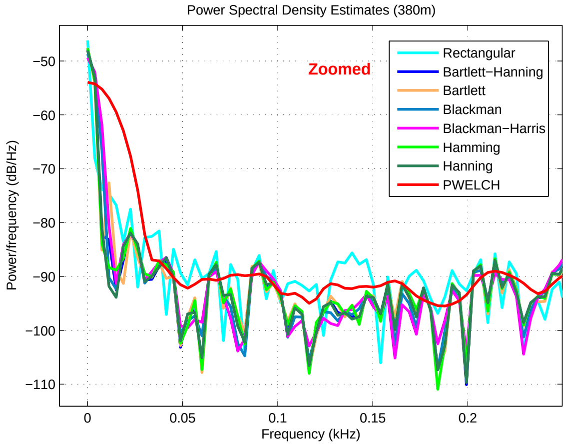

(a) Modified periodogram with different windows and Welch method

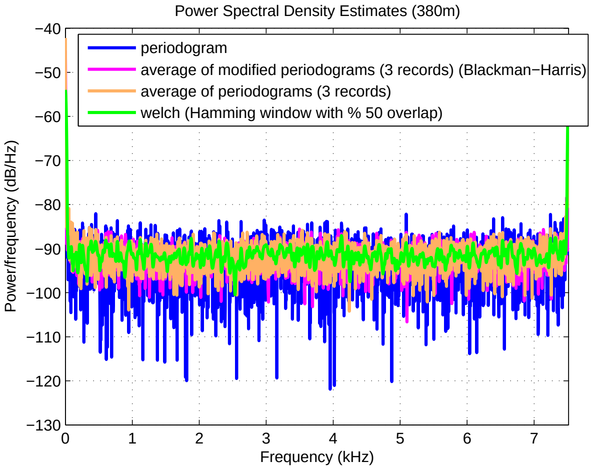

(b) Averaging periodograms and modified periodograms

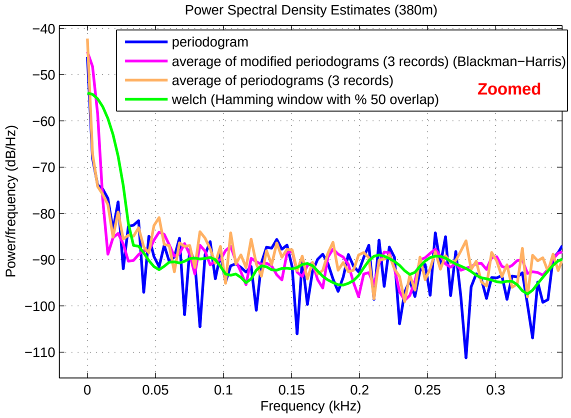

(c) Averaging periodograms and modified periodograms (zoomed)

Figure 4.26: Further spectral analysis of the range cell at 380 m for a better PSD estimate

4.2.3 Statistical Analysis for Terrain - 2

4.2.3.1 Temporal Analysis for Terrain - 2

The temporal analyses performed for Terrain - 2 are tabulated in Table 4.9 - 4.12. The blind zone is excluded from the analyses and 417 samples between 820 m - 4990 m are examined over different number of pulses. Table 4.9 and Table 4.11 give the analysis results of the first L pulses for each range. Also, for each range, keeping the observation time constant, each of 2, 4, 10 and 20 pulses are analyzed. The results are in Table 4.10 and Table 4.12.

Table 4.9: Temporal fit of clutter I/Q data between 820 m - 4990 m to Normal distribution (First L pulses)

Number of pulses analyzed (L)	**Corresponding time length**	**Number of RCs for which Normality is rejected - I (LILLIETEST)**	**Number of RCs for which Normality is rejected - Q (LILLIETEST)**
2000	266 msec	15/417	12/417
1000	133 msec	19/417	20/417
500	66.5 msec	14/417	26/417
200	26.6 msec	23/417	23/417
100	13.3 msec	25/417	25/417

Table 4.10: Temporal fit of clutter I/Q data between 820 m - 4990 m to Normal distribution (1:step:2000)

Number of pulses analyzed (1:step:2000)	**step**	**Corresponding time length**	**Number of RCs for which Normality is rejected - I (LILLIETEST)**	**Number of RCs for which Normality is rejected - Q (LILLIETEST)**
2000	1	266 msec	15/417	12/417
1000	2	266 msec	21/417	20/417
500	4	266 msec	22/417	28/417
200	10	266 msec	24/417	24/417
100	20	266 msec	16/417	20/417

Table 4.11: Temporal fit of clutter amplitude between 820 m - 4990 m to Rayleigh distribution (First L pulses)

Number of pulses analyzed (L)	**Corresponding time length**	**Number of RCs for which Rayleigh is rejected (KS TEST)**	**Number of RCs for which Rayleigh is rejected (MKS TEST)**
2000	266 msec	5/417	32/417
1000	133 msec	2/417	35/417
500	66.5 msec	4/417	23/417
200	26.6 msec	1/417	23/417
100	13.3 msec	0/417	19/417

Table 4.12: Temporal fit of clutter amplitude between 820 m - 4990 m to Rayleigh distribution (1:step:2000)

Number of pulses analyzed (1:step:2000)	**step**	**Corresponding time length**	**Number of RCs for which Rayleigh is rejected (KS TEST)**	**Number of RCs for which Rayleigh is rejected (MKS TEST)**
2000	1	266 msec	5/417	32/417
1000	2	266 msec	1/417	30/417
500	4	266 msec	1/417	26/417
200	10	266 msec	1/417	18/417
100	20	266 msec	1/417	24/417

According to Table 4.9 and Table 4.10, the normality of I/Q data is accepted with a high percentage and the result does not seem to depend on the number of pulses analyzed or the observation time.

On the other hand, the results of MKS tests checking the fit of clutter amplitude to Rayleigh model show that Rayleigh is rejected with a ratio not higher than 10%. As opposed to Terrain - 1, the Rayleigh seems to be a suitable model for temporal clutter amplitude. This is an expected result, since a range cell in Terrain - 2 is mostly composed of diffuse components in contrast to Terrain - 1.

4.2.3.2 Spatial Analysis for Terrain - 2

For the spatial characterization of clutter, 417 samples corresponding to the range 820 m - 4990 m are analyzed after spatial calibration as in Terrain - 1.

As an example, the results of the 1st pulse are presented in Figure 4.27. According to the MKS test performed with ML estimates of the parameters, Log-normal and Rayleigh are rejected and Weibull is accepted.

For the space-time compound analyses performed for the same range interval and the same pulse, the texture and speckle components and their GoF test results are also shown in Figure 4.28. The speckle is found to be Rayleigh distributed, however none of the Gamma, Log-normal and Exponential distributions is successful to model the texture component.

The above spatial tests are again repeated for the first 50 pulses and the results are tabulated in Table 4.13. The Rayleigh and Log-normal models are not accepted for any of the 50 pulses. On the other hand, the ratio of Weibull rejection is found to be quite high as opposed to the Terrain - 1 results. For 80% of the pulses, Weibull model is rejected. Here, it will be better to analyze the spatial characteristics of clutter amplitude in smaller windows.

Table 4.13: Spatial fit of I/Q data and amplitude of clutter for the first 50 pulses (820 m - 4990 m)

Lillifors test results for I/Q components 820 m - 4990 m (417 samples)	**MKS test results for clutter amplitude 820 m - 4990 m (417 samples)**
• I - Normality rejected for 50 pulses out of 50 pulses • Q - Normality rejected for 50 pulses out of 50 pulses	• Rayleigh rejected for 50 pulses out of 50 pulses • Log-normal rejected for 50 pulses out of 50 pulses • Weibull rejected for 39 pulses out of 50 pulses

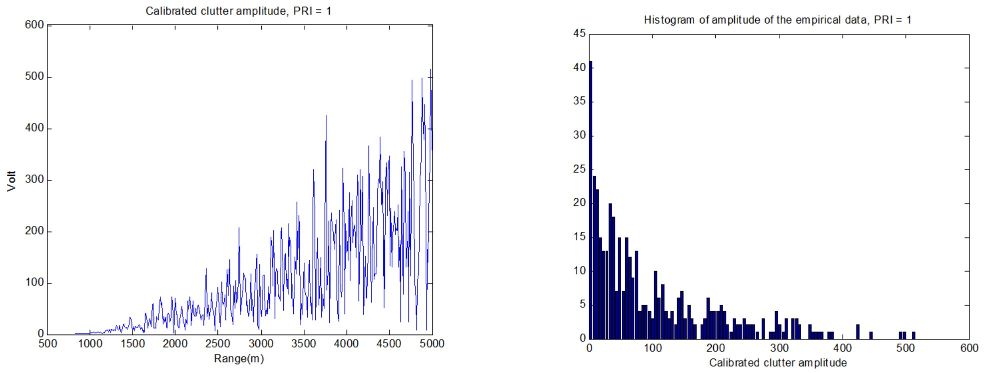

(a) (b)

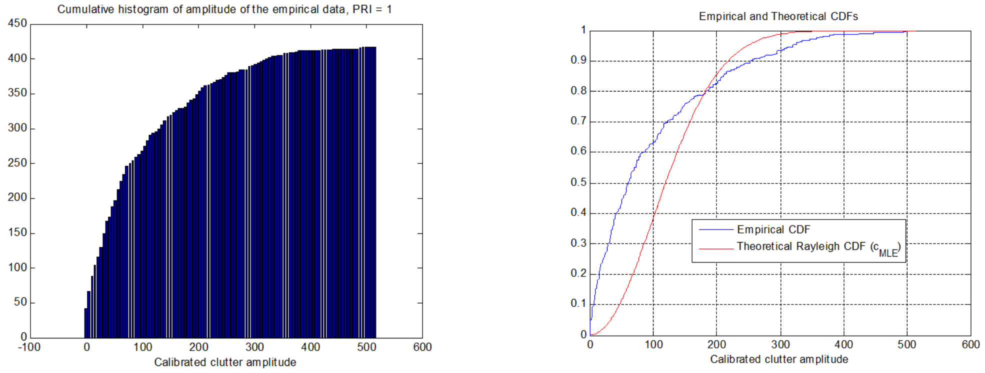

p-value = 0% < 5%

→ RAYLEIGH REJECTED

(c) (d)

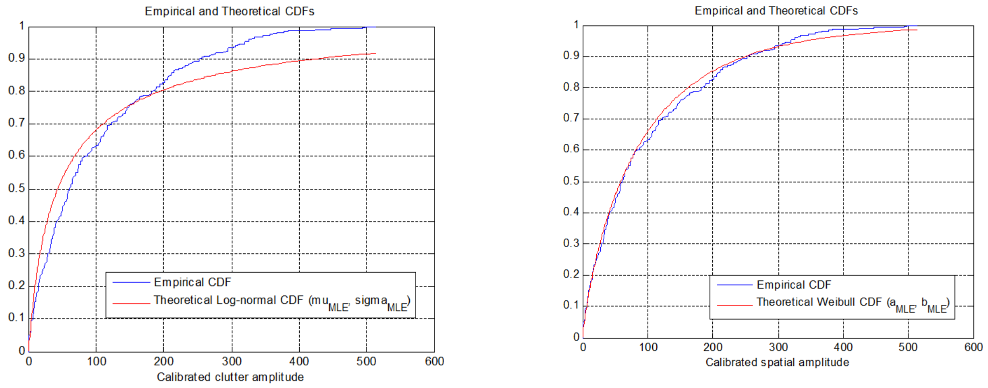

p-value = 0% < 5%

→ LOG-NORMAL REJECTED

(e)

p-value = 12.85% > 5%

→ WEIBULL NOT REJECTED

(f)

Figure 4.27: Spatial analysis of clutter amplitude between 820 m - 4990 m for the 1st pulse

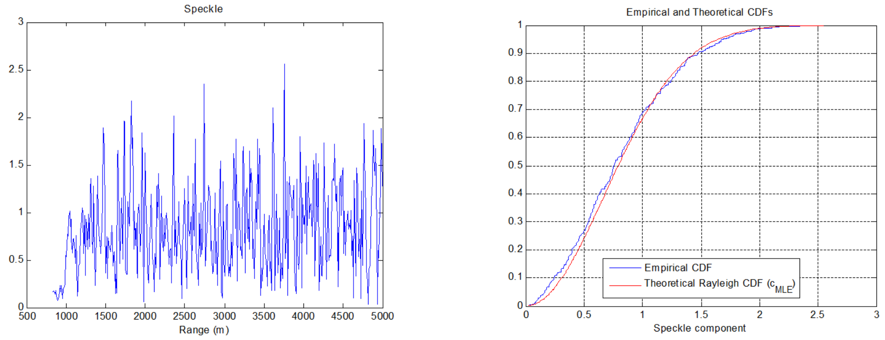

p-value 7.24% > 5%
→ Rayleigh speckle NOT rejected

(a) (b)

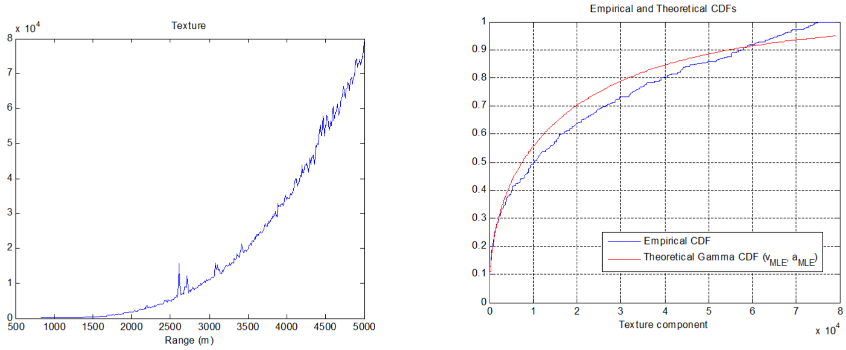

(c)

p-value = 0% < 5%
→ Gamma texture rejected

(d)

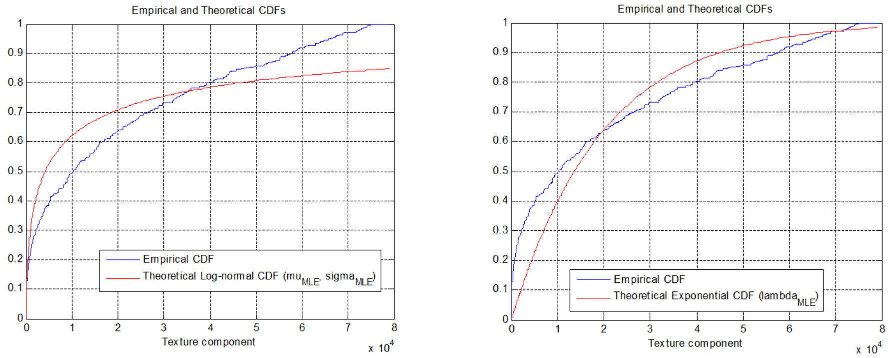

value = 0% < 5%
→ Log-normal texture rejected

(e)

p-value = 0% < 5%
→ Exponential texture rejected

(f)

Figure 4.28: Space - time compound analysis of clutter amplitude between 820 m - 4990 m for the 1st pulse

The window sizes of 250 m, 500 m and 1 km are used for the second illumination area. The results are shown in Figure 4.29-4.31. Again, as the window size decreases, more rapid changes in the scale and shape parameters are observed. Also, for some windows for which Weibull is rejected, Log-normal may be proposed.

For the window length of 500 m, the Weibull shape parameter is found to decrease mainly in three points. A decrease in the shape parameter of Weibull means an increase in the variance. Hence, it can be said that these transitions occur due to a spatial heterogeneity in that region. However, as opposed to the Terrain - 1 results, the Weibull may still be accepted although the shape parameter decreases.

However, the main difference between the results of Terrain-1 and Terrain-2 is that the Log-normal is rejected more than Weibull for the latter. The lower grazing angle in the first terrain, together with the point scatterers such as high buildings, is expected to yield a variance higher than that of the second terrain for which the grazing angle is relatively high. Hence, the Log-normal, with its heavier tails than Weibull, may be more suitable to model Terrain-1. This result seems to be consistent with a previous study on ground clutter [13], in which Log-normal is found to model the clutter amplitude for low-grazing angles, while high-grazing angle clutter is modeled with Weibull. Also, in [32], a region with building blocks is found to be modeled better with Log-normal distribution.

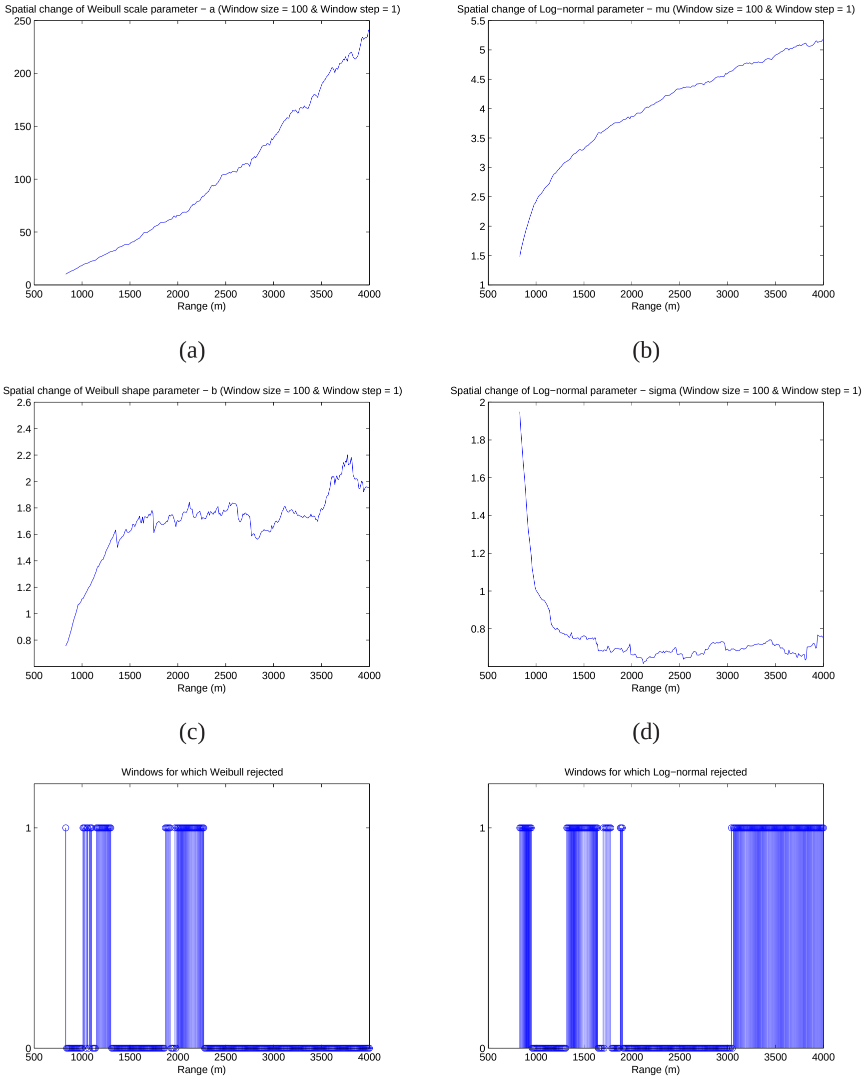

(a) (b)

(c) (d)

(e) (f)

Figure 4.29: Spatial changes of the shape and scale parameters of Weibull and Log-normal distributions for the 1st pulse (Window size = 100)

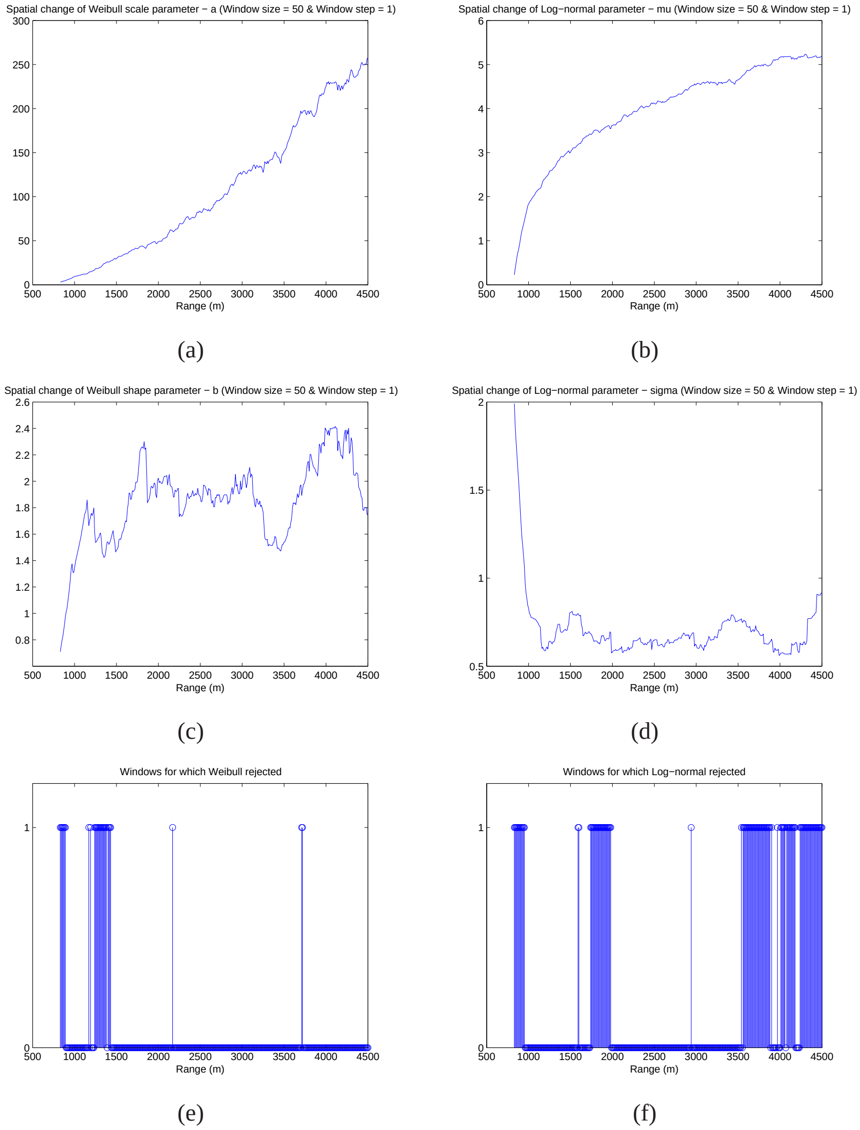

(a) (b) (c) (d) (e) (f)

Figure 4.30: Spatial changes of the shape and scale parameters of Weibull and Log-normal distributions for the 1st pulse (Window size = 50)

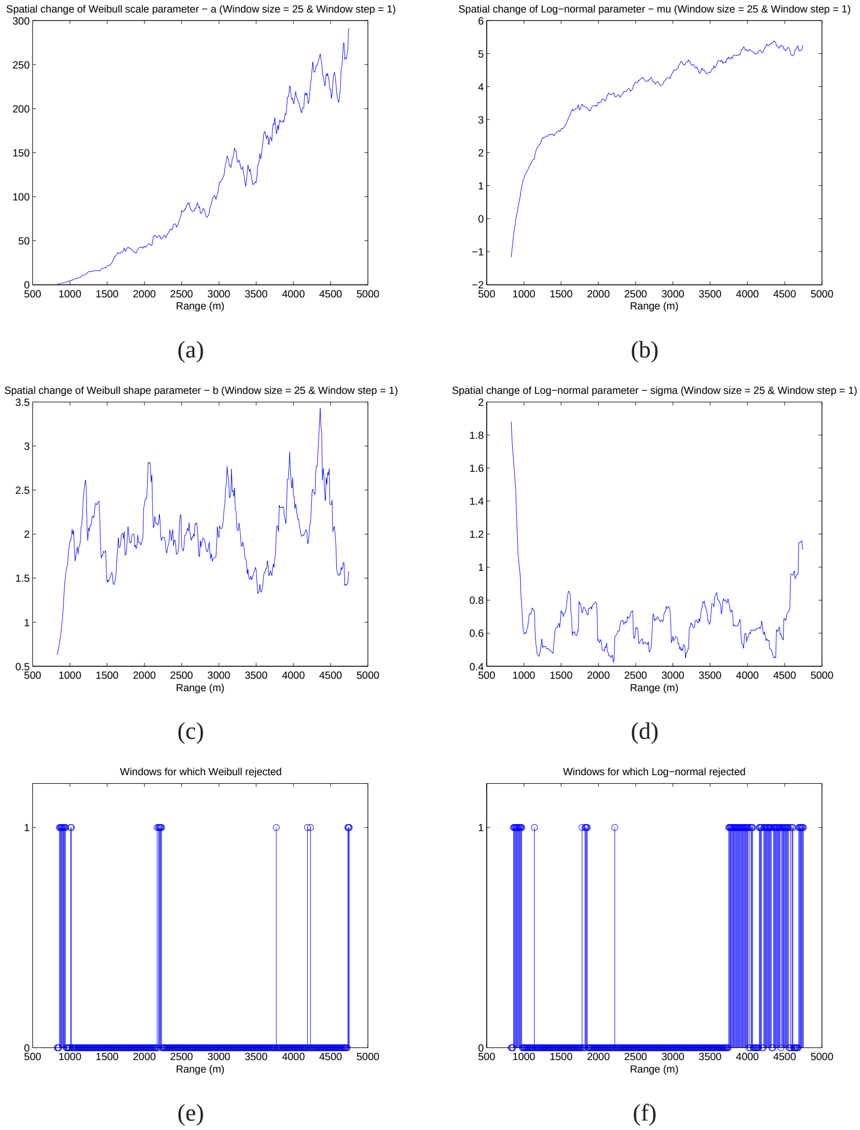

(a) (b)

(c) (d)

(e) (f)

Figure 4.31: Spatial changes of the shape and scale parameters of Weibull and Log-normal distributions for the 1st pulse (Window size = 25)

4.2.4 Surface Clutter Reflectivity for Terrain - 2

In this section, the clutter RCS and reflectivity are calculated for the range interval of 820 m - 4990 m.

The required parameters are the same as Terrain-1 (Table 4.8), except for the grazing angle. The grazing angle for this range interval is assumed to be 10°.

The resulting clutter RCS and clutter reflectivity for Terrain - 2 are presented in Figure 4.32(b) and Figure 4.32(d), respectively. From these figures, it can be seen that the surface reflectivity of Terrain-2 is smaller than that of Terrain-1. Considering the characteristics of the terrains, this is an expected result since Terrain-1 is mostly filled with high buildings as opposed to Terrain-2 which is composed of relatively diffuse components [33].

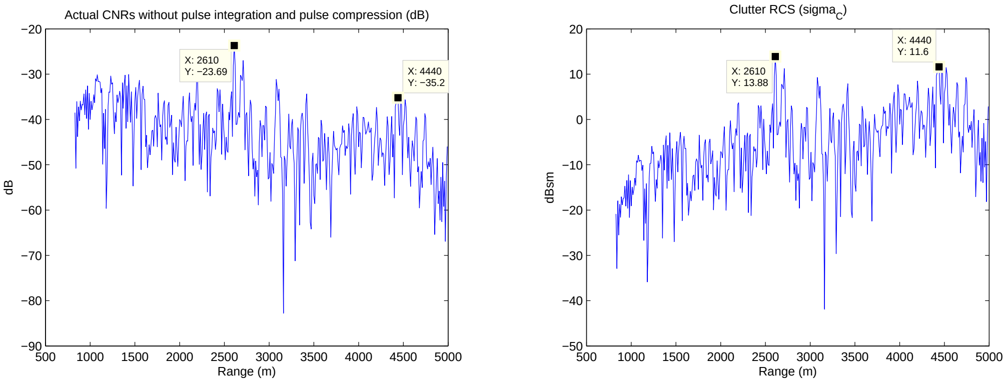

(a) Actual CNRs without improvement factors

(b) Clutter RCS

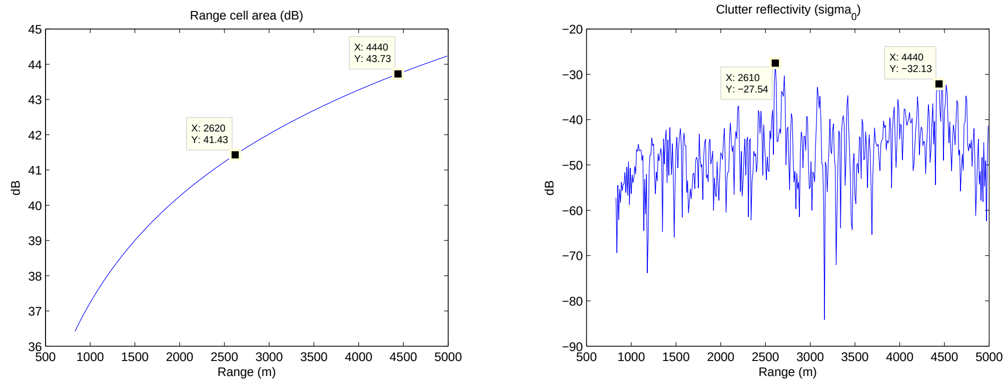

(c) Range cell area

(d) Clutter reflectivity

Figure 4.32: Clutter RCS and reflectivity for 820 m - 4990 m

CHAPTER 5

CONCLUSION

The performance of radar detection and imaging systems strongly depends on the characteristics of radar clutter. In order to improve the radar signal processing algorithms, successful analysis and modeling of radar clutter are required. For a successful model of radar clutter, both the spectral and statistical characteristics of the clutter should be revealed.

In this thesis, an experimental radar data acquisition system is established in order to analyze the measured radar clutter. The limitations of the system due to the specifications of COTS test equipments are determined and the system parameters are optimized accordingly. Finally, the hardware and the data processing system are verified using generic signals.

Next, two different terrains are illuminated with 40-chip P4 coded pulses at 10 GHz. A total time record length of 266 msec is achieved at 20 m range resolution. The recorded data are examined after the construction of a data matrix. The results are interpreted in the light of the characteristics of the illuminated terrains. For both terrains, the first range cells are filled with trees. The first terrain is rather flat with point scatterers such as buildings with various heights rising at various ranges. On the other hand, the second terrain is rugged with small trees and small buildings on it and near the horizon, high buildings rises. The grazing angle for the second terrain is greater than that of the first terrain.

First, the range-Doppler processing is performed for both terrains. In the power vs. range plots, the horizon line can easily be observed. The peaks in the range characteristics also seem to be consistent with the ranges of the scatterers in the illuminated terrains. However, considering the wide azimuthal beamwidth of the antenna, the comments cannot go beyond predictions. On the other hand, some Doppler spread is observed at the first ranges which are covered mostly with trees.

For detailed spectral analyses, the PSD of clutter is estimated for different range cells. Considering the trade-off between the resolution and variance of the PSD estimate, various non-parametric methods are applied. PSD estimates obtained with periodogram, modified periodogram and Welch methods are analyzed. In order to improve the PSD estimate averaging over different records is performed. As a result, for the range cells with trees, the Doppler velocity is found to spread up to 0.45 m/s at power levels 40-50 dB below the zero-Doppler peak under light air condition. For a carrier frequency of 10 GHz, it corresponds to a Doppler spread of 30 Hz.

Then, the statistical analyses in time and space are performed, and by means of complementary empirical fitting methods, the empirical data are tried to fit various theoretical distributions proposed in the literature to model clutter. ML estimates of the distribution parameters obtained from the data are used for the theoretical model that is to be fitted. As the GoF test, the modified KS test with the extension of Monte Carlo approach is used with a significance level of $\alpha = 0.05$. For Gaussianity check of the I/Q data, skewness and kurtosis values are used and the Lilliefors test is applied again with $\alpha = 0.05$.

From the temporal statistical analysis, the I/Q data from both terrains are found to be successfully modeled with Gaussian distribution independent of the number of pulses analyzed. However, as opposed to the second terrain, Rayleigh distribution is rejected to model the clutter amplitude of the first terrain, possibly due to the non-zero mean of the Gaussian I/Q data for the range cells with a dominant scatterer in them. Instead, the Ricean distribution is expected to model the temporal clutter of the first terrain.

As the spatial model, Rayleigh, Log-normal and Weibull distributions are checked for the clutter amplitude at different pulses. Among them, Rayleigh is rejected as expected for the systems with high resolution. Log-normal is also not accepted for both terrains. On the other hand, the rejection ratios of Weibull model for the first and the second terrains are found to be 40% and 80%, respectively. Then, it is also hard to conclude that Weibull is an appropriate model for the whole range of both terrains.

Hence, smaller windows of length 1 km, 500 m, 250 m are investigated by sweeping over the range cells. The spatial changes of the Weibull and Log-normal parameters together with the result of the MKS test are assessed for each window length. For the first terrain, Weibull is rejected more than the Log-normal, and vice versa for the second terrain. For both terrains, as the window size decreases, the spatial change of clutter parameters becomes more apparent. Also, the scale parameters are found to be rather related to the power level of the returns while the shape parameters are based on the dispersion of the scatterers in the illuminated terrain. Besides, since a decrease in the Weibull shape parameter corresponds to an increase in the variance, sharp decreases in this parameter may be attributed to spatial heterogeneity of the clutter region, which may be considered as the clutter edges.

Finally, the space-time compound models are examined. The texture and speckle components of the clutter amplitude are extracted. The speckle is found to be successfully modeled with the Rayleigh distribution. However, fit of the texture to any of the Gamma, Log-normal, Weibull and Exponential models could not be achieved.

Considering the results, possible system improvements and future works can be listed as follows:

- The total time record length of the current system is on the order of msec. Hence, it may be increased in order to improve the Doppler resolution further.
- The sampling rate of the receiver should be improved if finer range resolutions are required.
- The low spectral dynamic range should be improved by increasing the transmitter power.
- Antennas with higher directivity may be used if better angular resolution is required for clutter analyses.
- Antenna isolation may be improved so the receiver will not be exposed to high transmitter power coupled into the receiver antenna Then, it will be no more required to remove the first samples coupled into the receiver, thereby enabling the returns from the blind zone to be analyzed.
- A portable system may be implemented so the measurement areas can be diversified. Then, the characteristics of clutter in different sites can be examined. For instance, measurements can be performed near lakes, forests or agricultural fields, etc. and the results may be compared.

- In order to make it possible to take measurements under different weather conditions, necessary modifications should be applied to the system. For instance, the system may be put into a case which will protect it from rain, wind, etc. By this way, the effect of weather on the radar clutter may be observed.

REFERENCES

[1] F. J. Massey, “The Kolmogorov-Smirnov test for goodness of fit,” *Journal of the American Statistical Association*, vol. 46, no. 253, pp. 68-78, March 1951.

[2] H. W. Lilliefors, “On the Kolmogorov-Smirnov test for Normality with mean and variance unknown,” *Journal of the American Statistical Association*, vol. 62, no. 318, pp. 399-402, June 1967.

[3] G. B. Goldstein, “False-alarm regulation in Log-normal and Weibull clutter,” *IEEE Transactions on Aerospace and Electronic Systems*, vol. AES-9, no. 1, pp. 84-92, January 1973.

[4] B. W. Woodruff, A. H. Moore, E. J. Dunne, and R. Cortes, “A modified Kolmogorov-Smirnov test for Weibull distributions with unknown location and scale parameters,” *IEEE Transactions on Reliability*, vol. R-32, no. 2, pp. 209-213, June 1983.

[5] B. W. Woodruff, P. J. Viviano, A. H. Moore, and E. J. Dunne, “Modified goodness-of-fit tests for Gamma distributions with unknown location and scale parameters,” *IEEE Transactions on Reliability*, vol. R-33, no. 3, pp. 241-245, August 1984.

[6] A. Farina, A. Russo, and F. A. Studer, “Coherent radar detection in Log-normal clutter,” *IEE Proceedings-F on Communications, Radar and Signal Processing*, vol. 133, no. 1, pp. 39-53, February 1986.

[7] J. B. Billingsley and J. F. Larrabee, “Measured spectral extent of L- and X-Band radar reflections from wind-blown trees,” Project Report CMT-57, MIT Lincoln Laboratory, 6 February 1987.

[8] H. C. Chan, “Temporal statistics of low-angle ground clutter,” Report no. 1021, Defence Research Establishment Ottawa, December 1989.

[9] M. Sekine and Y. Mao, “Weibull radar clutter,” *IEE Radar, Sonar, Navigation and Avionics Series 3*, London: Peter Peregrinus, 1990.

[10] H. Keutelian, “The Kolmogorov-Smirnov test when parameters are estimated from data,” CDF note 1285, Version 1.0, 30 April 1991.

[11] T. J. Nohara and S. Haykin, “Canadian East Coast radar trials and the K-distribution,” *IEE Proceedings-F on Radar and Signal Processing*, vol. 138, no. 2, pp. 80-88, April 1991.

[12] J. B. Billingsley and J. F. Larrabee, “Multifrequency measurements of radar ground clutter at 42 sites,” Technical Report 916, vol.2, MIT Lincoln Laboratory, 15 November 1991.

[13] K. R. Menon, N. Balakrishnan, M. Janakiraman, and K. Ramchand, “Characterization of fluctuation statistics of radar clutter for Indian terrain,” *IEEE Transactions on Geoscience and Remote Sensing*, vol. 33, no. 2, pp. 317-324, March 1995.

[14] J. B. Billingsley, “Exponential decay in windblown radar ground clutter Doppler spectra: Multifrequency measurements and model,” Technical Report 997, MIT Lincoln Laboratory, 29 July 1996.

[15] A. Farina, F. Gini, M. V. Greco, and L. Verrazzani, “High resolution sea clutter data: Statistical analysis of recorded live data,” *IEE Proceedings - Radar, Sonar and Navigation*, vol. 144, no. 3, pp. 121-130, June 1997.

[16] V. Anastassopoulos, G. A. Lampropoulos, A. Drosopoulos, and M. Rey, “High resolution radar clutter statistics,” *IEEE Transactions on Aerospace and Electronic Systems*, vol. 35, no. 1, pp. 43-60, January 1999.

[17] J. B. Billingsley, A. Farina, F. Gini, M. V. Greco, and L. Verrazzani, “Statistical analyses of measured radar ground clutter data,” *IEEE Transactions on Aerospace and Electronic Systems*, vol. 35, no. 2, pp. 579-593, April 1999.

[18] F. E. Nathanson, J. P. Reilly, and M. N Cohen, “Radar Design Principles,” New Jersey: SciTech, 2nd ed., 1999.

[19] M. Greco, F. Gini, A. Farina, and J. B. Billingsley, “Validation of windblown radar ground clutter spectral shape,” *IEEE Transactions on Aerospace and Electronic Systems*, vol. 37, no. 2, pp. 538-548, April 2001.

[20] D. Blacknell and R. J. A. Tough, “Parameter estimation for the K-distribution based on [z log(z)],” *IEE Proceedings - Radar, Sonar and Navigation*, vol. 148, no. 6, pp. 309-312, December 2001.

[21] M. W. Long, “Radar reflectivity of land and sea,” 3rd ed., 2001.

[22] E. Radoi, A. Quinquis, and P. Saulais, “Analysis and simulation of sea clutter at high range resolution and low grazing angles,” *IEEE International Geoscience and Remote Sensing Symposium 2003*, vol. 7, no., pp. 4192-4194, 21-25 July 2003.

[23] G. Davidson, H. D. Griffiths, and S. Ablett, “Analysis of high-resolution land clutter,” *IEEE Proceedings - Vision, Image and Signal Processing*, vol. 151, no. 1, pp. 86-91, 5 February 2004.

[24] E. E. Kuruoglu and J. Zerubia, “Modeling SAR images with a generalization of the Rayleigh distribution,” *IEEE Transactions on Image Processing*, vol. 13, no. 4, pp. 527-533, April 2004.

[25] M. A. Richards, “Fundamentals of radar signal processing,” New York: McGraw-Hill, 2005.

[26] P. Stoica and R. L. Moses, “Spectral analysis of signals,” New Jersey: Prentice Hall, 2005.

[27] K. D. Ward, R. J. A. Tough, and S. Watts, “Sea clutter: Scattering, the K distribution and radar performance,” *IET Radar, Sonar and Navigation Series 20*, London: IET, 2006.

[28] M. S. Greco and F. Gini, “Statistical analysis of high-resolution SAR ground clutter data,” *IEEE Transactions on Geoscience and Remote Sensing*, vol. 45, no. 3, pp. 566-575, March 2007.

[29] U. C. Doyuran and Y. Tanik, “Detection in range-heterogeneous Weibull clutter,” *IEEE Radar Conference 2007*, vol., no., pp. 343-347, 17-20 April 2007.

[30] P. Wellig, K. Schmid, H. Essen, A. Kurz, H. Schimpf, and T. Brehm, “Clutter analysis of high resolution millimeter-wave SAR-data in the spatial and wavelet domain,” *IEEE International Geoscience and Remote Sensing Symposium 2007*, vol., no., pp. 559-562, 23-28 July 2007.

[31] S. Watts, “Radar sea clutter modelling and simulation - Recent progress and future challenges,” *IET Seminar on Radar Clutter Modelling 2008*, vol., no., pp. 1-7, 19 February 2008.

[32] L. Zhu, Z. M. Chen, and C. S. Jiang, “Amplitude statistical analysis of Ku-band SAR ground clutter data,” *International Conference on Communications, Circuits and Systems 2008*, vol., no., pp. 866-870, 25-27 May 2008.

[33] M. I. Skolnik, “Radar Handbook,” McGraw Hill, 3rd ed., 2008.

[34] A. C. Hamurcu and A. Hizal, “CA-CFAR detection in spatially correlated K-distributed sea clutter,” *IEEE 17th Signal Processing and Communications Applications Conference*, vol., no., pp. 840-843, 9-11 April 2009.

[35] D. J. Crisp, L. Rosenberg, N. J. Stacy, and Y. Dong, “Modelling X-band sea clutter with the K-distribution: Shape parameter variation,” *International Radar Conference - Surveillance for a Safer World 2009*, vol., no., pp. 1-6, 12-16 October 2009.

[36] X. W. Xing, Z. L. Chen, H. X. Zou, and S.L. Zhou, “A fast algorithm based on two-stage CFAR for detecting ships in SAR images,” *2nd Asian-Pacific Conference on Synthetic Aperture Radar 2009*, vol., no., pp. 506-509, 26-30 October 2009.

[37] N. Kilicoglu, “Construction of an experimental radar system,” December 2010.

[38] “Agilent E8267D PSG Vector Signal Generator Data Sheet,” 5989-0697EN, 28 July 2008.

[39] “HP8348A Microwave Amplifier Data Sheet”

[40] “AML218L1502 Low Noise Amplifier Data Sheet”

[41] “Agilent E4446A PSA Spectrum Analyzer Data Sheet,” 5980-1284E, 11 August 2008.

[42] “Agilent E4446A PSA Spectrum Analyzer Specifications Guide,” E4440-90606, June 2008.

[43] “Agilent 89600 Vector Signal Analysis Software Data Sheet,” 5989-1786EN, 20 April 2010.

[44] “Agilent N9010A EXA Signal Analyzer Data Sheet,” 5989-6529EN, 19 April 2010.

[45] “Agilent N9010A EXA Signal Analyzer Specifications Guide,” N9010-90025, August 2010.

[46] “Agilent IQ Modulation Considerations for PSG Vector Signal Generators,” 5989-7057EN, 24 July 2007.

Appendix A

NEYMAN-PEARSON CRITERION

Problem Definition: Maximize the probability of detection P_D under the constraint that the probability of false alarm P_{FA} does not exceed some tolerable value α. That is,

chose $\Re_1$ such that P_D is maximized, subject to $P_{FA} \leq \alpha$.

In order to solve this optimization problem, the method of Lagrange multipliers is used:

$$F \equiv P_D + \lambda \left(P_{FA} - \alpha \right). \tag{A.1}$$

To find the optimum solution for the design variable $\Re_1$, F is maximized and then λ satisfying the constraint $P_{FA} = \alpha$ is chosen.

If P_D and P_{FA} are expressed as

$$P_D = \int_{\Re_1} p_{\mathbf{y}} \left(\mathbf{y} \mid H_1 \right) \, \mathbf{dy} \tag{A.2a}$$

$$P_{FA} = \int_{\Re_1} p_{\mathbf{y}} \left(\mathbf{y} \mid H_0 \right) \, \mathbf{dy}. \tag{A.2b}$$

then, the function F can be written as follows

$$
\begin{aligned}
F &= \int_{\mathfrak{R}_1} p_{\mathbf{y}}\left(\mathbf{y} \mid H_1\right)\, \mathbf{dy} + \lambda\left(\int_{\mathfrak{R}_1} p_{\mathbf{y}}\left(\mathbf{y} \mid H_0\right)\, \mathbf{dy} - \alpha\right) \\
&= -\lambda\alpha + \int_{\mathfrak{R}_1} \left\{p_{\mathbf{y}}\left(\mathbf{y} \mid H_1\right) + \lambda p_{\mathbf{y}}\left(\mathbf{y} \mid H_0\right)\right\} \mathbf{dy}
\end{aligned}
\tag{A.3}
$$

The first term in (A.3) is independent of $\mathfrak{R}_1$. Hence, the second term is maximized in order to maximize F. The integrand of the second term can be either positive or negative depending on the values of λ, $p_{\mathbf{y}}\left(\mathbf{y} \mid H_1\right)$, and $p_{\mathbf{y}}\left(\mathbf{y} \mid H_0\right)$. Thus, the integral is maximized by assigning all the points $\mathbf{y}$ in the N dimensional space for which

$$
p_{\mathbf{y}}\left(\mathbf{y} \mid H_1\right) + \lambda p_{\mathbf{y}}\left(\mathbf{y} \mid H_0\right) > 0 \tag{A.4}
$$

to the region $\mathfrak{R}_1$.

Then, the decision rule is found to be as

$$
\frac{p_{\mathbf{y}}\left(\mathbf{y} \mid H_1\right)}{p_{\mathbf{y}}\left(\mathbf{y} \mid H_0\right)} \gtrless_{H_0}^{H_1} \gamma \tag{A.5}
$$

where $\gamma = -\lambda$.

Appendix B

HYPOTHESIS TEST TERMINOLOGY

Null hypothesis, H_0: The hypothesis that is to be tested.

Alternative hypothesis, H_A: The hypothesis that is to be accepted when the null hypothesis is rejected.

Type-I error (False positive): The error of rejecting the null hypothesis when it is actually true.

Type-II error (False negative): The error of failing to reject the null hypothesis when it is not true.

Test statistic: A quantity calculated from the data sample. The decision whether to accept or reject the null hypothesis is based on this statistic.

Critical value: The threshold to which the test statistic is compared in order to decide whether to reject the null hypothesis or not.

Significance level (or critical p-value), α: The probability of wrongly rejecting the null hypothesis, i.e., the probability of making a Type-I error. A hypothesis test is constructed for a given significance level. A typical value for α is 0.05.

p-value, p: The probability of getting a value of the test statistic as extreme as or more extreme than that observed by chance alone, if the null hypothesis is true. If the p-value is smaller than the significance level α, the result is said to be *statistically significant*. If the p-value is greater than α, there is insufficient evidence to reject the null hypothesis. (Note that lack of evidence for rejecting the null hypothesis is not evidence for accepting the null hypothesis.)

Statistical significance: A result is said to be statistically significant if it is unlikely to have occurred by chance.

Confidence level: $100(1-\alpha)\%$

Appendix C

SOME NOTES ON THE MEASUREMENT EQUIPMENTS

C.1 PULSE/RF Blanking Function of VSG

ALC hold function is also enabled by PULSE/RF blanking. If ALC hold is on, it samples the IQ waveform only where the marker waveform is defined, and uses the average of the sampled waveform to set the ALC circuitry. For a pulsed signal, the marker waveform is on during the on samples of the pulse. However, if ALC hold is off, the whole signal is taken into account. Hence, the average seems to be lower than actual value due to the off samples. Then, the ALC circuitry tries to increase the average further although it is not required. This results in an erroneous DC-like component on the whole signal.

In order to exemplify this situation, the VSG and PSA are connected directly to each other without antennas in between. A 100-chip P4-coded pulse of 10 usec PW and 100 usec PRI is transmitted. In the following plots for no RF blanking, the DC-like component can be easily observed.

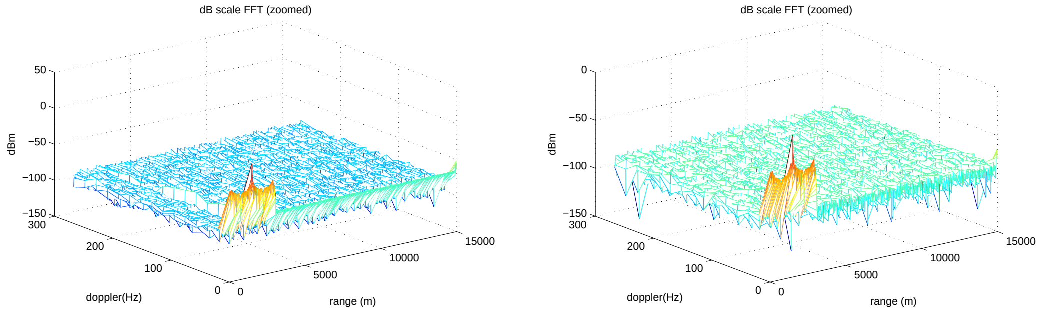

(a) RF blanking OFF (original view)

(b) RF blanking ON (original view)

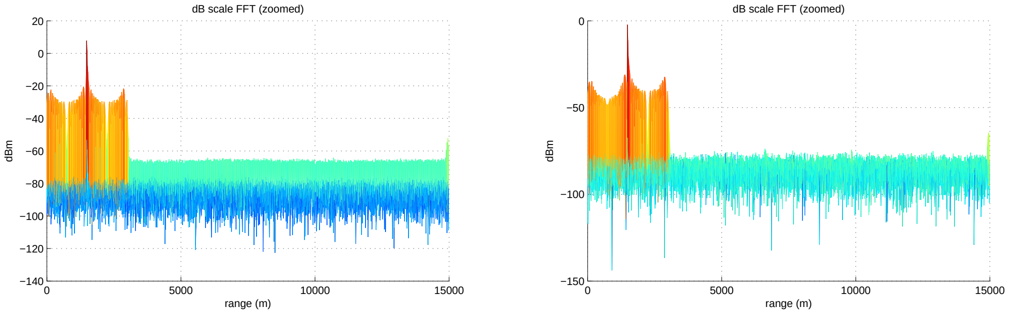

(c) RF blanking OFF (Power vs. range)

(d) RF blanking ON (Power vs. range)

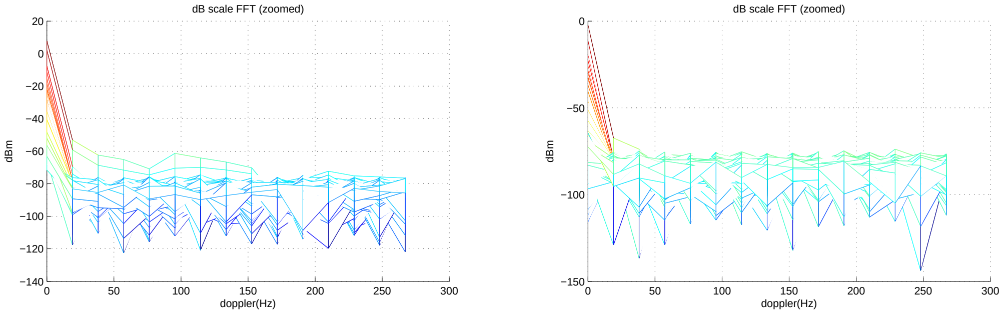

(e) RF blanking OFF (Power vs. Doppler freq)

(f) RFblanking ON (Power vs. Doppler freq)

Figure C.1: Effect of PULSE/RF blanking function of VSG

C.2 Input Range Selection of VSA

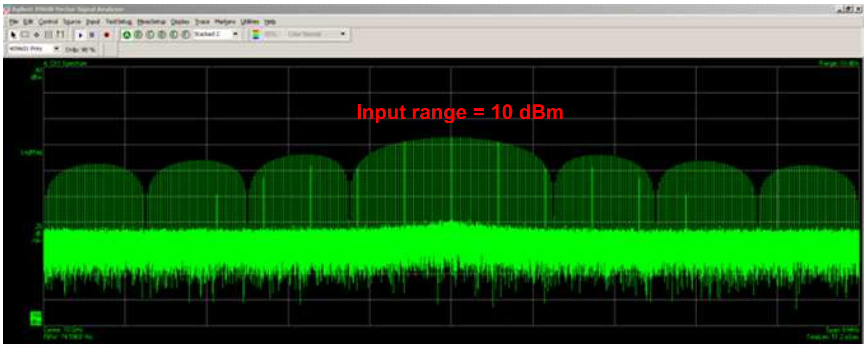

(a) Input range = 10 dBm

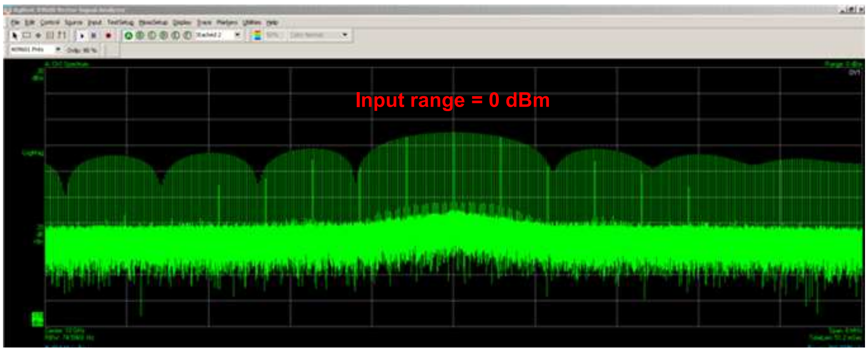

(b) Input range = 0 dBm

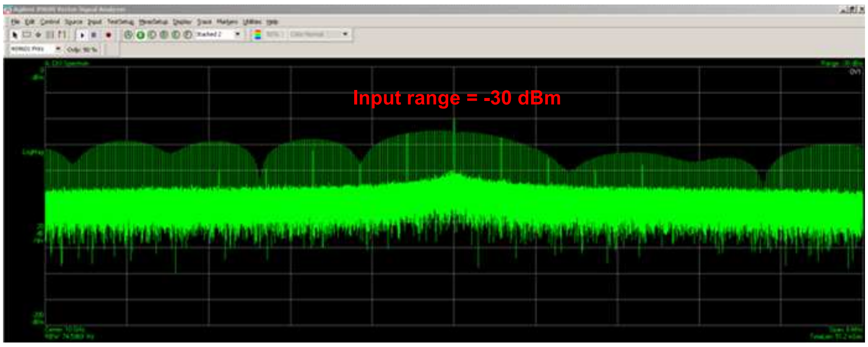

(c) Input range = -30 dBm

Figure C.2: Effect of the input range selection of VSA

C.3 Noise Level and Noise Figure of PSA Spectrum Analyzer

The noise figure of PSA spectrum analyzer can be calculated from the following formula:

$$\text{NF (dB)} = \text{Noise level normalized to 1Hz RBW (dBm)} - \text{kTB (dBm)} \tag{C.1}$$

where

NF: Noise figure of the spectrum analyzer (dB),
k: Boltzmann's constant (1.38×10^{-23} joules/Kelvin),
T: Temperature (Kelvin),
B: Bandwidth in which the noise is measured (Hz),
RBW: Resolution bandwidth of the spectrum analyzer (Hz).

According to the data sheet of the spectrum analyzer [41], its typical noise level at 10 GHz is -149 dBm (normalized to 1Hz RBW and 0 dB attenuation). This noise level can be directly read by a noise marker as in Figure C.3(a). Then, the noise figure can be calculated as

$$\begin{aligned} \text{NF (dB)} &= \text{Noise level normalized to 1Hz RBW (dBm)} - \text{kTB (dBm)} && \text{(C.2a)} \\ &= \text{-149 dBm} - (10 \cdot \log_{10}(1.38 \cdot 10^{-23} \cdot (25 + 273) \cdot 1) + 30)\ \text{dBm} && \text{(C.2b)} \\ &= 25\ \text{dB}. && \text{(C.2c)} \end{aligned}$$

It is important to note that, if a normal marker is used instead of a noise marker to measure the noise level, the reading differs. In this case, a correction factor of RBW/B should be taken into account in interpreting the noise level reading of a normal marker. Then, (C.1) can be written as

$$\text{NF (dB)} = \text{Measured noise level (dBm)} - \text{kTB (dBm)} - \frac{\text{RBW}}{\text{B}}\text{(dB)} \tag{C.3}$$

where RBW is the resolution bandwidth of the spectrum analyzer (Hz).

For example, when B=1 MHz, T=25°C, RBW=1 Hz, N=25 dB, the measured noise level is found to be -99 dBm. Indeed, the normal marker reads -100 dBm (Figure C.3(b)).

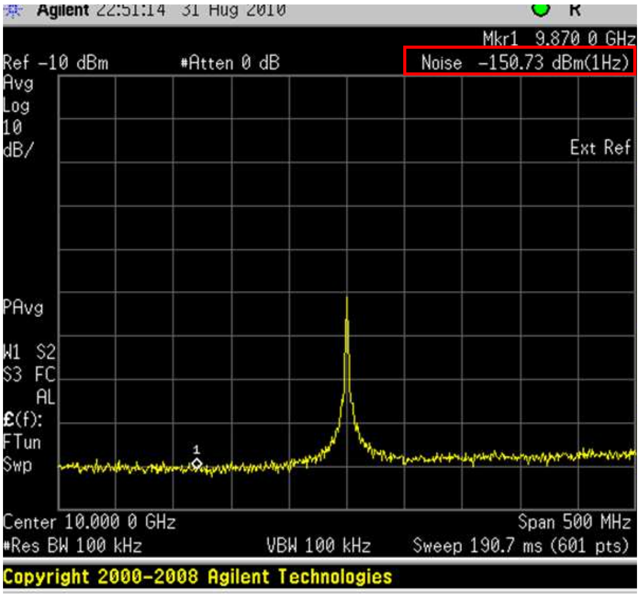

Agilent 22:51:14 31 Aug 2010

Mkr1 9.870 0 GHz

Ref -10 dBm #Atten 0 dB Noise -150.73 dBm(1Hz)

Center 10.000 0 GHz Span 500 MHz

#Res BW 100 kHz VBW 100 kHz Sweep 190.7 ms (601 pts)

(a) By a noise marker

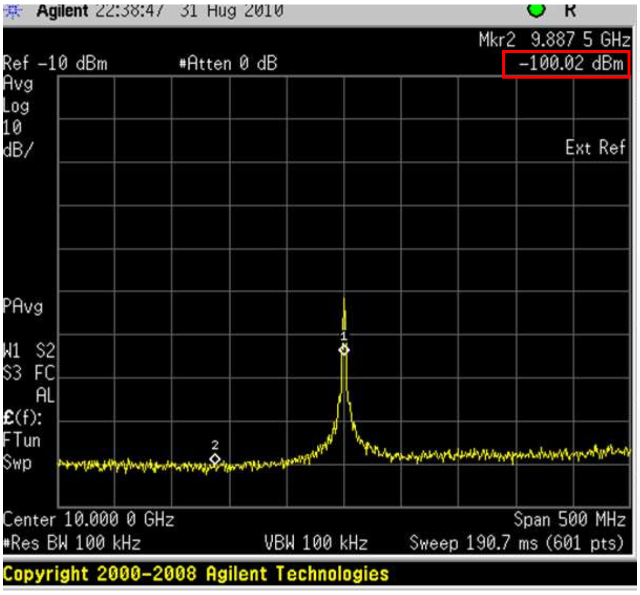

Agilent 22:38:47 31 Aug 2010

Mkr2 9.887 5 GHz

Ref -10 dBm #Atten 0 dB -100.02 dBm

Center 10.000 0 GHz Span 500 MHz

#Res BW 100 kHz VBW 100 kHz Sweep 190.7 ms (601 pts)

(b) By a normal marker

Figure C.3: Noise level readings of the spectrum analyzer

Appendix D

ALTITUDE PROFILES OF THE ILLUMINATED TERRAINS

D.1 Altitude Profiles for Terrain - 1

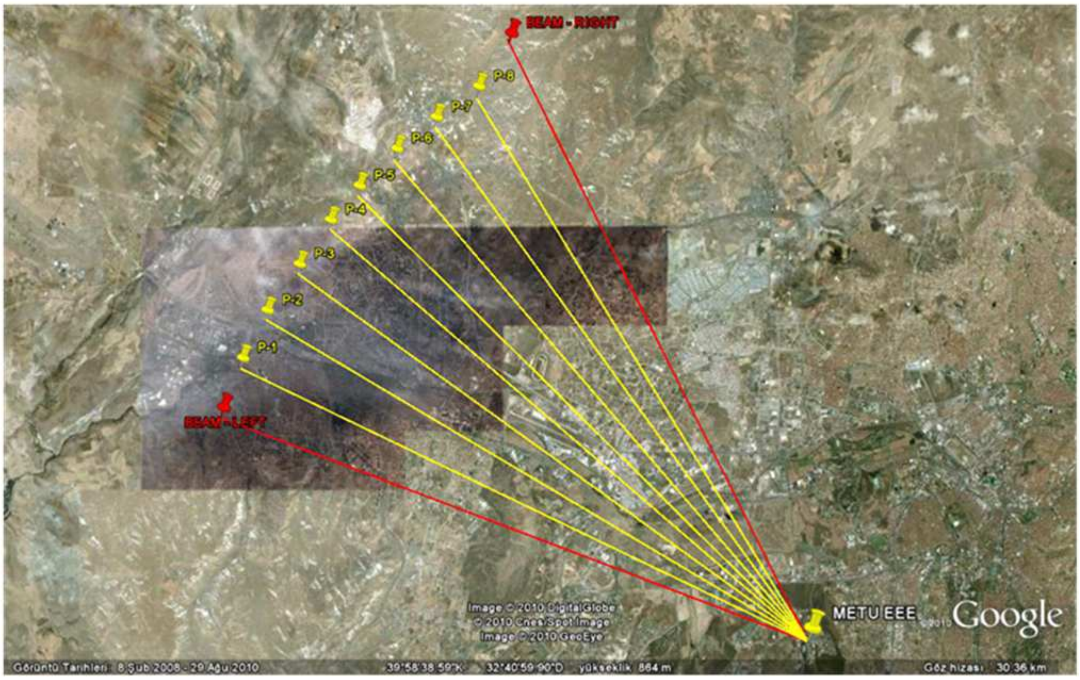

Figure D.1: Antenna beam for Terrain-1

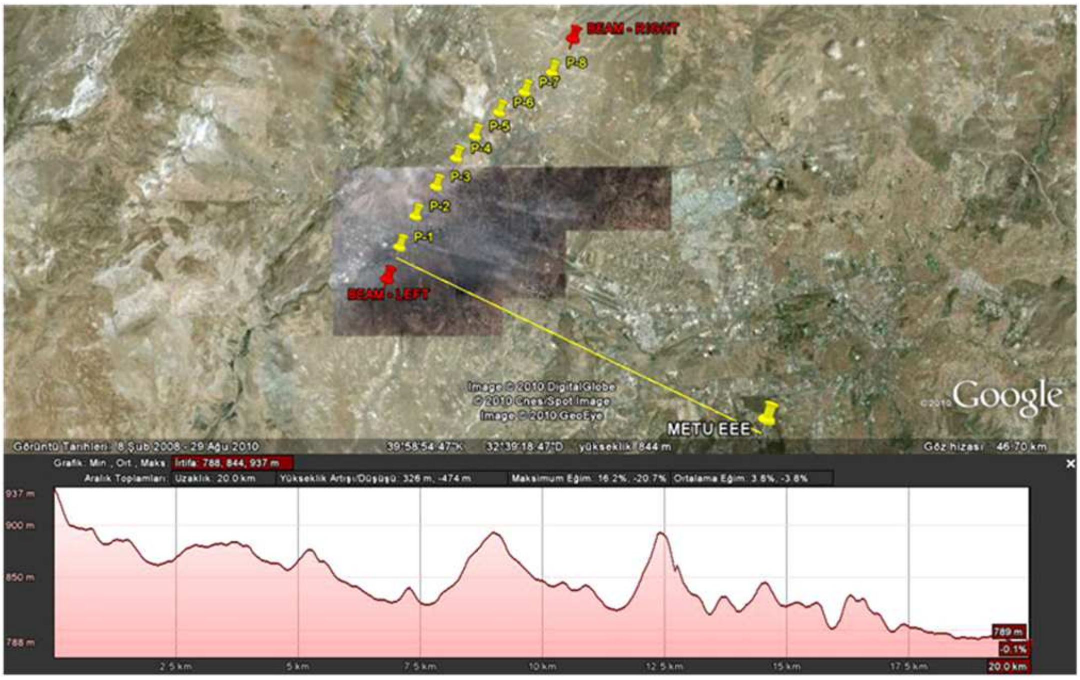

Görüntü Tarihleri: 8 Şub 2008 - 29 Ağu 2010 39°58'54.47"K 32°39'18.47"D yükseklik 844 m Göz hizası 46.70 km

Grafik: Min, Ort, Maks: İrtifa: 788, 844, 937 m

Aralık Toplamları: Uzaklık: 20.0 km Yükseklik Artışı/Düşüşü: 326 m, -474 m Maksimum Eğim: 16.2%, -20.7% Ortalama Eğim: 3.8%, -3.8%

Figure D.2: Altitude profile of Path-1 for Terrain-1

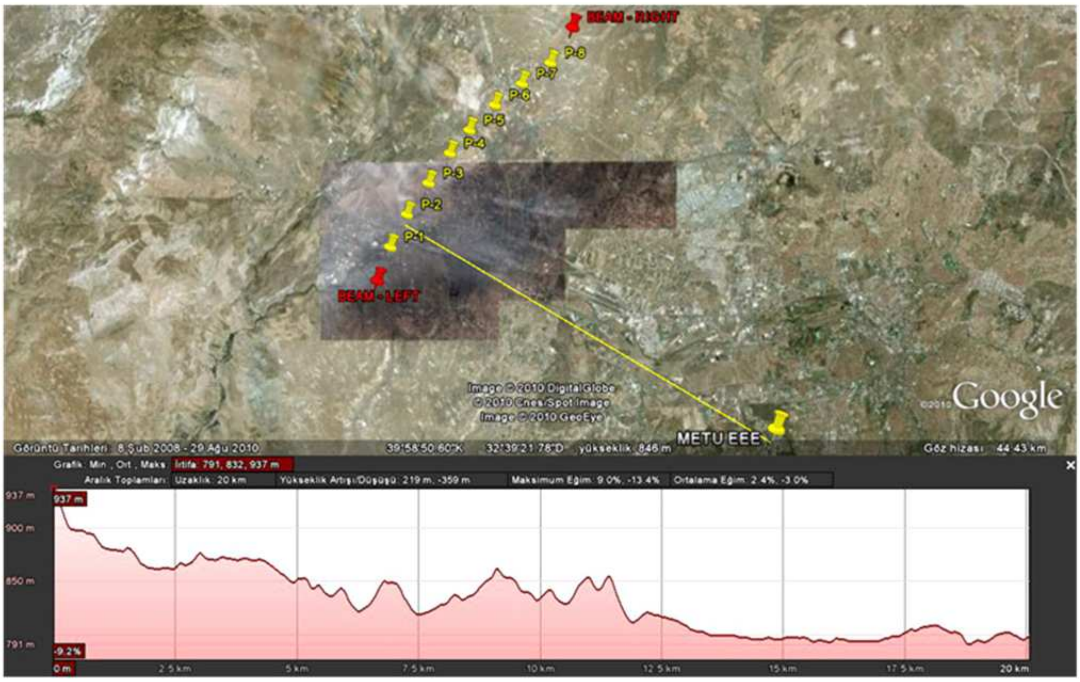

Görüntü Tarihleri: 8 Şub 2008 - 29 Ağu 2010 39°58'50.60"K 32°39'21.78"D yükseklik 846 m Göz hizası 44.43 km

Grafik: Min, Ort, Maks: İrtifa: 791, 832, 937 m

Aralık Toplamları: Uzaklık: 20 km Yükseklik Artışı/Düşüşü: 219 m, -359 m Maksimum Eğim: 9.0%, -13.4% Ortalama Eğim: 2.4%, -3.0%

Figure D.3: Altitude profile of Path-2 for Terrain-1

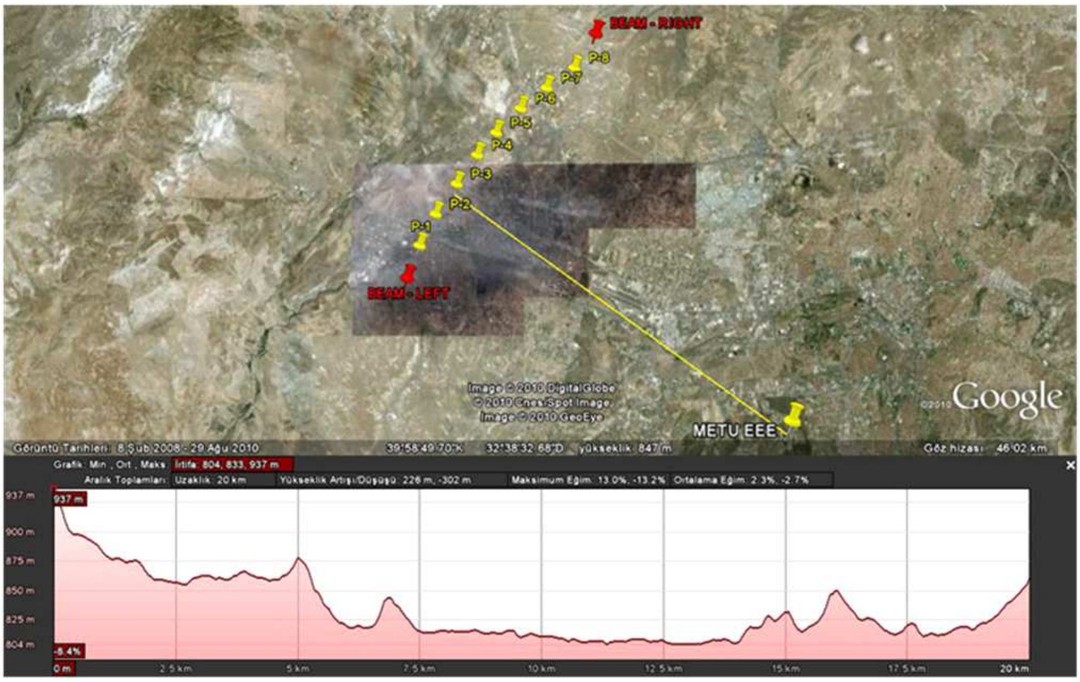

Figure D.4: Altitude profile of Path-3 for Terrain-1

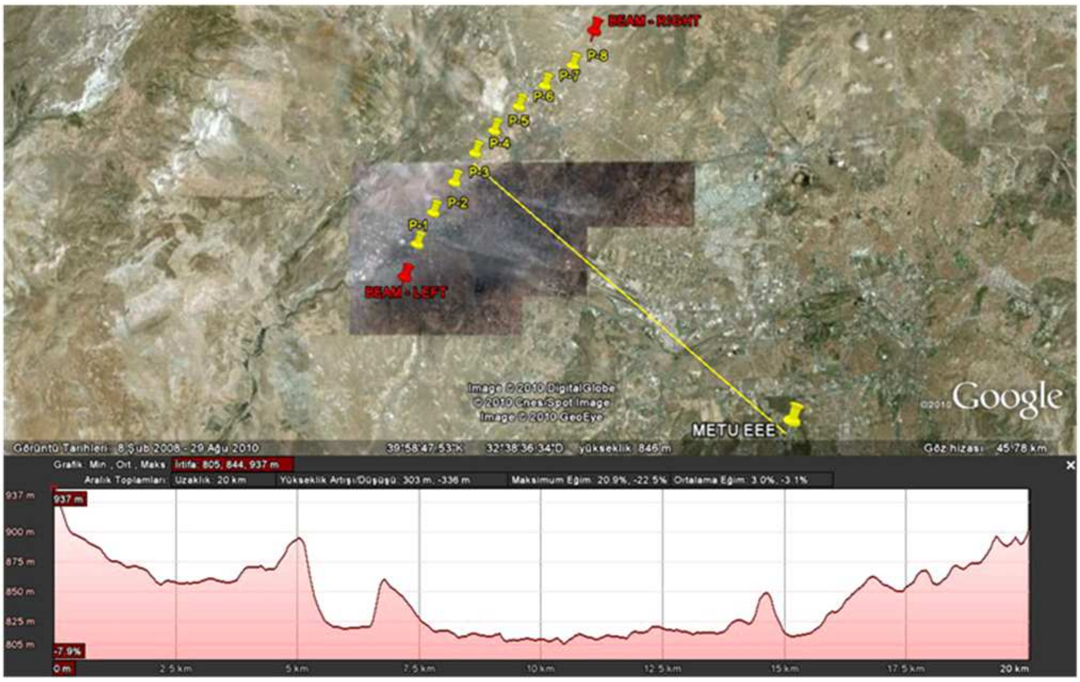

Figure D.5: Altitude profile of Path-4 for Terrain-1

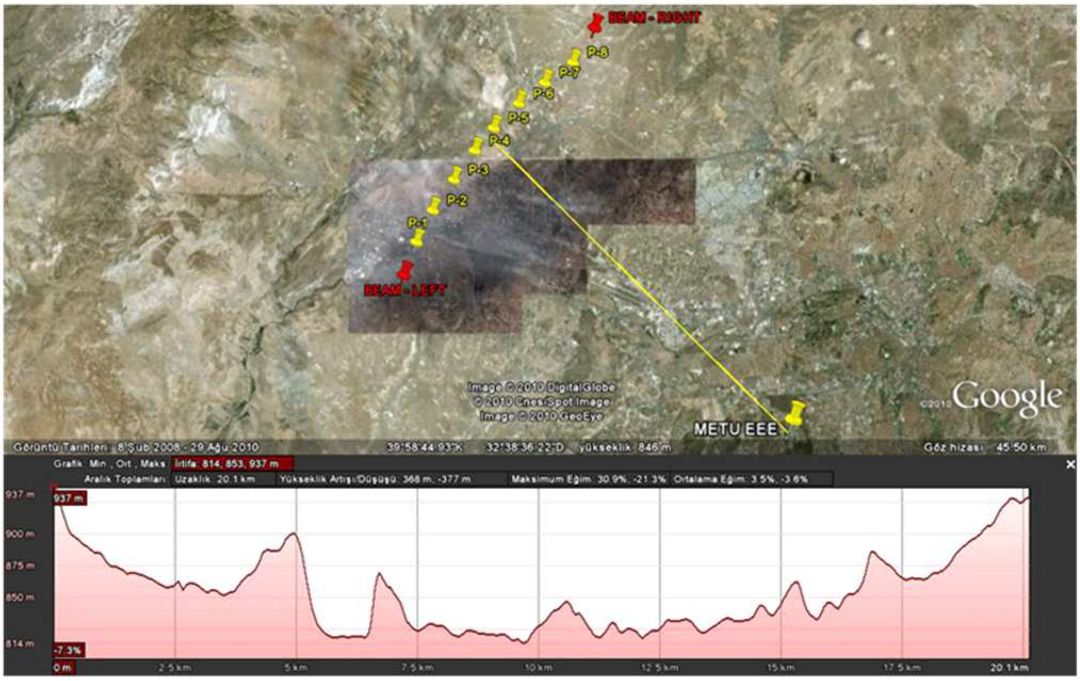

Figure D.6: Altitude profile of Path-5 for Terrain-1

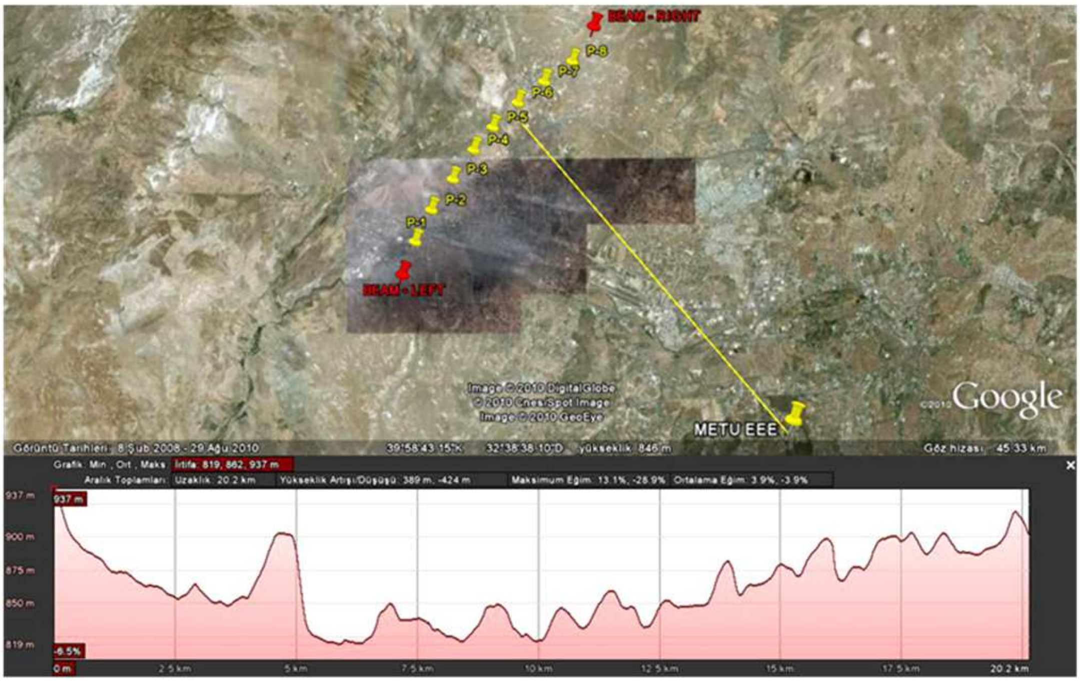

Figure D.7: Altitude profile of Path-6 for Terrain-1

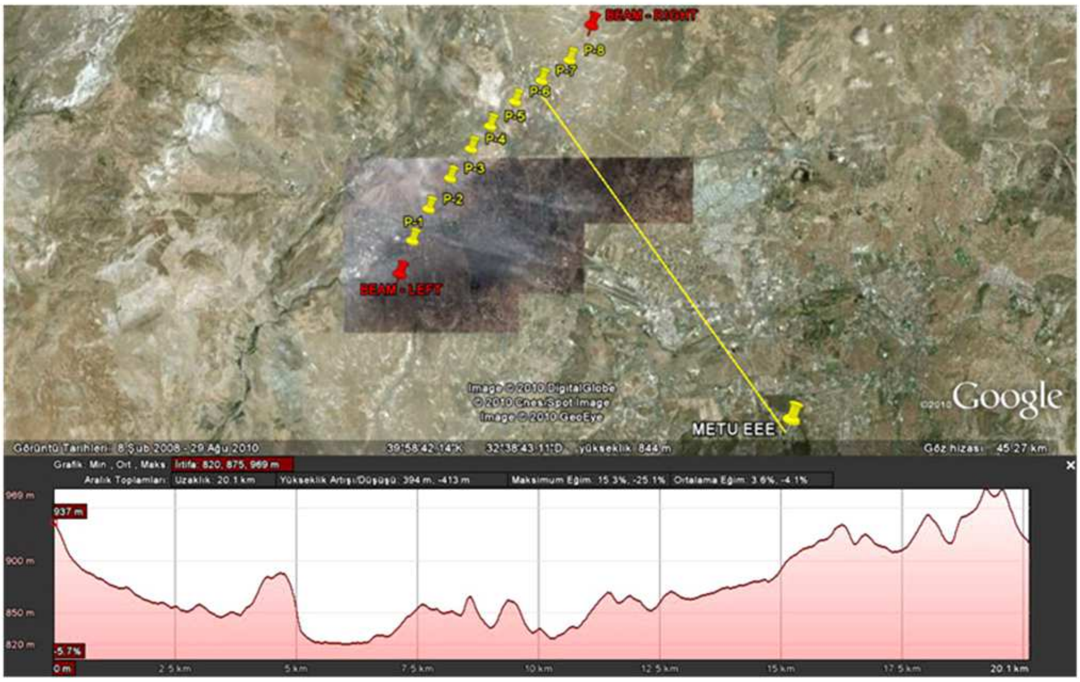

Figure D.8: Altitude profile of Path-7 for Terrain-1

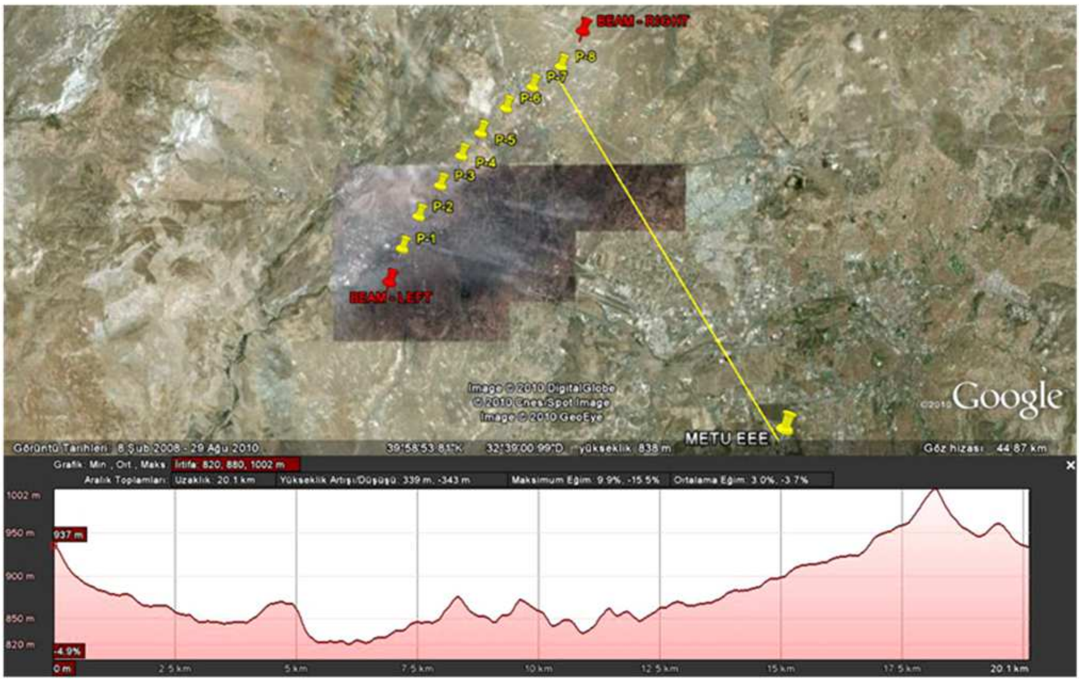

Figure D.9: Altitude profile of Path-8 for Terrain-1

D.2 Altitude Profiles for Terrain - 2

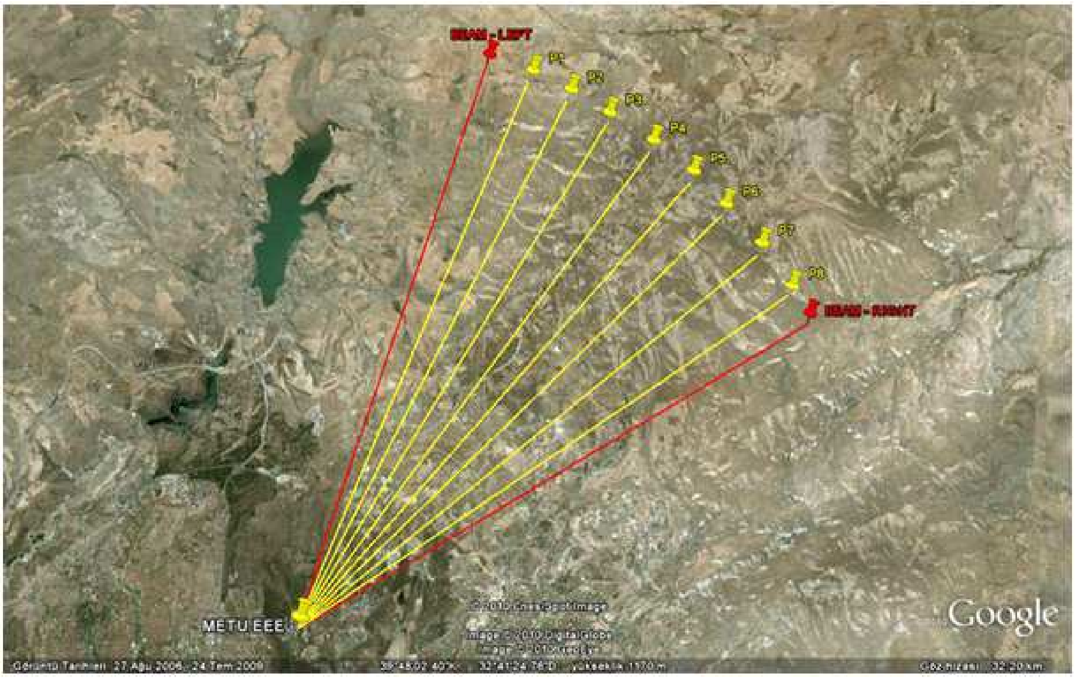

Figure D.10: Antenna beam for Terrain-2

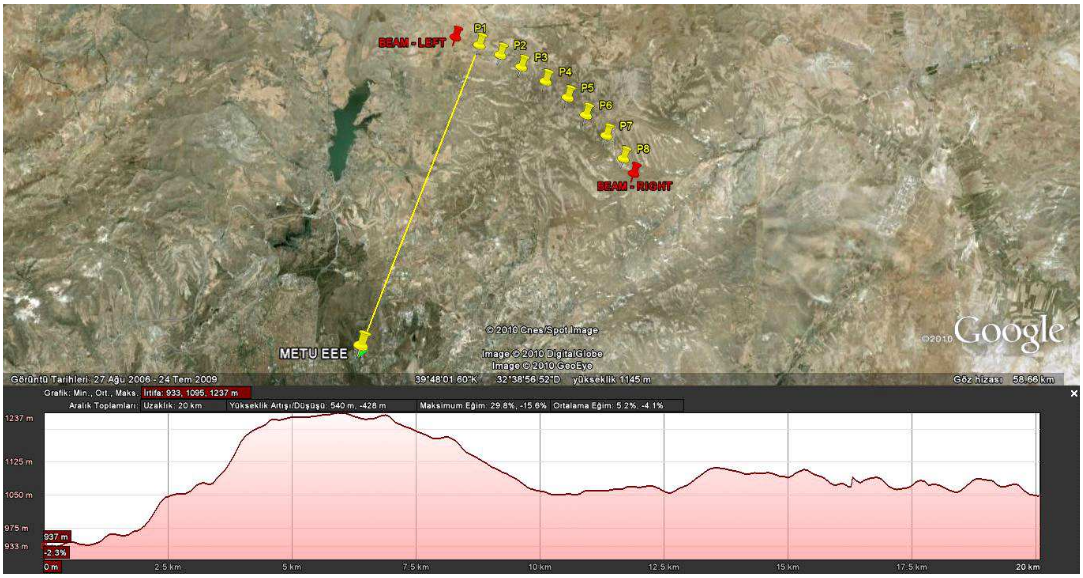

Figure D.11: Altitude profile of Path-1 for Terrain-2

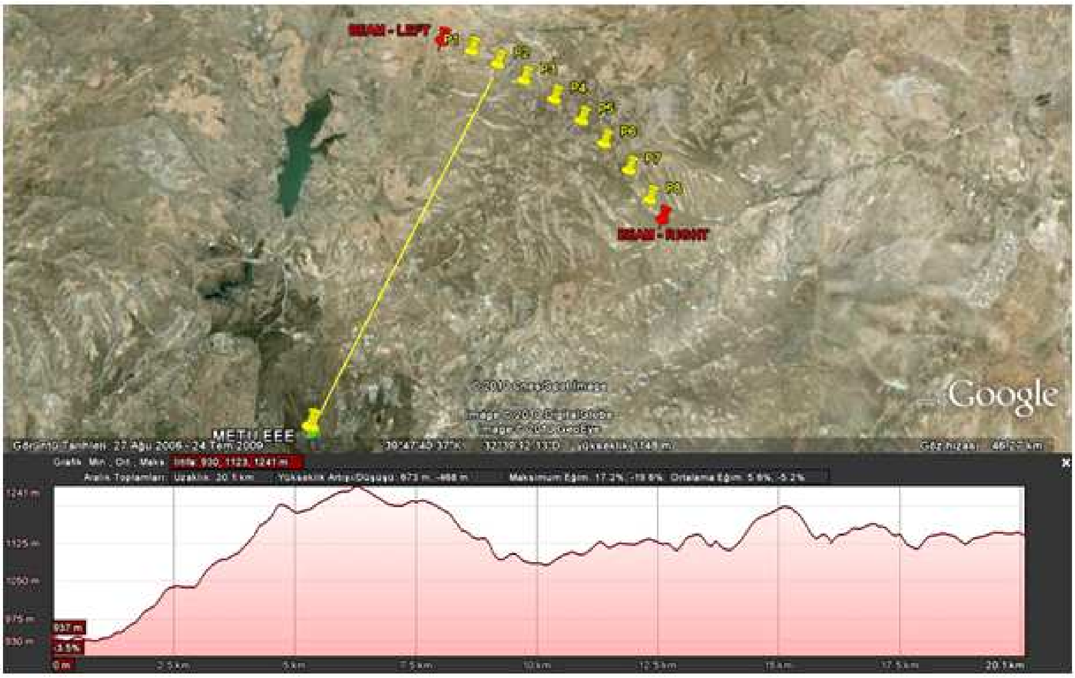

Figure D.12: Altitude profile of Path-2 for Terrain-2

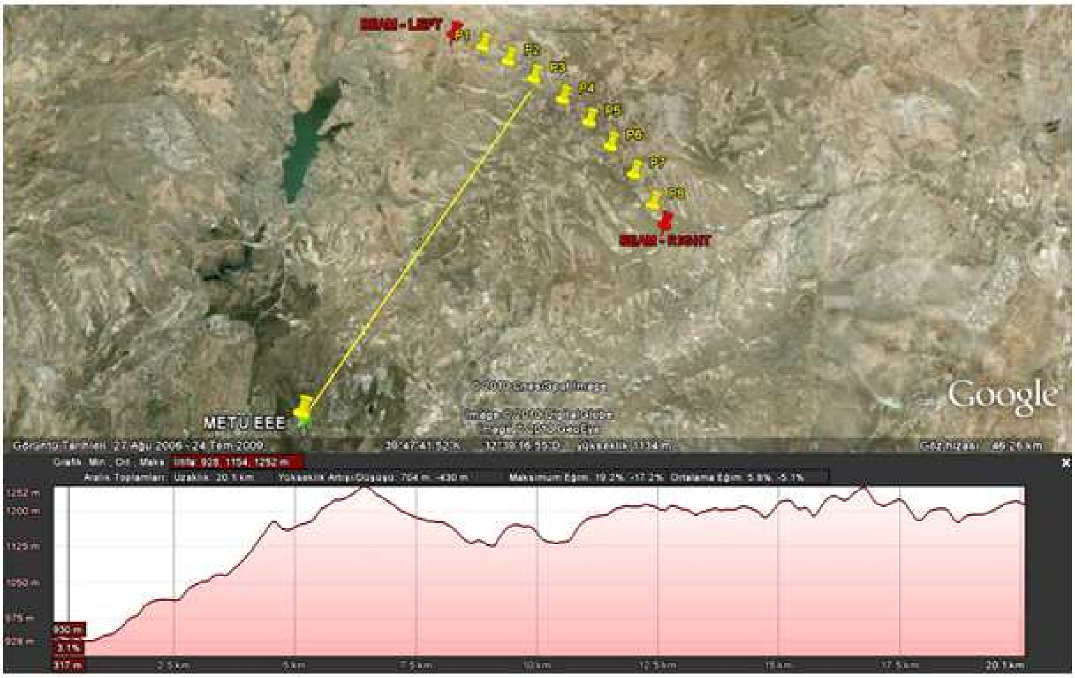

Figure D.13: Altitude profile of Path-3 for Terrain-2

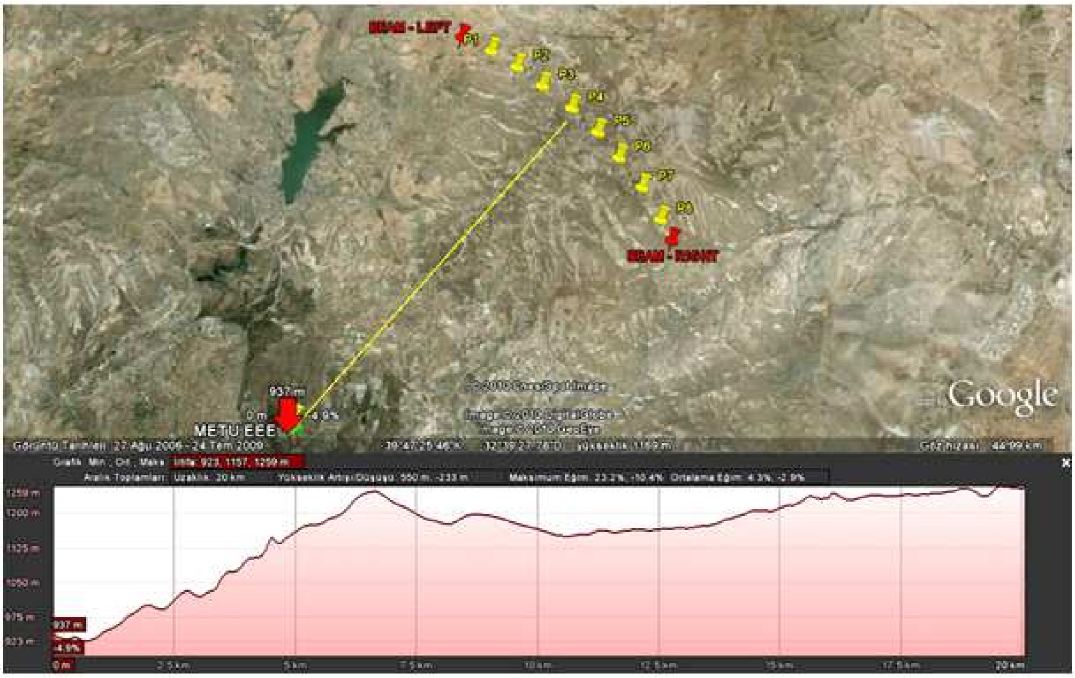

Figure D.14: Altitude profile of Path-4 for Terrain-2

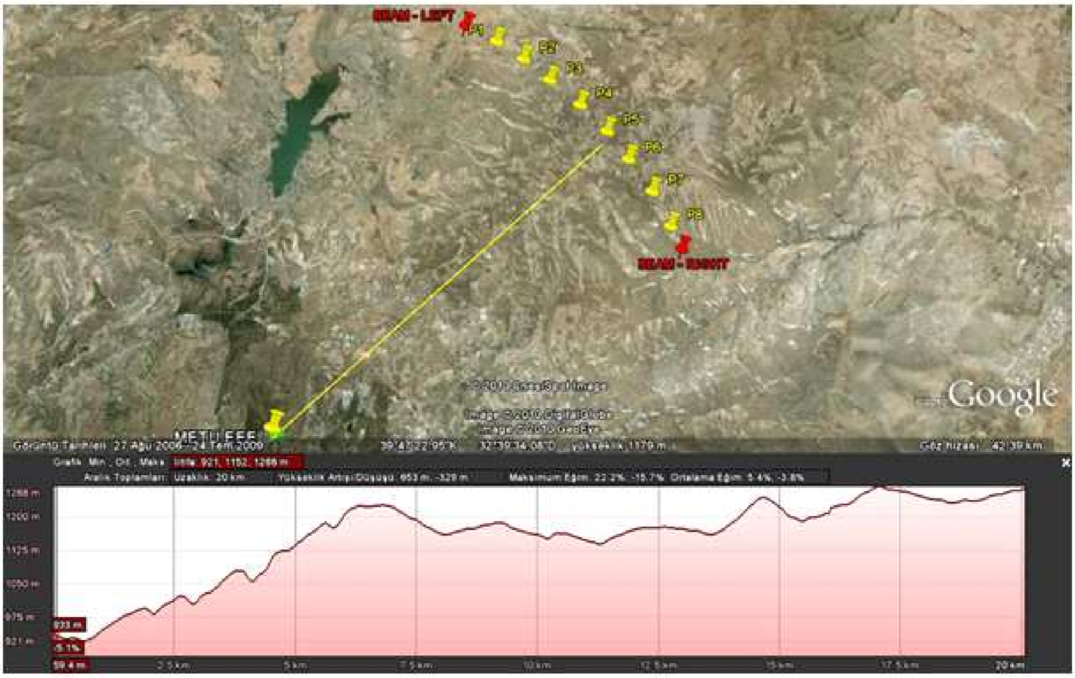

Figure D.15: Altitude profile of Path-5 for Terrain-2

Figure D.16: Altitude profile of Path-6 for Terrain-2

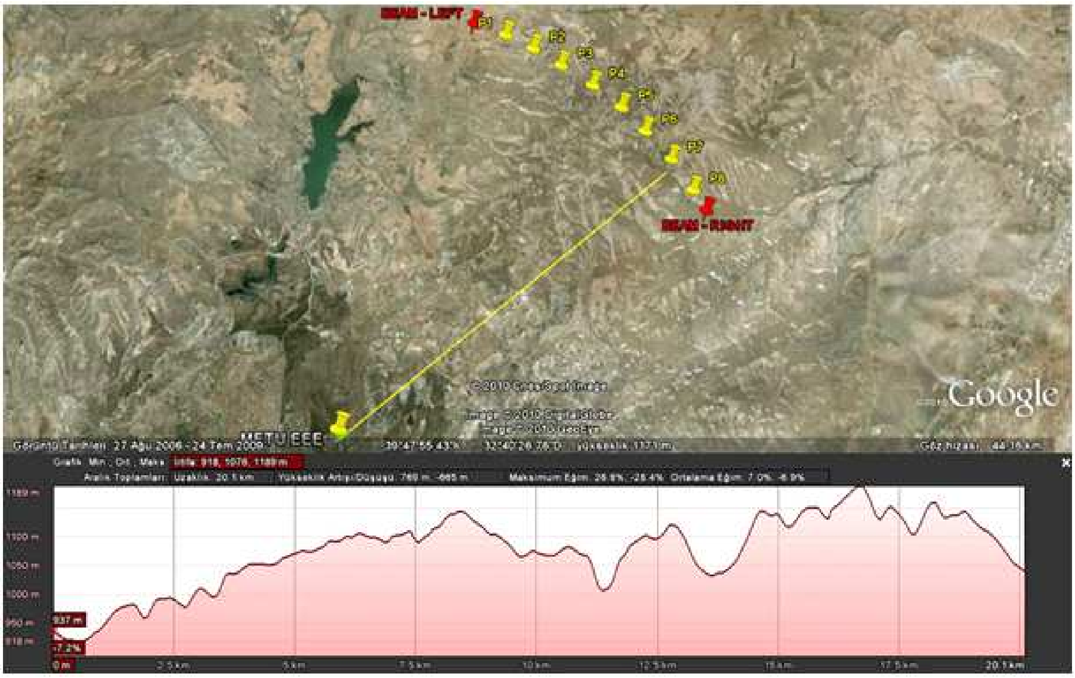

Figure D.17: Altitude profile of Path-7 for Terrain-2

Figure D.18: Altitude profile of Path-8 for Terrain-2

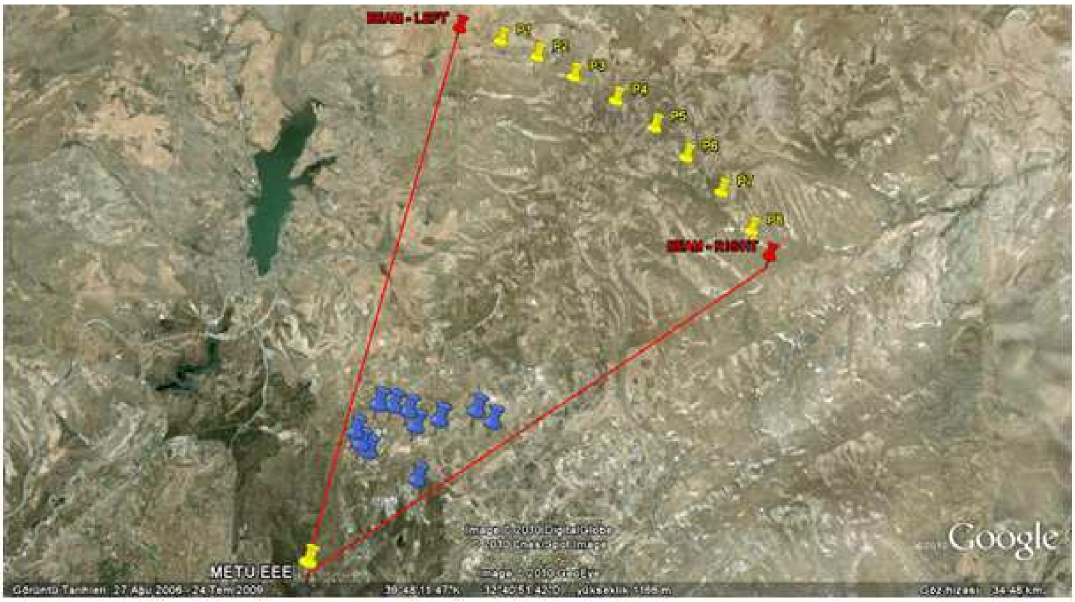

Figure D.19: Horizon line for Terrain-2